Nuclear Magnetic Resonance Readable Sensors

by
Yibo Ling

B.S.E. Biomedical Engineering, B.A English
University of Michigan - Ann Arbor, 2005

S.M. Electrical Engineering and Computer Science
Massachusetts Institute of Technology, 2008

Submitted to the Harvard-MIT Division of Health Sciences and Technology
in partial fulfillment of the requirements for the degree of

Doctor of Philosophy in Medical Engineering and Medical Physics
at the
MASSACHUSETTS INSTITUTE OF TECHNOLOGY
June 2010

Author.....
Harvard-MIT Division of Health Sciences and Technology
April 30th, 2010

Certified
by.....
Michael J. Cima, Ph.D.
Sumitomo Electric Industries Professor of Engineering
Thesis Supervisor

Certified
by.....
Robert S. Langer, Sc.D.
Institute Professor
HST Committee Chair

Accepted
by.....
Ram Sasisekharan, Ph.D
Director, Harvard-MIT Division of Health Sciences and Technology
Edward Hood Taplin Professor of Health Sciences & Technology and Biological Engineering

Nuclear Magnetic Resonance Readable Sensors

by
Yibo Ling

Submitted to the Harvard-MIT Division of Health Sciences and Technology
on April 30th, 2010 in partial fulfillment of the
requirements of the degree of
Doctor of Philosophy in Medical Engineering and Medical Physics

Abstract

The monitoring of physiological biomarkers is fundamental to the diagnosis and treatment of disease. We describe here the development of molecular sensors which can be read by magnetic resonance (MR) relaxometry. MR is an advantageous bio-sensor readout because it can be determined from opaque samples and through intervening layers of matter. Wash steps can therefore be avoided in *in vitro* MR assays and non-invasive interrogation achieved for *in vivo* MR sensing.

Functionalized magnetic nanoparticles originally developed as *in vivo* contrast agents have recently been adapted for use in magnetic relaxometry assays. The first half of this thesis describes a simple particle functionalization strategy and its application to the detection of myocardial infarction ("heart attack") associated biomarkers. The particles were subcutaneously implanted in the form of small discrete sensors and shown to be efficacious in measuring the physiological release of three protein biomarkers.

Alternative contrast mechanisms may also be employed by MR readable sensors. The second half of this thesis introduces the novel use of 'smart' polymers which produce analyte-responsive changes in MR relaxivity. We show that MR responsive calcium-crosslinked and pH-swelling hydrogels can be incorporated within discrete sensors.

Thesis Supervisor: Michael J. Cima
Title: Sumitomo Electric Industries Professor of Engineering

Acknowledgments

It is my privilege to have known and worked with great people.

Professor Cima taught me many important lessons about how to ask and answer scientific questions. He pushed me to take account of my thinking and to be a professional. Professors Langer and Adalsteinsson guided me through the process. Their mentorship eased me through rough stretches of the road.

Terrence Pong from the Cardiovascular Research Center (MGH) was an amazing collaborator and a good friend. He performed the intricate surgeries described in Chapter 3. Chris and Vincent poked and prodded me all the way to the end. We shared the successes and setbacks of the project and way too many meandering off-topic conversations. Grace and Karen were here when I came. They helped me transition onto the project and set me on my way. Yoda put my name next to the office door on my first day in lab. She showed me that truly selfless people actually exist. Alex, Barbara, Byron, Dan, Heejin, Hong Linh, Lenny, Maple, Noel, Qunya and Urvashi formed the rest of the labscape. Labmates make the lab experience and they made mine great.

Graduate school has been the most enjoyable experience of my first twenty-seven years. This is due in large part to the great friends I've made here. They taught me how to do some math and what it takes to be 'hard.' They taught me how to drive a stick and coast in neutral down a Costa Rican mountain. They taught me that having fun depends as much on the people around you as the nature of your endeavor.

I used to believe that my family was like all other families. I now know that is not true. Mine is exceptional; exceptional in their acceptance of my many faults and exceptional in their unwavering support for my choices. This thesis is dedicated to my mom, my dad, my grandma, my grandpa and Lan.

Contents

List of Figures

1 Introduction

5 MR Readable pH Sensor

List of Tables

Chapter 1

Introduction

This thesis work was undertaken in the field of molecular sensing. We focus in particular on magnetic resonance (MR) readable sensors which exhibit unique properties as compared to traditional sensing technologies. The purpose of this introductory chapter is to provide context and: 1) motivate our interest in MR based sensing, 2) give a brief explanation of the principles of the MR phenomenon and its use in traditional applications, and 3) describe the magnetic relaxation switch (MRSw) sensors on which our efforts were built.

1.1 Molecular Sensing

A cancer researcher may 'assay' blood serum to identify protein markers of disease progression (1). A nephrologist may look at blood urea nitrogen (BUN) and creatinine 'assays' to determine the functional status of a patient's kidneys (2-5). Molecular assays are analytical procedures through which the presence and quantity of a substance can be determined. They are employed in research and medicine to detect and measure the levels of specific targets from heterogeneous samples.

One widely used type of assay is the enzyme-linked immunoassay (ELISA). Figure 1.1 on the next page depicts the procedures required by a typical ELISA setup and helps to illustrate that molecular assays generally require:

1) A binding mechanism which is specific for the target of interest
2) A change which is induced as a result of the binding
3) A means of detecting and quantifying this change

The ELISA schematic shows that its binding mechanism is an antibody, the change induced is the colorimetric conversion of a substrate by alkaline phosphatase, and the means of detection is optical. The binding agent of a molecular assay can generally be a small molecule (6), a protein (7), or a chemically active surface (8); the induced change can be chemical (9), physical (10), or electrical (11, 12) in nature; the quantification method can be optical (13), electrochemical (14), or electromagnetic (15). A variety of assay techniques exist and most are, for all practical purposes, designed to obtain single time point data.

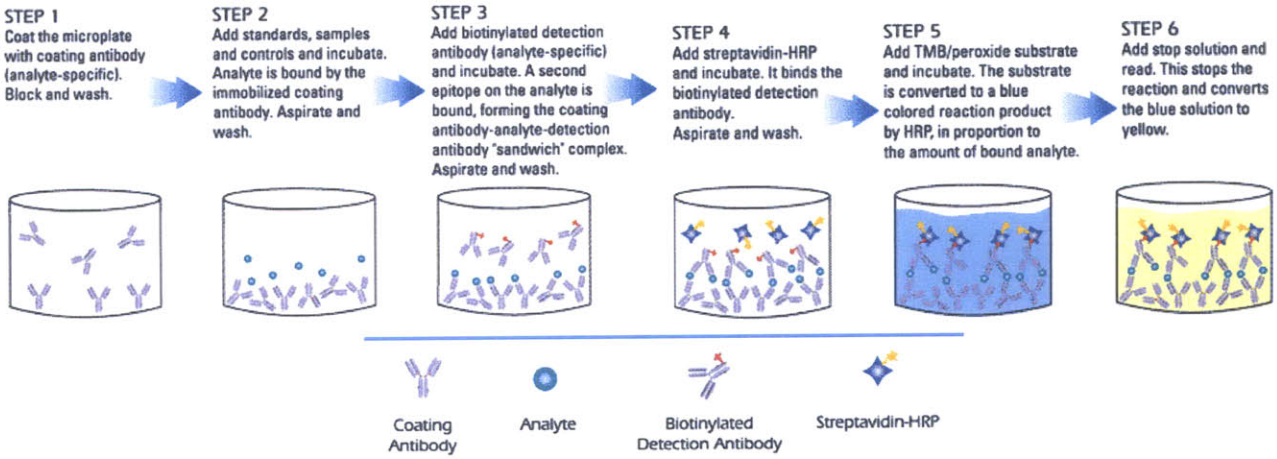

Figure 1.1 A schematic depiction of ELISA. A heterogeneous sample is first pipetted within a well which has been pre-coated with a coating antibody. The analyte of interest binds to the coating antibody. The well is then washed and a detection antibody, subsequently coupled to HRP via biotin-streptavidin binding, is added. Further addition of TMB substrate and a stop solution yields a colorimetric change which can be quantified using a spectrophotometer. Figure reproduced from Pierce website.

1.2 Implantable Sensors

Medical tests inform physicians seeking to determine the physiological status or response of their patients. Measurements in the clinic are typically made at single time points and so represent a brief sampling of a (generally) time-varying continuous signal. Continuous sensing would provide more complete information, but the means of doing so are often impractical given the limitations (time-consuming, invasive) of current measurement techniques. Continuous or high-frequency monitoring is possible for certain physiological parameters but can be difficult or impossible to achieve for molecular markers. Many heart failure patients, for instance, now rely on chronically implanted pacemakers and defibrillators to treat electrophysiological pathologies seen in the electrocardiogram (ECG) signal. These patients might also benefit from sentinel heart attack sensors which monitor the appearance of molecular biomarkers in the blood. No monitoring technology of this kind currently exists.

We are interested in discrete molecular sensors which, when implanted, can track its target biomarker over a sustained duration. Most research efforts underway in this category are concerned with glucose detection for diabetics (16-18) but there are many more important diseases and biomarkers. Incorporating existing molecular assay techniques within implantable sensors is one possible approach, but this strategy poses two hurdles: 1) most molecular assays require multi-step procedures which cannot be easily automated, and 2) the sensor readouts frequently require complex equipment that may be difficult to engineer onboard an implanted sensor. We describe in the body of this thesis a set of results pertaining to sensors for which the readout is based on MR relaxometry. We believe MR to be an advantageous readout for implanted sensors because the signal can be measured from turbid samples so that such assays often consist of single-step procedures. MR measurements may also be made at a distance and through tissue, thus obviating the need to build complex electronics onboard the implant.

1.3 The Magnetic Resonance Phenomenon

The following section provides a brief description of the classical (i.e. non-quantum mechanics based) view of magnetic resonance, also called nuclear magnetic resonance.

1.3.1 MR Excitation

Atoms possessing a 'nuclear spin angular momentum' (possessing an odd number of protons or neutrons) can be treated as charged spinning spheres. Spinning charges give rise to magnetic moments. The MR phenomenon comes about as an interaction of these magnetic moments (i.e. spins) with externally applied fields. The individual moments align under a constant uni-directional field $\vec{B}_0$ (in what is conventionally defined as the z-direction) to generate a net magnetic moment which we may treat as a single vector $\vec{M}$. They precess at a well-defined rate called the Larmour frequency $\omega_0 = \gamma \vec{B}_0$ where γ is the gyromagnetic ratio (the ratio between the angular momentum and the magnetic dipole moment). This *resonant* Larmour frequency is specific to each type of atom. Subsequent application of a radiofrequency (RF) pulse $\vec{B}_1$ at the Larmour frequency in a direction within the xy-plane can torque $\vec{M}$ out of longitudinal alignment. A $\vec{B}_1$ pulse of the appropriate duration and strength can induce a full 90° rotation of $\vec{M}$ into the xy-plane. $\vec{M}$ then relaxes back into alignment with the $\vec{B}_0$ field upon cessation of the excitation pulse. This process is summarized in Figure 1.2.

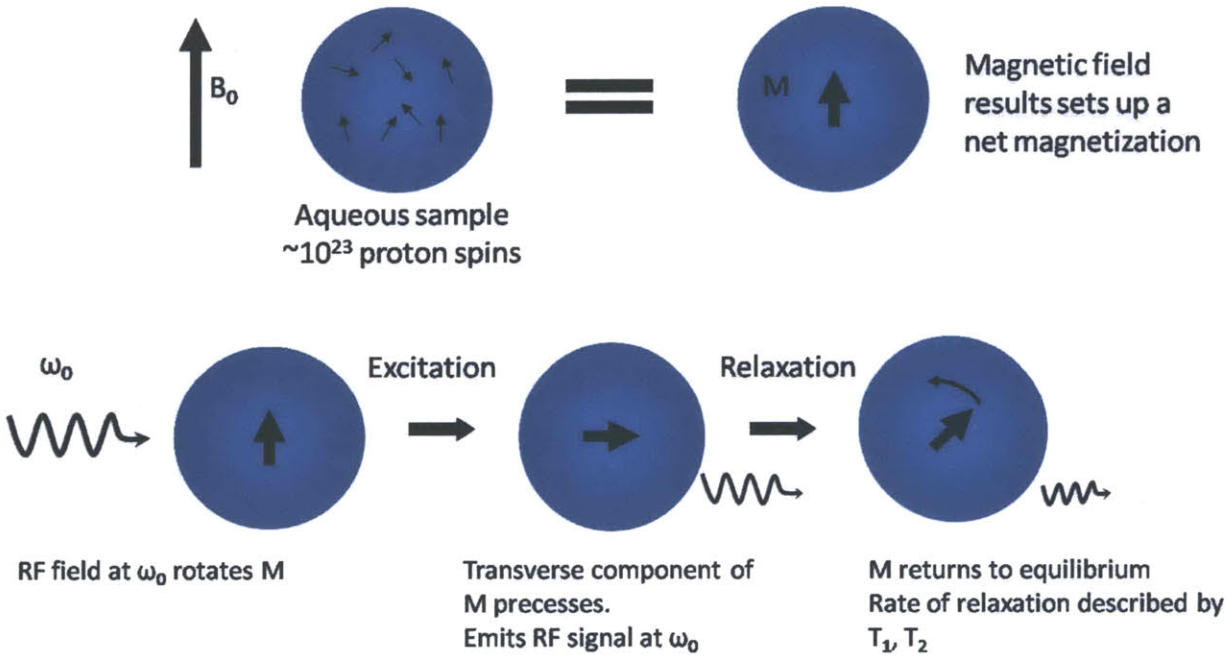

Figure 1.2 A schematic explanation of the MR phenomenon. Proton spins align with the static $\vec{B}_0$ field and can be treated as a single magnetic vector $\vec{M}$. RF excitation at the Larmour frequency ω_0 leads to a 90° rotation of the vector into the xy-plane. $\vec{M}$ subsequently relaxes back into alignment with the $\vec{B}_0$ field.

1.3.2 MR Relaxation

Relaxation can be intuitively thought of as energy dissipation, a set of magnetic moments transitioning back into alignment with an externally imposed equilibrium. Relaxation would not occur under ideal conditions when only a constant $\vec{B}_0$ field is present. Thermal motion in real samples, however, causes molecules to rapidly tumble so that only a small subset of spins are actually aligned in the z-directional at any given moment. Each molecule possessing a magnetic moment produces its own local field distortion which fluctuates with its thermal motion. A given nucleus (which is a single element of a much larger set) hence 'sees' not a constant $\vec{B}_0$ but rather $\vec{B}_0 + \vec{B}_{random}(t)$ where $\vec{B}_{random}(t)$ fluctuates randomly over time. The longitudinal component of these tiny perturbations causes, among the ensemble of spins, a loss of phase coherence in the transverse plane. If we consider this dispersal as a random walk, then the distribution of the ensemble phase will be Gaussian with a variance that grows with time. The readout signal is the sum of the projection of these spins in a single direction within the xy-plane so phase dispersal attenuates transverse signal. It can be shown that when the cosine of the phase is integrated over a Gaussian distribution, the signal attenuation in the transverse plane (and similarly the signal recovery in the longitudinal direction) is an exponential function of time. $\vec{M}$ changes in both magnitude and direction during the relaxation process, and its dynamics are described by two relaxivity time constants, T_1 (longitudinal) and T_2 (transverse). The reason that the longitudinal relaxation rate differs from the transverse relaxation rate is that T_2 is sensitive to all random field fluctuations while T_1 is only sensitive to those acting at the Larmour frequency. Recall that the initial 90° excitation was generated by a RF signal tuned to the Larmour frequency. It goes to reason that the longitudinal relaxation of $\vec{M}$ back into z-alignment can only be induced by field fluctuations acting at this specific frequency. Transverse relaxation, as discussed above, is thus an unrecoverable loss in phase coherence while longitudinal relaxation is a phase-independent process. The following description of nuclear magnetization in MR, called the Bloch equation, was empirically found to describe these dynamics:

$$\frac{d\vec{M}}{dt} = \vec{M} \times \gamma\vec{B} - \frac{\vec{M}_x\vec{i} + \vec{M}_y\vec{j}}{T_2} - \frac{(\vec{M}_z - \vec{M}_0)\vec{k}}{T_1} \tag{1}$$

where $\vec{i}$, $\vec{j}$, $\vec{k}$ are unit vectors pointing in the x-, y-, and z-directions. T_1 is denoted by convention as the exponential recovery constant along the z-axis so longitudinal relaxation is described by the differential equation:

$$\frac{dM_z}{dt} = -\frac{M_z - M_0}{T_1} \tag{2}$$

for which the solution is:

$$M_z = M_0 + (M_z(0) - M_0)e^{-t/T_1} \tag{3}$$

The signal's decay constant in the xy-plane is denoted T_2 and described by the differential equation:

$$\frac{dM_{xy}}{dt} = -\frac{M_{xy}}{T_2} \tag{4}$$

for which the solution is:

$$M_{xy} = M_0 e^{-t/T_2} \tag{5}$$

1.3.3 Loss and Recovery of Phase Coherence

The MR signal read by a detector is the uni-directional projection of an ensemble of magnetic vectors. Sources contributing to loss of phase coherence therefore attenuate the MR signal. Field inhomogeneities resulting from equipment imperfections and susceptibility effects are two common sources of signal attenuation, producing what is called a T_2* decay. Note that whereas T_2 relaxation is based on inherent loss of phase coherence from random field fluctuations, T_2* results from constant field distortions. Modifying our previous equation, a given nucleus actually 'sees' $\vec{B}_0 + \vec{B}_{inhomo}(x,y,z) + \vec{B}_{random}(t)$ where the term $\vec{B}_{in\,hom\,o}(x,y,z)$ depends on spatial position (but not time). Loss of phase coherence due to these positionally-dependent but time-invarying distortions can be recovered. One commonly used 'spin echo' concept uses refocusing RF pulses which rotate the vector 180° about the x'-axis (rotational frame x-axis) some time τ after the original 90° RF pulse (Figure 1.3).

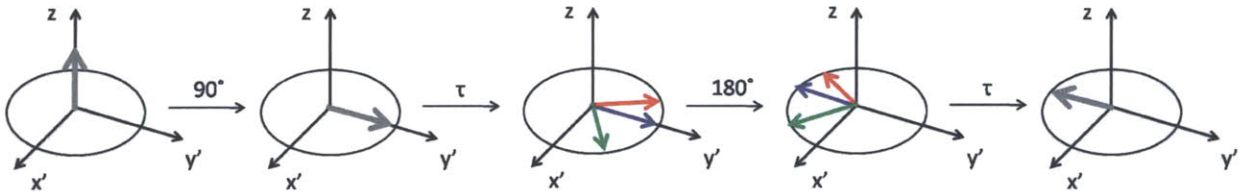

Figure 1.3 The spin echo refocusing concept (adapted from *Principles of Magnetic Resonance Imaging* by Dwight G. Nishimura).

A phase φ accumulates after τ but the refocusing pulse rotates the magnetic vector to a phase π–φ. The vector then once more accrues phase φ after another period τ and returns (with π offset) as an 'echo' to phase coherence TE = 2τ (TE is called the echo time) after the initial 90° RF pulse. The in-phase echoes subject to T_2* decay (shown in Figure 1.4) are used as the MR readout; sampling of these echo peaks can reveal the envelope function of intrinsic T_1 and T_2 relaxation. One caveat to the efficacy of the spin echo technique is that individual magnetic moments must move relatively slowly as compared to TE so that they are subjected to the same field (possibly offset from $\vec{B}_0$ by some inhomogeneity) both before and after the refocusing pulse.

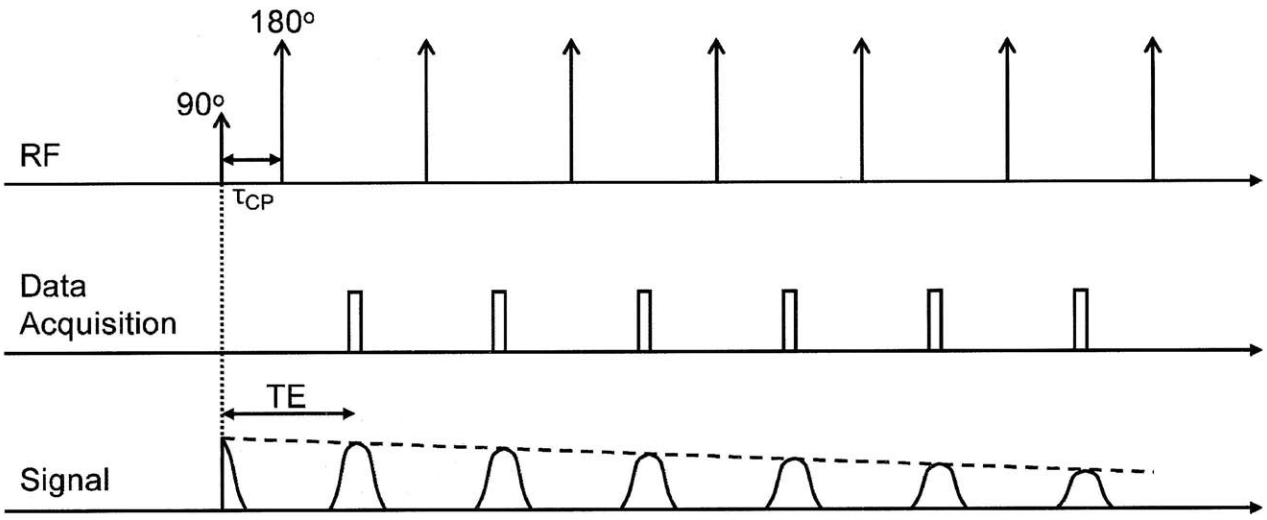

Figure 1.4 A spin echo pulse train. TE = echo time. The dotted line in the lower graph indicates the envelope of T_2 while the solid lines show re-focusing and T_2* decay.

1.3.4 Spectroscopy and Imaging

The magnetic resonance phenomenon underlies two of today's most basic analytical tools. NMR spectroscopy is perhaps the most important technique available for studying the chemical structure of compounds. A number of atoms (^{1}H, ^{13}C ^{19}F, ^{23}Na, ^{31}P) possess spin angular momentum and so can be probed by NMR. The attachment of these atoms to a chemical group produces a slight but characteristic 'chemical shift' in their resonant Larmour frequencies because some energy can be transferred through the chemical bonds. Protons attached to water vs. methyl groups are, for instance, slightly but visibly offset in resonant frequency thus allowing for the determination of relative water and fat composition in biological tissues.

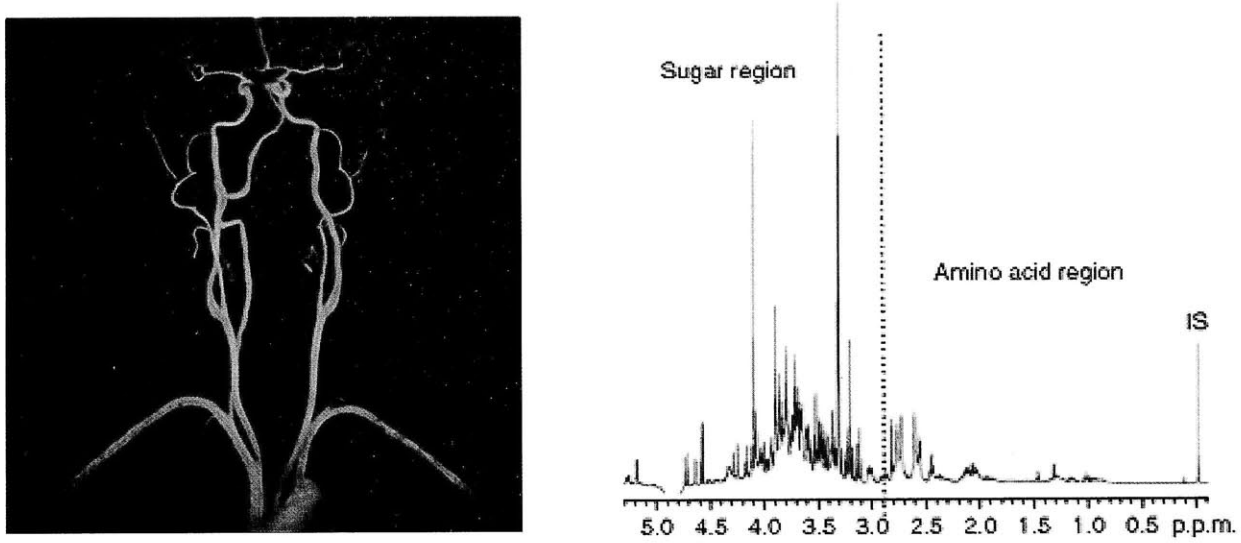

Figure 1.5 A MRI angiogram (19) and NMR spectral analysis of *Brassica rapa* metabolism (20).

Magnetic resonance imaging (MRI) has become an integral tool in modern medicine, the subject of multiple Nobel prizes, and a topic of intense continuing research. MRI applies linear spatial gradients to resolve spatial information within the volume of a sample. Its principles can most easily be described by considering the 1-dimensional case in which after RF excitation a $\vec{B}_0 + \vec{G}_x x$ field, where x is spatial distance, is applied rather than a static $\vec{B}_0$ field. Individual magnetic vectors at distances x will precess at differing but well-defined rates. The time signal that is received is then a cumulative one possessing a range of frequencies. Fourier transformation yields a frequency-to-location mapping which allows for the resolution of spatial information. This idea can be scaled up to localize physically segregated MR sources and enable 3D reconstruction. Examples of MRI images and NMR spectrums are shown in Figure 1.5 on the previous page.

1.4 Magnetic Relaxation Switch Sensors

Magnetic relaxation switch sensors are aqueous suspensions of functionalized magnetic particles. The particles 'switch' from a dispersed to a clustered state in the presence of specific molecular targets (15, 21). Clustering induces a change in the solvent's relaxation time which can in turn be measured by clinical MRI scanners or benchtop NMR relaxometers. Cross-linked iron oxide (CLIO) particles are the class of superparamagnetic iron oxide (SPIO) nanoparticles most frequently used as MRSw's. They possess 3-5 nm monocrystalline $(Fe_2O_3)_n(Fe_3O_4)_m$ cubic close packed cores in an inverse spinel structure. The cores sit within shells of dextran cross-linked with epichlorohydrin to enable solution stability; the particles can also be coated with exterior amine or other chemical groups to reach final dimensions of 20-100 nm in diameter. A summary of the different types of MRSw particles that have been used is given in Table 1.1 below.

Particle	Size	Composition	Characteristics	Reference
CLIO	~30 nm	5 nm core, 10 nm dextran coating	R_2 = 40 (s•mM Fe)$^{-1}$	(15)
Core/Shell	16 nm	Fe core, iron oxide shell, 2.5 nm shell thickness	R_2 = 260 (s•mM Fe)$^{-1}$	(22)
Mn-Magnetic Nanoparticle	16 nm	Mn-doped iron oxide	R_2 = 420 (s•mM metal)$^{-1}$	(23)
Magnetic Particle	1000 nm	Commercial (Dynabeads)	R_2 = 43 (s•mM Fe)$^{-1}$	(24)

Table 1.1 Characteristics of MRSw particles used for biosensing. Adapted from Koh and Josephson (25).

Ohgushi *et al.* first noticed in the late 1970's that magnetic particles reduce the T_2 of their solvent (26). This observation led by the 1990's to the adaptation of SPIO nanoparticles into 'targeted' MRI contrast agents which bind to and enable the MR visualization of specific cells or molecules *in vivo*. It was during the course of these efforts (27-30) that Josephson *et al.* found suspensions of particle clusters to exhibit markedly enhanced rates of relaxation as compared to their dispersed counterparts (Figure 1.6); SPIO nanoparticles were subsequently developed into target-specific *in vitro* assay materials (31). Targeting could be achieved through surface functionalization with antibodies,

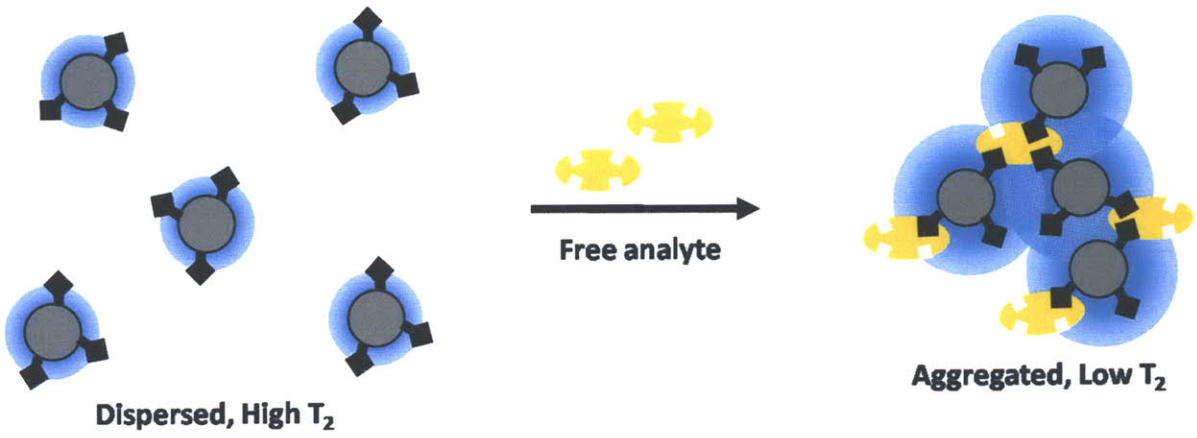

Figure 1.6 A schematic illustration of the principle of the MRSw assay. Magnetic nanoparticles (left) with attached binding moieties cluster when analyte is added (right), resulting in a T_2 change of the aqueous phase.

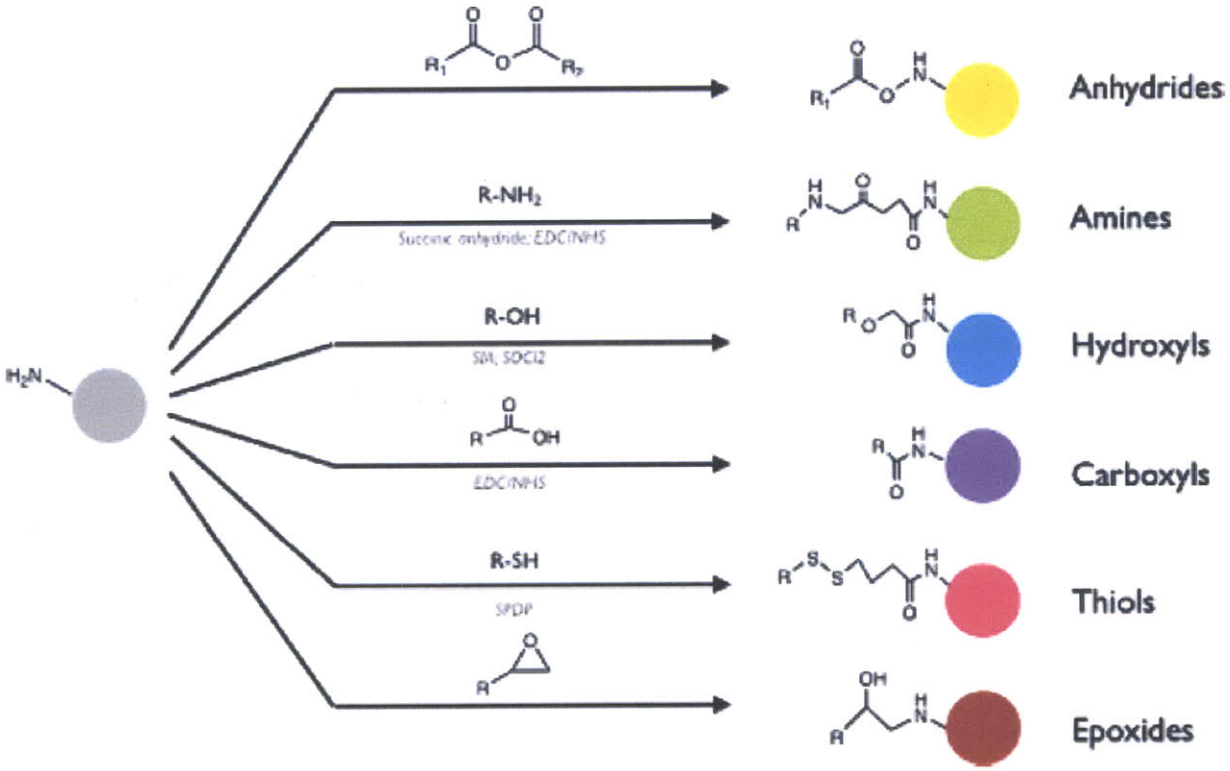

Figure 1.7 Conjugation strategies to magnetofluorescent nanoparticles. Aminated magnetofluorescent nanoparticles were reacted with small molecules with different reactivities. Reproduced from Sun *et al.* (32).

nucleic acids, aptamers or other binding moieties. A variety of procedures and chemical groups can be used to link them to particle surfaces (Figure 1.7). We employ N-hydroxysuccinimide (NHS) based bifunctional cross-linking to induce covalent attachment of sulfhydryl-bearing binding moieties.

New configurations and additions exploiting the MRSw principle now exist: sensing can be based on aggregation of similar sized particles, aggregation between micro- and nanoparticles, cluster dispersal, or sedimentation of particle aggregates (24, 33). Recently a lab-on-a-chip microNMR detector was developed to enable multiplexed point-of-care application of MRSw assays (34). A company, T2 Biosystems, has also been founded to commercialize MRSw technology as a medical diagnostic platform (35).

1.4.1 Magnetic Nanoparticles as MR Field Inhomogeities

Nanoparticles possessing SPIO cores become magnetized and possess high relaxivities (10-100 mM^{-1} Fe S^{-1}) when placed in external fields. The individual electron spins act in unison to form a larger magnetic dipole and this dipole creates local magnetic distortions in otherwise uniform magnetic fields. Water protons drifting through these areas of local inhomogeneity rapidly lose phase coherence with the rest of the solution (Figure 1.8); addition of magnetic nanoparticles to an aqueous solution therefore impacts the overall relaxivity of the surrounding water protons. We next discuss the outer sphere theory, which offers an explanation for why the particles exhibit markedly different transverse relaxations when aggregated. This behavior lies at the foundation of all MRSw assays, which have been adapted to detect proteins, antibodies, receptor ligands, peptides, nucleic acids, oligonucleotides, and other small molecules (10, 15, 21, 36-38).

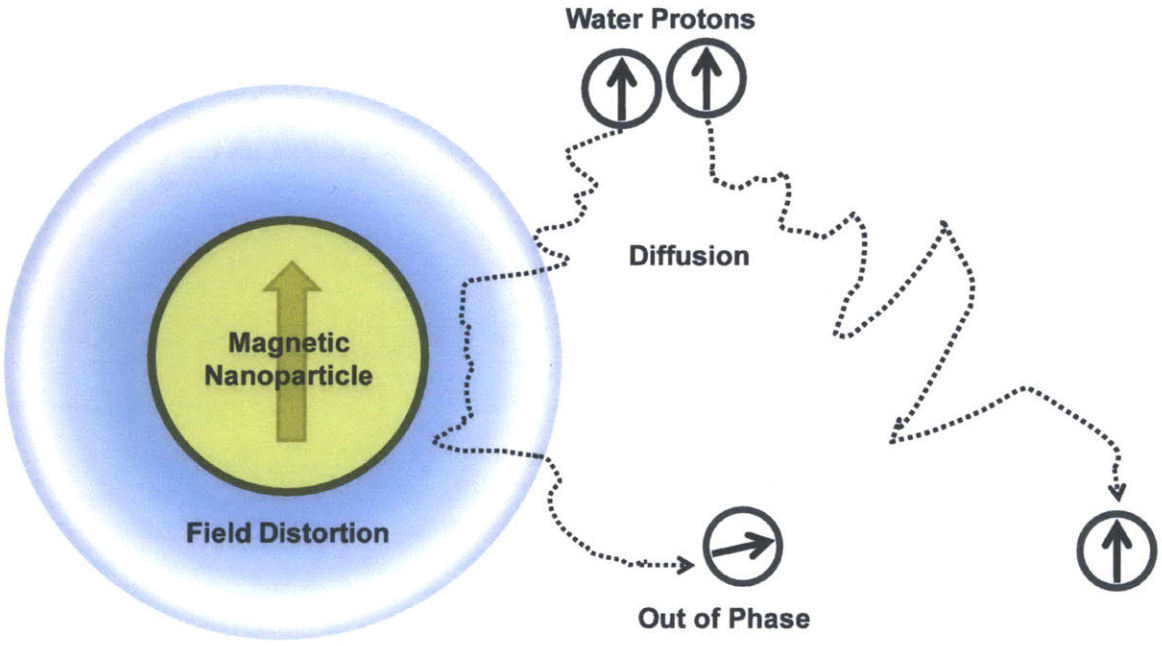

Figure 1.8 A schematic of the mechanism by which magnetic nanoparticles are thought to shorten solvent T_2. A proton diffusing past the local field distortion generated by the nanoparticle will lose phase coherence relative to the protons which do not.

1.4.2 Outer Sphere Theory

Outer sphere theory is the predominant model used in the literature to quantify the transverse relaxation of magnetic nanoparticles. It states:

$$1/T_2 = (4/9)V(\Delta\omega)^2\tau_d \quad (6)$$

where V is the nanoparticle occupied volume fraction of the sample, $\tau_d = r^2/D$ (where r is particle radius, D is self-diffusion coefficient of water), and $\Delta\omega = (1/3)\mu_0\gamma M$ (where M is particle magnetization, μ_0 is the free space magnetic permeability, and γ is the proton gyromagnetic ratio).

The theory in general differentiates between two echo time dependent regimes. The static dephasing regime applies when $\tau_D >> \tau$ where τ_D is the characteristic diffusion time of water and τ is echo time used in the pulse sequence. Water molecules, in this regime, are static and so loss of phase coherence is almost completely recoverable by spin echo pulses. Contrast this with the motional averaging regime for which $\tau_D << \tau$; phase coherence cannot be recovered here because water protons have diffused through the areas of inhomogeneity and so are subject to asymmetrical field distortions prior to and after the spin echo pulse. MR measurements of SPIO are thought to be confined to the motional averaging regime. Eq. (6) hence assumes $\tau_D << \tau$.

SPIO nanoclusters were treated by Shapiro *et al.* (39) as single nanoparticles possessing increased volumes (40). They derived a relationship between T_2 and cluster size by:

1) Assuming clusters are fractal aggregates of individual particles possessing a ratio of:

$$r \propto n^{1/df} \quad (7)$$

where r is the effective radius of the aggregate, n is the number of individual nanoparticles in the aggregate, and df is the fractal's degrees of freedom.

2) Assuming M is proportional to the number of nanoparticles per aggregate:

$$M \propto \frac{n}{r^3} \propto r^{df-3} \quad (8)$$

so that if V and D do not depend on aggregation, we can plug Eqs. (7-8) into Eq. (6) to obtain:

$$1/T_2 = (4/9)V(\Delta\omega^2)\tau_D \propto M^2 r^2 \propto r^{2df-4} \quad (9)$$

The above equation predicts T_2 decreases ($1/T_2$ increases) with increasing r, as long as $df > 2$. The published findings show the T_2 of SPIO nanoparticle aggregates to be shorter than that of dispersed nanoparticles.

1.5 Overview of Thesis

MR sensing possesses the following characteristics: 1) the magnetic resonance of materials can be determined from a distance, through tissue or other material, 2) magnetic resonance is most decidedly not an optical technique and is therefore robust for interrogating opaque samples. These properties make MR sensing useful for both *in vivo* applications in which passive implanted sensors can be repeatedly interrogated and *in vitro* applications for which single-step assay procedures (no wash cycles) streamline the work of clinicians and researchers alike. The *sensors* described in this thesis are diffusion devices that allow the inward flux of target analytes and which contain a sensing medium whose MR properties are altered by the presence of the target. Past efforts to develop MR-readable sensors have incorporated magnetic relaxation switch (MRSw) technology to generate relaxivity-based contrast. We point out that magnetic nanoparticle clustering, though effective, is only one possible basis for generating T_2 contrast.

1.5.1 Thesis Roadmap

This thesis can be divided into two sections. I describe in the first half, chapters 2 and 3, the progress we have made in making MRSw-based sensors easier to use and more viable for *in vivo* application. I discuss in the second half, chapters 4 and 5, the identification and characterization of novel mechanisms for generating MR contrast from non-MRSw sensing media. These efforts are schematically summarized by Figure 1.9.

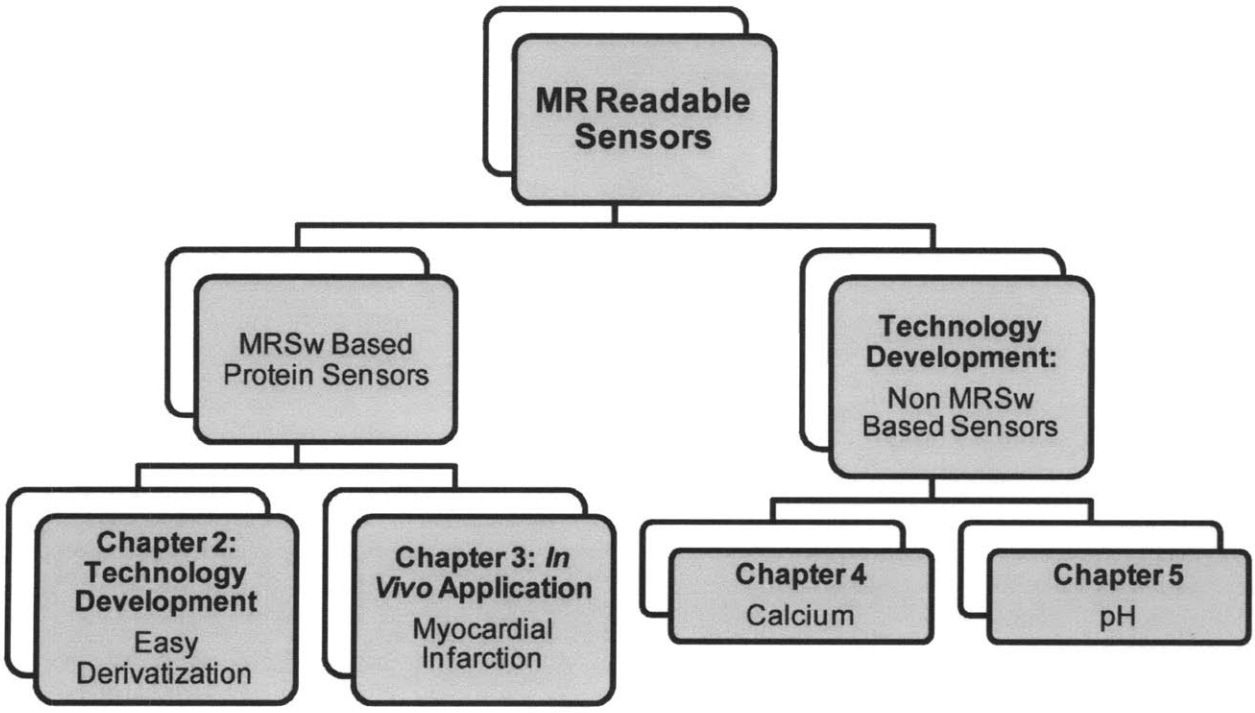

Figure 1.9: Thesis roadmap.

1.5.2 Summary of Chapters

Chapter 2: A novel technique for facile derivatization of MRSw.

Protein assays are widely used in experimental biology and biochemistry. Our goal was to build a MRSw platform approaching the ease-of-use of common assay platforms such as ELISA, and which can be adapted to detect many different protein targets (1, 41, 42). Previous work in which target-specific antibodies were conjugated to nanoparticles has demonstrated that MRSw assays can detect a variety of protein targets (1, 32, 41-43). However, the time and effort required to generate these functionalized particle sets makes the process cumbersome (7, 44). Conjugation chemistry can take over 12 hours to complete and effective valency of the particles (antibodies per particle) is difficult to manage even under carefully controlled conditions. The approach we show here exploits primary-secondary antibody binding so that a single set of particles can be used as a platform from which subsets may be derivatized to target specific proteins by single-step incubations.

Chapter 3: MRSw based detection of myocardial infarction in an in vivo mouse model.

Many patients suffering from cardiac disease experience myocardial infarctions (MI), a process by which the occlusion of a cardiac artery leads to myocardial ischemia and death. The efficacy of MRSw sensors was been demonstrated *in vivo* for the detection of hCG (human chorionic gonadotropin), a cancer biomarker. We show in this chapter the *in vivo* efficacy of MRSw-based sensors for the detection of standard markers of myocardial infarction: troponin I, creatine kinase-MB and myoglobin (45). We further show that these sensors can quantify the magnitude of an acute MI. Myocardial infarction was chosen because its panel of markers is of practical clinical consequence, and accessible animal models of MI release biomarkers at physiological concentrations.

Chapter 4: non-MRSw Calcium Sensing

MR readable sensors are attractive because they can be simple, passive, and interrogated at a distance (potentially through tissue). While MRSw assays use particle aggregation-dependent changes in solution relaxivity, other analyte-sensitive materials can also trigger relaxivity changes. We describe in this chapter a non-MRSw means of detecting calcium using alginate as the sensing medium. Alginate pre-polymer can be induced to gel by adding calcium (46). We exploit this phenomenon, after observing that liquid pre-polymer and polymerized hydrogel possess differing relaxivities (47), to develop a MR readable calcium sensor.

Chapter 5: non-MRSw pH Sensing

'Smart' hydrogels which respond to specific stimuli have been used in drug delivery (48, 49), as mechanical actuators (50, 51), and to achieve molecular separation (52). For instance, an insulin delivery mechanism has been described which consists of glucose-sensitive polymers capable of expanding to release calibrated doses of insulin (53). pH is a fundamental physiological parameter that is deranged in numerous pathological processes. It is thus a valuable biomarker. We describe in this chapter a non-MRSw means of quantifying environmental pH through MR relaxometry by using a pH-sensitive hydrogel. We focus on the *in vitro* characterization of the gel's contrast mechanism and characterize its dynamics when enclosed within discrete implantable sensors.

1.6 References

1. Engvall E & Perlmann P (1971) Enzyme-linked immunosorbent assay (ELISA). Quantitative assay of immunoglobulin G. *Immunochemistry* 8(9):871-874 .
2. Hankins DA, Babb AL, Uvelli DA, Miller WP, & Scribner BH (1981) Creatinine production rate measured by whole body counting of 40K. *Int J Artif Organs* 4(1):31-34 .
3. Hankins DA, Babb AL, Uvelli DA, & Scribner BH (1981) Creatinine degradation. II: Mathematical model including the effect of extra-renal removal rates. *Int J Artif Organs* 4(2):68-71 .
4. Hankins DA, Babb AL, Uvelli DA, & Scribner BH (1981) Creatinine degradation I: the kinetics of creatinine removal in patients with chronic kidney disease. *Int J Artif Organs* 4(1):35-39 .
5. Maeda M, Otsuki M, Okano K, Yamasaki T, & Baba S (1981) Clinical evaluation of amylase-creatinine clearance ratio and amylase isoenzyme clearance in chronic renal failure. *Gastroenterol Jpn* 16(3):242-248 .
6. Wang WU, Chen C, Lin KH, Fang Y, & Lieber CM (2005) Label-free detection of small-molecule-protein interactions by using nanowire nanosensors. *Proceedings of the National Academy of Sciences of the United States of America* 102(9):3208-3212 .
7. Kim GY, Josephson L, Langer R, & Cima MJ (2007) Magnetic relaxation switch detection of human chorionic gonadotrophin. *Bioconjug Chem* 18(6):2024-2028 .
8. Liu AH (2008) Towards development of chemosensors and biosensors with metal-oxide-based nanowires or nanotubes. *Biosensors & Bioelectronics* 24(2):167-177 .
9. Liu J, *et al.* (2007) Label-free protein detection by ZnO nanowire based bio-sensors. *57th Electronic Components & Technology Conference, 2007 Proceedings*:1971-1976, 2040 .
10. Perez JM, O'Loughin T, Simeone FJ, Weissleder R, & Josephson L (2002) DNA-based magnetic nanoparticle assembly acts as a magnetic relaxation nanoswitch allowing screening of DNA-cleaving agents. *J Am Chem Soc* 124(12):2856-2857 .
11. Patolsky F, Zheng GF, & Lieber CM (2006) Fabrication of silicon nanowire devices for ultrasensitive, label-free, real-time detection of biological and chemical species. *Nature Protocols* 1(4):1711-1724 .
12. Zheng GF, Patolsky F, & Lieber CM (2006) General and powerful platform for large-scale, label-free, parallel electrical detection of biomolecules by ultrasensitive nanowire transistor arrays. *Abstracts of Papers of the American Chemical Society* 231:- .
13. Liu Y, Gerber R, Wu J, Tsuruda T, & McCarter JD (2008) High-throughput assays for sirtuin enzymes: a microfluidic mobility shift assay and a bioluminescence assay. *Anal Biochem* 378(1):53-59 .
14. Anandan V, Rao YL, & Zhang GG (2006) Nanopillar array structures for enhancing biosensing performance. *International Journal of Nanomedicine* 1(1):73-79 .
15. Perez JM, Josephson L, O'Loughlin T, Hogemann D, & Weissleder R (2002) Magnetic relaxation switches capable of sensing molecular interactions. *Nat Biotechnol* 20(8):816-820 .
16. Renard E (2004) Implantable glucose sensors for diabetes monitoring. *Minim Invasiv Ther* 13(2):78-86 .
17. Koschwanez HE & Reichert WM (2007) In vitro, in vivo and post explantation testing of glucose-detecting biosensors: Current methods and recommendations. *Biomaterials* 28(25):3687-3703 .
18. Daniloff GY (1999) Continuous glucose monitoring: long-term implantable sensor approach. *Diabetes Technol Ther* 1(3):261-266 .

19. Sherry AD & Woods M (2008) Chemical exchange saturation transfer contrast agents for magnetic resonance imaging. *Annu Rev Biomed Eng* 10:391-411 .
20. Kim HK, Choi YH, & Verpoorte R (NMR-based metabolomic analysis of plants. *Nat Protoc* 5(3):536-549 .
21. Perez JM, Josephson L, & Weissleder R (2004) Use of magnetic nanoparticles as nanosensors to probe for molecular interactions. *Chembiochem* 5(3):261-264 .
22. Lee H, Yoon TJ, & Weissleder R (2009) Ultrasensitive detection of bacteria using core-shell nanoparticles and an NMR-filter system. *Angew Chem Int Ed Engl* 48(31):5657-5660 .
23. Lee H, Yoon TJ, Figueiredo JL, Swirski FK, & Weissleder R (2009) Rapid detection and profiling of cancer cells in fine-needle aspirates. *Proc Natl Acad Sci U S A* 106(30):12459-12464 .
24. Koh I, Hong R, Weissleder R, & Josephson L (2008) Sensitive NMR sensors detect antibodies to influenza. *Angew Chem Int Ed Engl* 47(22):4119-4121 .
25. Koh I & Josephson L (2009) Magnetic Nanoparticle Sensors. *Sensors* 9(10):8130-8145 .
26. Ohgushi MN, K.; Wada, A. (1978) Dextra-Magnetite - New Relaxation Agent and Its Application to T_2 Measurements in Gel Systems. . *Journal of Magnetic Resonance* 29:599-601.
27. Schellenberger EA, *et al.* (2002) Annexin V-CLIO: a nanoparticle for detecting apoptosis by MRI. *Mol Imaging* 1(2):102-107 .
28. Kang HW, Josephson L, Petrovsky A, Weissleder R, & Bogdanov A, Jr. (2002) Magnetic resonance imaging of inducible E-selectin expression in human endothelial cell culture. *Bioconjug Chem* 13(1):122-127 .
29. Wunderbaldinger P, Josephson L, & Weissleder R (2002) Crosslinked iron oxides (CLIO): a new platform for the development of targeted MR contrast agents. *Acad Radiol* 9 Suppl 2:S304-306 .
30. Weissleder R, *et al.* (1990) Ultrasmall superparamagnetic iron oxide: characterization of a new class of contrast agents for MR imaging. *Radiology* 175(2):489-493 .
31. Josephson L, Perez JM, & Weissleder R (2001) Magnetic nanosensors for the detection of oligonucleotide sequences. *Angewandte Chemie-International Edition* 40(17):3204-+ .
32. Sun EY, Josephson L, Kelly KA, & Weissleder R (2006) Development of nanoparticle libraries for biosensing. *Bioconjug Chem* 17(1):109-113 .
33. Tsourkas A, Hofstetter O, Hofstetter H, Weissleder R, & Josephson L (2004) Magnetic relaxation switch immunosensors detect enantiomeric impurities. *Angewandte Chemie-International Edition* 43(18):2395-2399 .
34. Lee H, Sun E, Ham D, & Weissleder R (2008) Chip-NMR biosensor for detection and molecular analysis of cells. *Nature Medicine* 14(8):869-874 .
35. Lowery TJ, Palazzolo R, Wong SM, Prado PJ, & Taktak S (2008) Single-coil, multisample, proton relaxation method for magnetic relaxation switch assays. *Analytical Chemistry* 80(4):1118-1123 .
36. Perez JM, Simeone FJ, Saeki Y, Josephson L, & Weissleder R (2003) Viral-induced self-assembly of magnetic nanoparticles allows the detection of viral particles in biological media. *J Am Chem Soc* 125(34):10192-10193 .
37. Taktak S, Sosnovik D, Cima MJ, Weissleder R, & Josephson L (2007) Multiparameter magnetic relaxation switch assays. *Anal Chem* 79(23):8863-8869 .
38. Tsourkas A, Hofstetter O, Hofstetter H, Weissleder R, & Josephson L (2004) Magnetic relaxation switch immunosensors detect enantiomeric impurities. *Angew Chem Int Ed Engl* 43(18):2395-2399 .

39. Shapiro MG, Atanasijevic T, Faas H, Westmeyer GG, & Jasanoff A (2006) Dynamic imaging with MRI contrast agents: quantitative considerations. *Magn Reson Imaging* 24(4):449-462 .
40. Brooks RA, Moiny F, & Gillis P (2001) On T2-shortening by weakly magnetized particles: the chemical exchange model. *Magn Reson Med* 45(6):1014-1020 .
41. Engvall E, Jonsson K, & Perlmann P (1971) Enzyme-linked immunosorbent assay. II. Quantitative assay of protein antigen, immunoglobulin G, by means of enzyme-labelled antigen and antibody-coated tubes. *Biochim Biophys Acta* 251(3):427-434 .
42. Engvall E & Perlmann P (1972) Enzyme-linked immunosorbent assay, Elisa. 3. Quantitation of specific antibodies by enzyme-labeled anti-immunoglobulin in antigen-coated tubes. *J Immunol* 109(1):129-135 .
43. Sun EY, Weissleder R, & Josephson L (2006) Continuous analyte sensing with magnetic nanoswitches. *Small* 2(10):1144-1147 .
44. Daniel KD, *et al.* (2007) Multi-reservoir device for detecting a soluble cancer biomarker. *Lab Chip* 7(10):1288-1293 .
45. Braunwald E (2008) Biomarkers in heart failure. *N Engl J Med* 358(20):2148-2159 .
46. Franzesi GT, Ni B, Ling Y, & Khademhosseini A (2006) A controlled-release strategy for the generation of cross-linked hydrogel microstructures. *J Am Chem Soc* 128(47):15064-15065 .
47. Baumgartner S, Lahajnar G, Sepe A, & Kristl J (2002) Investigation of the state and dynamics of water in hydrogels of cellulose ethers by 1H NMR spectroscopy. *AAPS PharmSciTech* 3(4):E36 .
48. Soppimath KS, Aminabhavi TM, Dave AM, Kumbar SG, & Rudzinski WE (2002) Stimulus-responsive "smart" hydrogels as novel drug delivery systems. *Drug Development and Industrial Pharmacy* 28(8):957-974 .
49. Kulkarni RV & Biswanath S (2007) Electrically responsive smart hydrogels in drug delivery: a review. *Journal of Applied Biomaterials & Biomechanics* 5(3):125-139 .
50. Luo RM, Li H, & Lam KY (2007) Coupled chemo-electro-mechanical simulation for smart hydrogels that are responsive to an external electric field. *Smart Materials & Structures* 16(4):1185-1191 .
51. Santulli C, Patel SI, Jeronimidis G, Davis FJ, & Mitchell GR (2005) Development of smart variable stiffness actuators using polymer hydrogels. *Smart Materials & Structures* 14(2):434-440 .
52. Kim JJ & Park K (1998) Smart hydrogels for bioseparation. *Bioseparation* 7(4-5):177-184 .
53. Peppas NA, Wood KM, & Blanchette JO (2004) Hydrogels for oral delivery of therapeutic proteins. *Expert Opin Biol Ther* 4(6):881-887 .

Chapter 2

A Generalized MRSw Assay Platform

This chapter describes a novel approach for facile derivatization of antibody functionalized MRSw assays. The standard method for sensitizing MRSw nanoparticles towards specific targets involves a chemical conjugation procedure that is both time- and labor-intensive. Our approach is to exploit primary-secondary antibody binding to achieve single-step particle derivatization. Efficacy is demonstrated on *in vivo* derived samples, and the results from a rapidly generated multiplexed experimental setup are shown.

2.1 Motivation

Protein assays are widely used in experimental biology and biochemistry. It is often necessary to customize an assay to be sensitive against a desired target. An important quality of any assay platform is therefore the relative ease with which it can be adapted. The enzyme-linked immunosorbent assay (ELISA) platform is the most popular of customizable assay platforms (1-3). Considerable time and effort is required to produce an ELISA against a specific target. Further reducing ELISA's ease of use is the necessity for numerous wash steps as measurements rely on methods (usually optical) unsuitable for the interrogation of turbid samples. These drawbacks motivate us to develop alternative assay technologies.

Magnetic relaxation switch (MRSw) assays have traditionally consisted of superparamagnetic nanoparticles functionalized with target-specific binding moieties. The particles aggregate in the presence of target analyte and this aggregation changes the transverse relaxation time (T_2) of the aqueous solution under magnetic resonance interrogation (4-7). MRSw assays have been adapted to detect proteins, antibodies, receptor ligands, peptides, nucleic acids, oligonucleotides, and other small molecules. It differs from ELISA in that the readout does not depend on changes in optical properties, thereby eliminating the need for multiple washes and making it potentially well-suited for measuring opaque samples (8).

Antibodies can be and have been conjugated to MRSw to detect a variety of protein targets (9, 10). The chemical functionalization procedure is cumbersome (9). The conjugation chemistry can take over 12 hours to complete and the nominal valency of the particles is difficult to control even under carefully managed conditions. We illustrate here how to exploit primary-secondary antibody binding so that a single set of particles can be used as a generalized pool from which subsets of particles may be rapidly derivatized to target specific protein markers. We further demonstrate the application of this approach to be facile and inexpensive in producing multiplexed assays.

2.2 Derivatization Strategy

Our strategy relies on primary-secondary antibody binding (Figures 2.1a and 2.1b) to achieve derivatization through single-step incubations. The term secondary antibody refers in this chapter to antibodies specific for other *antibodies* and the term primary antibody to antibodies specific for *non-antibody protein targets of interest.* This method allows for the use of primary antibodies generated in any host species so long as the secondary antibodies are appropriately matched. These results, unless otherwise specified, were obtained using particles conjugated to anti-goat secondary antibodies (NM-[aGoat]) but we will also show the response of particles sensitive for human chorionic gonadotrophin (hCG) which were derivatized from NM-[aMouse]. It is important to note that since polyclonal secondary antibodies recognize multiple epitopes on primary antibodies, the strict use of monoclonal secondary antibodies is important for the stability of NM-[aGoat]. Specifically, the use of monoclonal as opposed to polyclonal antibodies will circumvent the possibility of direct cluster formation resulting from derivatization (Figure 2.1c).

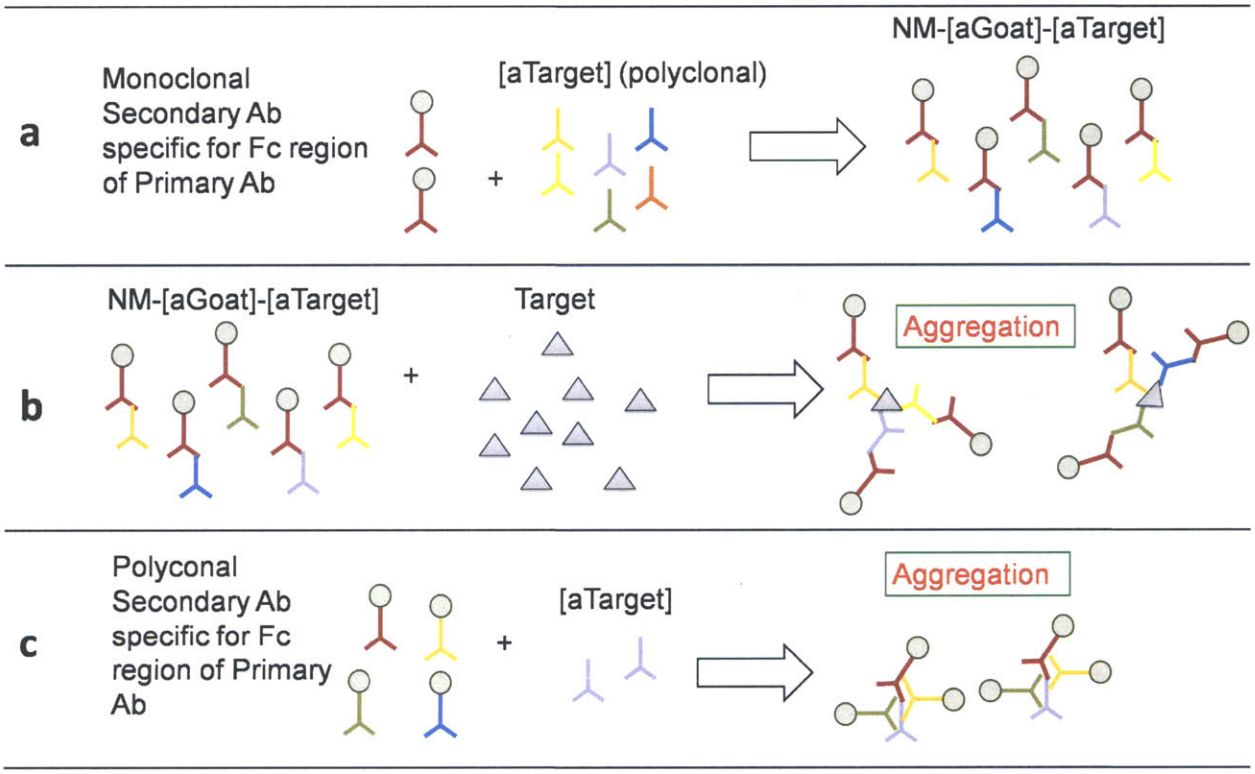

Figure 2.1 **a,** This approach utilizes a base set of NM-[aGoat] particles with which polyclonal primary antibodies sensitive towards specific targets may be attached by direct incubation. **b,** Derivatized nanoparticles can then interact with target molecules to form aggregates. **c,** If the secondary antibodies used are polyclonal rather than monoclonal, the derivatization step may result in unwanted aggregate formation and T_2 change.

2.3 Assay Response and Characterization

Control experiments using human cardiac troponin I (TNI) as a model analyte were first performed to determine the efficacy of this derivatization strategy. Non-derivatized NM-[aGoat] particles exhibited no significant T_2 change in the presence of TNI (Figure 2.2a) while NM-[aGoat]-[aTNI] was T_2 responsive (Figure 2.2b). Figure 2.2b depicts a representative T_2 time course upon addition of analyte; for clarity all subsequent results are reported as the difference between experimental and control values (ΔT_2) at the 12 hr time point. We emphasize that the assay can provide sufficient resolution as soon as one hour after analyte addition (Figure 2.3) although the required duration is expected to vary for different antibodies and targets used.

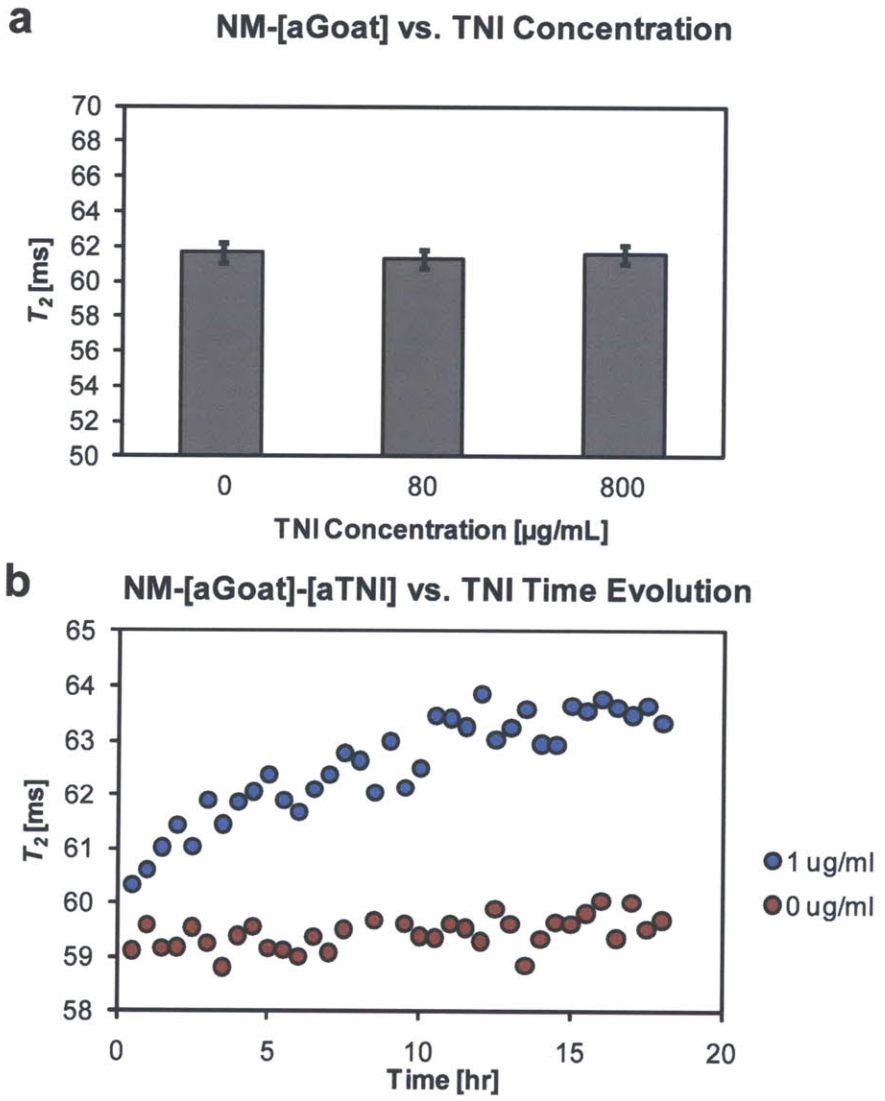

Figure 2.2 **a,** T_2 of NM-[aGoat] nanoparticles incubated with TNI analyte was assessed 12 hours after addition of analyte (n=3, error bars give standard error). **b,** A time-course study of T_2 change after analyte addition (which occured at the 0 hr time point) shows stabilization after approximately 12 hours (blue) while the control condition (red) remains stable over the same duration. The measurement error of each time point (omitted to facilitate uncluttered visualization) is ~0.5-0.7 ms.

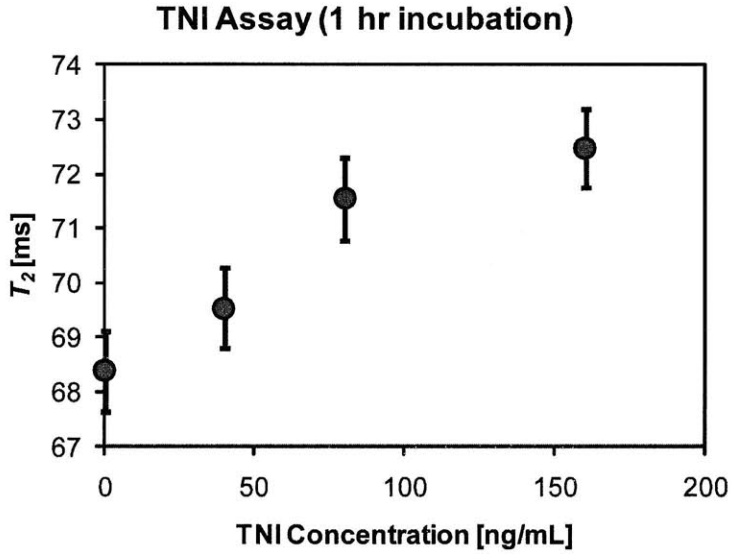

Figure 2.3 A troponin assay shows marked changes only 1 hr after analyte addition. The data is plotted as the mean of n=3 samples and error bars correspond to the standard error.

Previous studies of MRSw behavior (9) showed T_2 to decrease with the introduction of analyte but we find T_2 increases in this assay. The present model for a decreasing T_2 assumes that particle clusters are more efficient at dephasing the proton nuclear spins than dispersed particles (11, 12). Importantly, this model relies on solution stability of the particles both before and after aggregation as T_2 is measured from a fixed sample volume. A matched-pair of monoclonal antibodies was used in previous studies to limit the size of formed complexes but the use of polyclonal antibodies in this work permits the formation of large complexes. We reasoned that such large aggregates should possess decreased colloidal stability and precipitate. The precipitates cannot contribute to the measured T_2 signal so the effective nanoparticle concentration in solution would be decreased. A comparison of the iron content in the supernatant of samples to which analyte had been added or withheld is consistent with this hypothesis; ICP-AES analysis shows a 17% reduction in iron content (Figure 2.4). Dynamic light scattering tests further show that analyte introduction reduces the average diameter of the particle clusters as well as the total number of clusters that remain in solution. These results together indicate that precipitation is the likely driver of T_2 contrast exhibited by these assays.

An important advantage of our derivatization approach is the ease with which nominal valency (the concentration of primary antibodies incubated with a fixed number of nanoparticles) can be controlled. Particle valency in direct conjugation (9) is fixed at the chemical coupling stage in which large amounts of antibody must be used. Valency is controlled here by simply varying the far smaller concentrations of the incubated primary antibody. A nominal valency that maximizes ΔT_2 for a given analyte concentration can be seen in Figure 2.5. This result is consistent with the notion that there may be some maximum nominal valency at which the binding pockets of the secondary antibodies become saturated. Higher real valencies (the actual number of primary antibodies attached to nanoparticles) naturally increase the likelihood that large complexes would form and

	+ TNI	-TNI	% Change
Fe [ug/mL]	11.616	13.989	16.92%

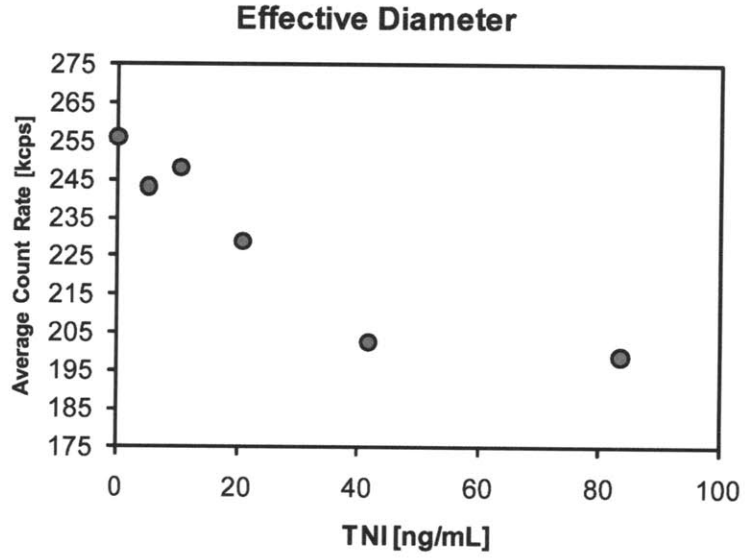

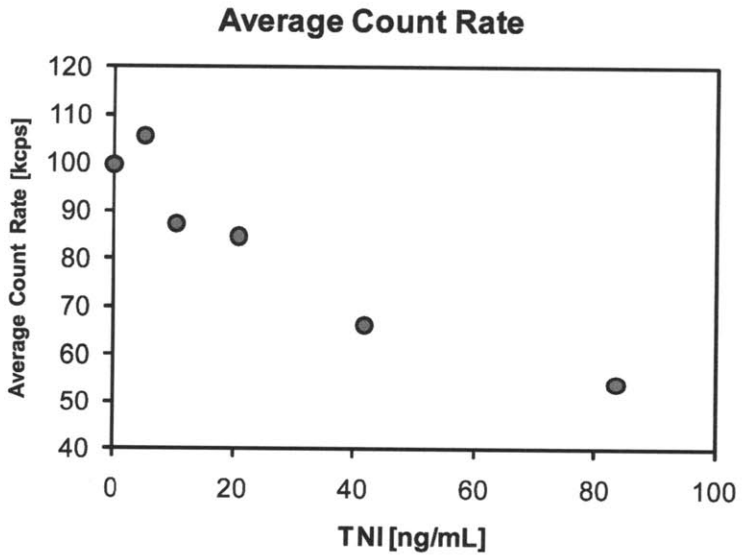

Figure 2.4 Particle precipitation induces T_2 change. The upper table gives the iron concentration of a NM-[aGoat]-[aTNI] assay supernatant with and without the addition TNI analyte (as measured by ICP). The lower graphs show particle diameters and concentrations measured from sample supernatants. The decrease in effective diameter indicates that larger particles have precipitated from solution. The decrease in average count rate in kilo-counts per second (kcps) of particles is also consistent with precipitation.

precipitate in the presence of analyte to produce a T_2 change. The addition of primary antibodies to particles with already saturated binding sites, however, results in free-floating primary antibodies that can bind to analyte molecules but do not contribute to cluster formation. They would instead be expected to sequester analyte and inhibit the formation of aggregates.

The response curve of T_2 vs. TNI depicted in Figure 2.6 is approximately linear ($R^2 = 0.997$) in the physiologically relevant range of 5-80 ng/mL. The LOD in this assay is 8.6 ng/mL while the LOQ is 28.4 ng/mL. The specific model analyte used here is TNI but a similar T_2 dependence was found in a myoglobin assay (Figure 2.7). Note also that this assay is responsive despite the further addition of 50% FBS. MRSw particles derivatized through this primary-secondary strategy are clearly robust to the presence of FBS-associated proteins and ions. Any future quantitative assay will require standards against which experimental values are calibrated; the issues of a linear range, LOD, and LOQ will similarly need to be individually characterized for each combination of target analyte, primary antibody, secondary antibody, and sample media used. The generalized MRSw protein assay is no different in this respect from ELISA or most other existing assays.

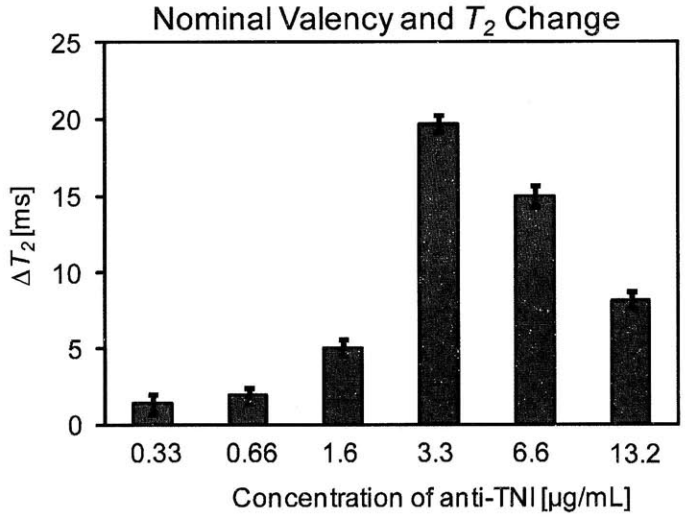

Figure 2.5 Nominal valency of the nanoparticles can be controlled by varying the concentration of primary antibodies incubated. Addition of a fixed concentration of TNI analyte (800 ng/ml) induces T_2 changes that vary with the effective valency of the nanoparticles. The data is plotted as the mean of n=3 samples and error bars correspond to the standard error.

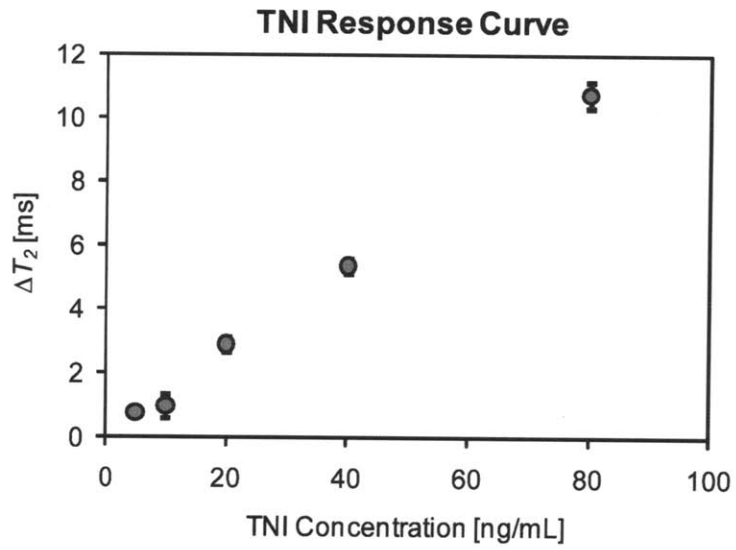

Figure 2.6 The assay is quantitative. A TNI response curve is shown for which a nominal valency of 3.3 μg/ml of [aTNI] was used. The data is plotted as the mean of n=3 samples and error bars correspond to the standard error.

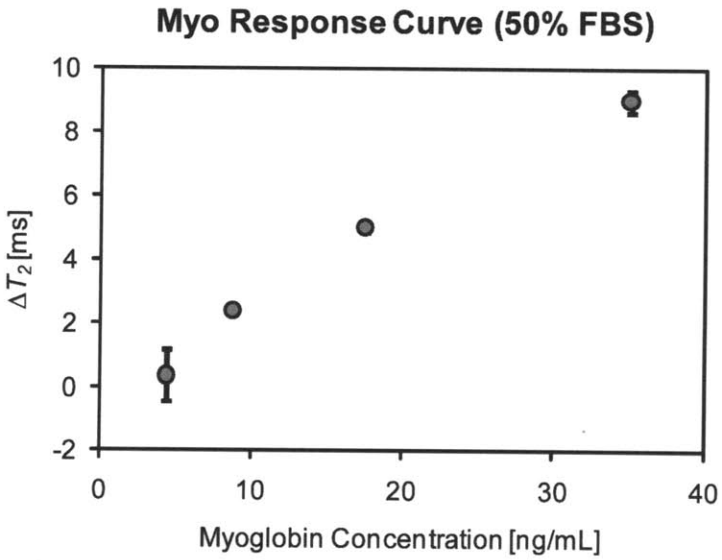

Figure 2.7 The assay can also be adapted to detect Myoglobin, and remains quantitative when FBS is added at 50% v/v. The data is plotted as the mean of n=3 samples and error bars correspond to the standard error.

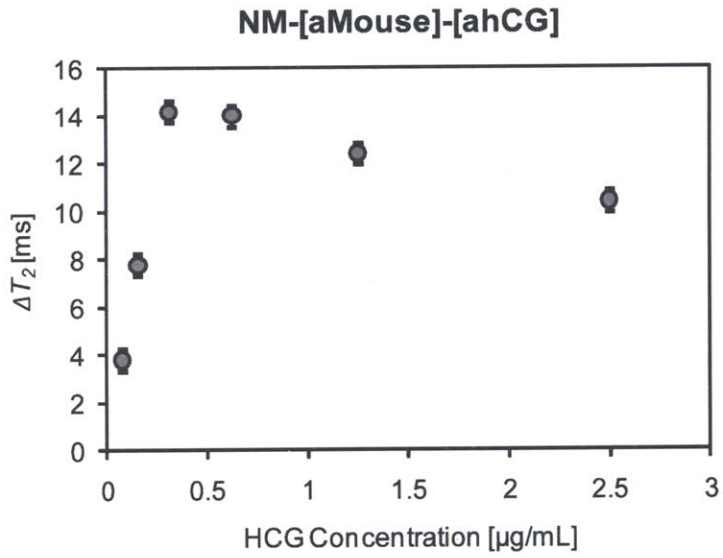

Figure 2.8 This hCG assay uses NM-[aMouse] as opposed to NM-[aGoat]. Our derivatization strategy therefore does not require the use of any particular secondary antibody as long as it is paired with primary antibodies generated in the appropriate species. The data is plotted as the mean of n=3 samples and error bars correspond to the standard error.

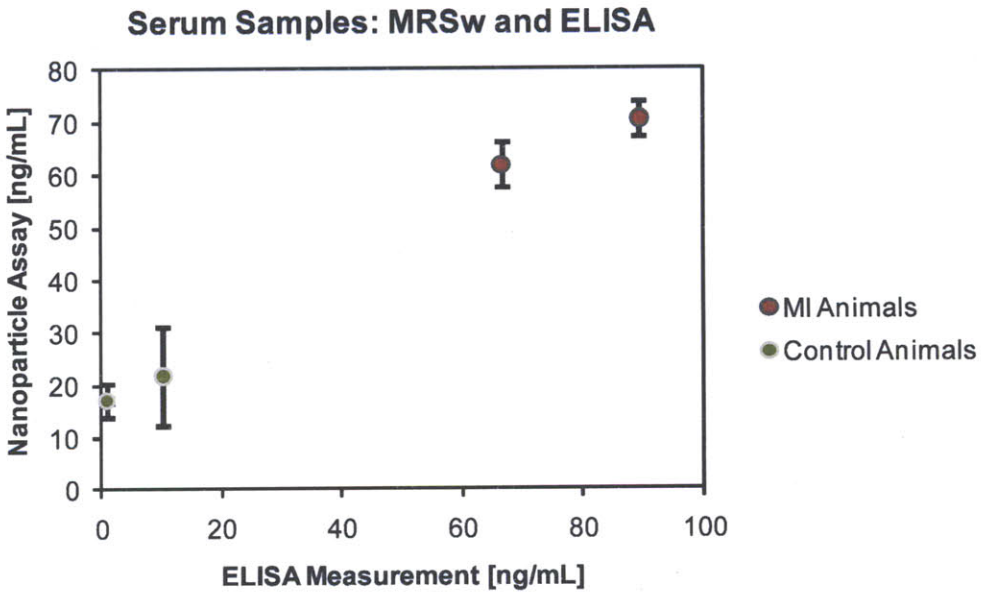

Figure 2.9 MRSw assay measurements of serum samples plotted against their ELISA counterparts show the assay to be effective for quantifying *in vivo* derived material. NM-[aGoat] particles without aMyo secondary antibodies were used as a control and exhibited no T_2 response. The samples were diluted 10X in PBS/BSA prior to measurement. The data is plotted as the mean of n=3 samples and error bars correspond to the standard error.

We compared the performance of a MRSw assay derivatized using the primary-secondary strategy to that of a commercially-obtained ELISA kit; the myoglobin contents of serum samples were determined using both methods (Figure 2.9). These results were the first confirmation that this generalized assay platform is robust and sensitive towards *in vivo* derived samples, and a precursor to the *in vivo* work described in Chapter 3. We also tested the efficacy of particles functionalized with anti-mouse secondary antibodies (Figure 2.8) by using hCG as a model target analyte. The assay's response confirms that the derivatization strategy described in this chapter does not depend on the use of any particular type of primary antibody. This hCG result also shows a saturation of the assay above the 'linear' range falling below 0.5 μg/mL of analyte; the effect was expected and consistent with previously reported findings.

Finally, we investigated the ease with which these assays can be multiplexed by derivatizing NM-[aGoat] particles against three model targets of interest (Figure 2.10). The results show that T_2 change is not uniform for all analytes even when analyte concentration and nominal valency are held constant. We did not expect uniformity here because the number of potential antibody binding sites varies with the size and specific properties of each target analyte, and populations of polyclonal antibodies are in general different from one another. It is true that a reliance on aggregate precipitation increases the complexity of this system in comparison to standard MRSw assays, and that precipitation (and subsequent T_2 change) is influenced by additional factors such as sample viscosity and temperature. These additional factors, however, do not prevent the system from giving quantitative results; the data presented here shows an unambiguous T_2 dependence on analyte concentration.

2.4 Conclusions

We have shown that primary-secondary antibody binding may be incorporated into MRSw assays to facilitate single-step particle derivatization. This simple but effective method allows for particle sets and antibodies to be treated as modular components, thus enabling rapid multiplexing. The derivatization strategy is robust and efficacious for measuring *in vivo* derived samples as well. The contrast mechanism differs from the aggregation-based relaxivity enhancements seen in traditional MRSw assays but nonetheless allows for the quantification of target analyte.

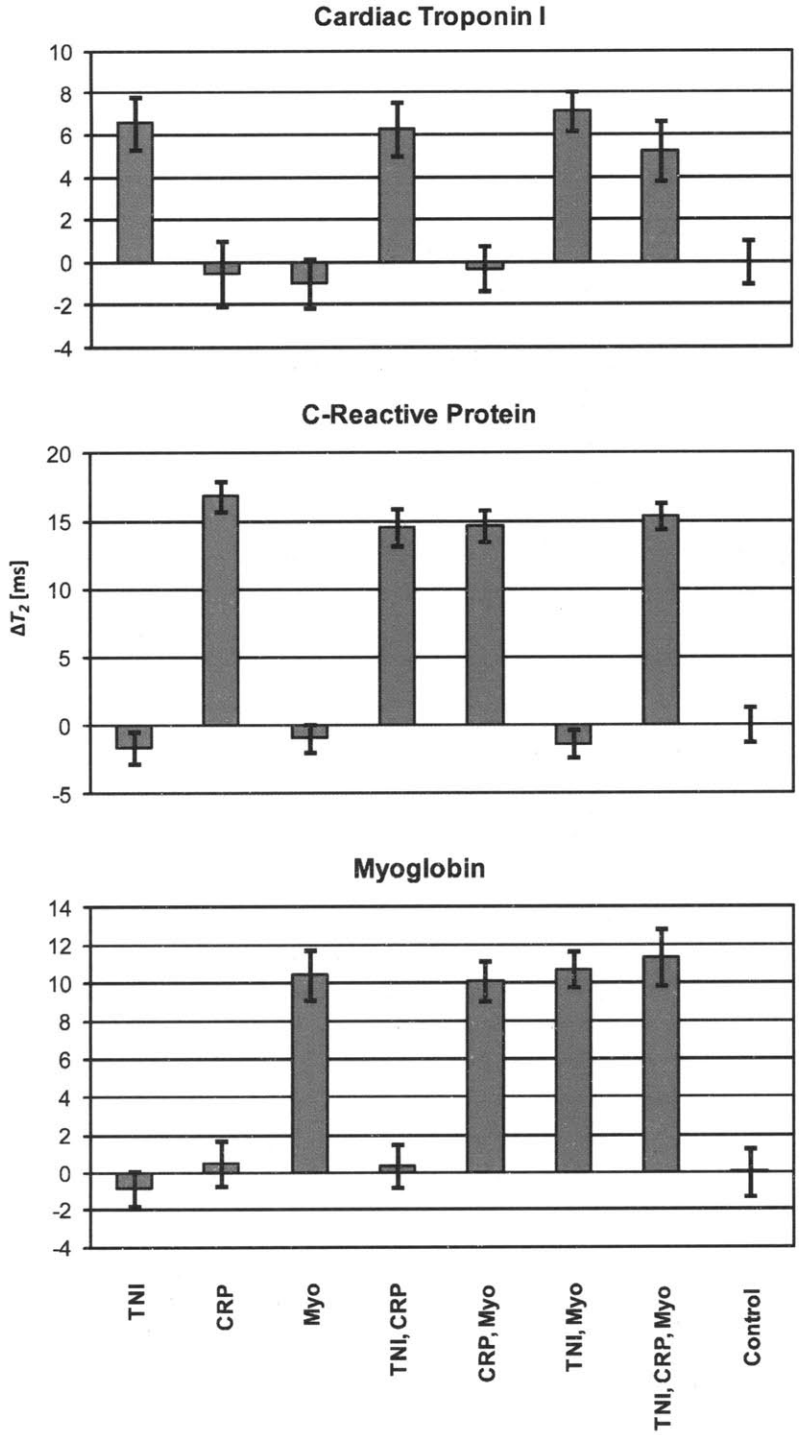

Figure 2.10 Target-specific nanoparticles against TNI, C-Reactive Protein (CRP), and Myoglobin were derivatized from the generic NM-[aGoat] population and used to assay various test mixtures. Each graph corresponds to an assay for a specific target; each column corresponds to a specific mixture that included one or more of the target analytes (with the exception of the control column). Error bars correspond to a 95% confidence interval for the fit.

2.5 Materials and Methods

2.5.1 Nanoparticle Conjugation

NanoMag-CLD (30 nm diameter) magnetic iron oxide nanoparticles with amine terminated dextran shells (Micromod) were conjugated to a monoclonal antibody against goat IgG (Meridian Life Sciences) using a previously described method (13). Nanoparticle surfaces were activated by 1 hr incubation at a ratio of 1:6 w/w with sulfo-succinimidyl-4-(*N*-maleimidomethyl)cyclohexane-1-carboxylate dissolved 60:1 w/v in dimethyl sulfoxide (Sigma-Aldrich). Antibodies were activated by 1 hr incubation at a ratio of 30:1 w/w with 12.5 mM N-succinimidyl-S-acetylthioacetate (Pierce) dissolved in dimethyl sulfoxide and de-acetylated over 2 hr by addition of 25 μL 0.5 M hydroxylamine hydrochloride (Sigma-Aldrich) dissolved in PBS buffer (containing 25 mM EDTA). These components were then purified by PD-10 desalting columns (GE Healthcare), mixed and left to incubate overnight to allow for chemical coupling, and quenched by 0.1% mercaptoethanol. Excess free antibodies were removed from the conjugated nanoparticles by purification through magnetic MACS Cell Separation LS columns (Miltenyi Biotec). 10 mM EDTA dissolved in PBS was used as the buffer for both the de-salting and magnetic columns. Iron concentrations were determined by Inductively Coupled Plasma Atomic Emission Spectroscopy (ICP-AES) after dissolution of samples in 6N HCl and H_2O_2 for 24 hours. Protein concentrations were determined with a bicinchoninic acid assay (Pierce).

2.5.2 Derivatization

NanoMag particles conjugated with anti-goat antibodies (NM-[aGoat]) were incubated with goat-produced polyclonal antibodies. The polyclonal antibody concentration was varied to control nominal valency, which we define to be the number of primary antibodies incubated per unit of nanoparticles. Unless otherwise specified, NM-[aGoat] (44 μg/ml iron concentration) was mixed at equal volumes with 3.29 μg/ml Goat anti-Human Cardiac Troponin I (BiosPacific, Emeryville, CA), 3.5 μg/ml Goat anti-Human Myoglobin (BiosPacific, Emeryville, CA), and 4 μg/ml Goat anti-Human C-Reactive Protein (BiosPacific, Emeryville, CA). The mixture incubated for one hour at room temperature before use as an assay reagent. Human myoglobin and human C-reactive protein were obtained from BiosPacific while human cardiac troponin I was obtained from CalBiochem, La Jolla, CA.

2.5.3 Determination of Proton Relaxation Time

Proton relaxation measurements were determined on custom-built system using a single-sided nuclear magnetic resonance (NMR) sensor[11] (0.43 T and 25°C; Profile NMR MOUSE, ACT Center for Technology, Aachen, Germany). The sensor's field gradient enables measurements to be made on a single well of a 96-well microplate positioned above the sensor. The single-sided NMR sensor was retrofitted with a programmable motion stage that moved the microplate over the sensor and enabled automated measurement of the entire plate. Transverse relaxation times for the single-sided MR ($T_{2,eff}$) were measured using a Carr Purcell Meiboom Gill (CPMG) sequence with the following parameters: echo time (TE) = 0.035 ms, 5714 echoes, 16 scans, and recovery time (TR) = 3 s. The echo peak intensities were fit to the equation $I = I_0 e^{-t/T2}$ using a custom script running on MATLAB (The Mathworks, Natick, MA). Transverse relaxation time constants measured on the single-sided system are lower than T_2 measured on a homogeneous field magnet system. The amount by which

the value is reduced is dependent upon the field gradient, the pulse sequence parameters and a combination of the sample's T_1 and T_2.[12] The measured time constant is thus reported as an effective T_2 ($T_{2,eff}$) . Assay proton relaxation time measurements were made 12 hrs after mixing equal volumes of assay reagent with analyte. Unless otherwise specified, analytes were diluted in phosphate buffered saline (Gibco) with 1% bovine serum albumin (Sigma) and 0.1% Penicillin-Streptomycin (Gibco) to minimize non-specific adsorption. Serum samples from control and MI mouse models were provided as a gift by Terrence Pong (Cardiovascular Research Laboratory, Massachusetts General Hospital). Reported concentrations are the final concentrations after mixing.

2.5.4 Determination of Limit of Detection (LOD)

The limit of detection (LOD) and the limit of quantitation (LOQ) were defined statistically as 3 standard and 10 standard deviations above the mean reading of the control samples.(14) The reported concentration limit values were extrapolated from a linear fit of the data.

2.5.5 Dynamic Light Scattering

Particle sizes were determined using a 90 Plus Particle Size Analyzer (Brookhaven Instrument Corporation, Holtsville, NY). Samples were measured at 37°C in PBS/BSA, λ = 658 nm, 90 degree fixed angle. The log-normal intensity weighted effective diameter was reported. The population distribution was determined by peak integration of the volume-weighted scattering intensity.

2.6 References

1. Engvall E & Perlmann P (1971) Enzyme-linked immunosorbent assay (ELISA). Quantitative assay of immunoglobulin G. *Immunochemistry* 8(9):871-874 .
2. Engvall E, Jonsson K, & Perlmann P (1971) Enzyme-linked immunosorbent assay. II. Quantitative assay of protein antigen, immunoglobulin G, by means of enzyme-labelled antigen and antibody-coated tubes. *Biochim Biophys Acta* 251(3):427-434 .
3. Engvall E & Perlmann P (1972) Enzyme-linked immunosorbent assay, Elisa. 3. Quantitation of specific antibodies by enzyme-labeled anti-immunoglobulin in antigen-coated tubes. *J Immunol* 109(1):129-135 .
4. Perez JM, O'Loughin T, Simeone FJ, Weissleder R, & Josephson L (2002) DNA-based magnetic nanoparticle assembly acts as a magnetic relaxation nanoswitch allowing screening of DNA-cleaving agents. *J Am Chem Soc* 124(12):2856-2857 .
5. Perez JM, Josephson L, O'Loughlin T, Hogemann D, & Weissleder R (2002) Magnetic relaxation switches capable of sensing molecular interactions. *Nat Biotechnol* 20(8):816-820 .
6. Tsourkas A, Hofstetter O, Hofstetter H, Weissleder R, & Josephson L (2004) Magnetic relaxation switch immunosensors detect enantiomeric impurities. *Angew Chem Int Ed Engl* 43(18):2395-2399 .
7. Taktak S, Sosnovik D, Cima MJ, Weissleder R, & Josephson L (2007) Multiparameter magnetic relaxation switch assays. *Anal Chem* 79(23):8863-8869 .
8. Daniel KD, *et al.* (2007) Multi-reservoir device for detecting a soluble cancer biomarker. *Lab Chip* 7(10):1288-1293 .
9. Kim GY, Josephson L, Langer R, & Cima MJ (2007) Magnetic relaxation switch detection of human chorionic gonadotrophin. *Bioconjug Chem* 18(6):2024-2028 .
10. Sun EY, Weissleder R, & Josephson L (2006) Continuous analyte sensing with magnetic nanoswitches. *Small* 2(10):1144-1147 .
11. Brooks RA, Moiny F, & Gillis P (2001) On T2-shortening by weakly magnetized particles: the chemical exchange model. *Magn Reson Med* 45(6):1014-1020 .
12. Shapiro MG, Atanasijevic T, Faas H, Westmeyer GG, & Jasanoff A (2006) Dynamic imaging with MRI contrast agents: quantitative considerations. *Magn Reson Imaging* 24(4):449-462 .
13. Josephson L, Tung CH, Moore A, & Weissleder R (1999) High-efficiency intracellular magnetic labeling with novel superparamagnetic-Tat peptide conjugates. *Bioconjug Chem* 10(2):186-191 .
14. Armbruster DA, Tillman MD, & Hubbs LM (1994) Limit of detection (LQD)/limit of quantitation (LOQ): comparison of the empirical and the statistical methods exemplified with GC-MS assays of abused drugs. *Clin Chem* 40(7 Pt 1):1233-1238 .

Chapter 3

In Vivo Sensing of Myocardial Infarction

Molecular biomarkers are frequently measured when attempting to assess the status of pathological processes. Biomarker levels change over time but clinical measurement is often constrained to a single time point. The ability to measure their dynamic time course could be clinically valuable but existing methods for doing so are invasive and impractical. We report in this chapter on implantable molecular sensors that integrate analyte exposure over time. The sensors possess magnetic nanoparticles, engineered to bind designated targets, which can be monitored non-invasively through magnetic resonance relaxometry. We test their response in a murine model of myocardial infarction to determine efficacy in measuring clinically relevant biomarkers at physiological levels. Sensor response differs between MI vs. control groups and correlates with infarct size. Alternative applications are numerous and we further demonstrate these sensors as a tool in assaying the cardiotoxicity of a chemotherapeutic.

3.1 Myocardial Infarction

3.1.1 Pathophysiology and Clinical Presentation

Myocardial infarctions, or heart attacks, frequently strike patients suffering from chronic cardiac disease (1). The acute process involves the obstruction of a major cardiac artery resulting in ischemia-induced necrosis of myocardium (Figure 3.1). Such obstructions usually arise from thrombus formation secondary to atherosclerotic plaque ruptures. Affected cardiomyocytes can survive for some duration after cessation of perfusion so cell death does not immediately follow ischemia. The length of the duration depends on the degree of ischemia and the presence of collateral circulation (complete death of the entire afflicted zone usually takes 4-6 hours). MI appears, by histology, as necrotic zones ringed by a gradient of progressively healthier tissue.

Occlusion site dictates the severity of a MI. Blockage of a large feeder vessel (such as the left anterior descending artery) can cause severe impairment of heart function while micro-infarcts in small vessels can be functionally inconsequential. The occlusion site also dictates the location of the infarct zone, be it anterior, lateral, inferior, posterior, or septal (or some combination). An upstream lesion, as at site A in Figure 3.1, afflicts a much larger (lightly shaded area) amount of tissue than does a downstream lesion at site B (darkly shaded). First-line pharmacotherapy consists of thrombolytic agents and anticoagulants which obliterate the obstruction, as well as beta blockers that reduce myocardial oxygen demand. Surgical intervention such as coronary artery bypass or stent placement can then be deployed to physically circumvent the site of obstruction. Cardiac myocytes transition from a stunned/shocked state to death over a finite period of time, so such reperfusion therapies can often salvage ischemic but still viable tissue. The American College of Cardiology's classification scheme for MI is reproduced in Table 3.1.

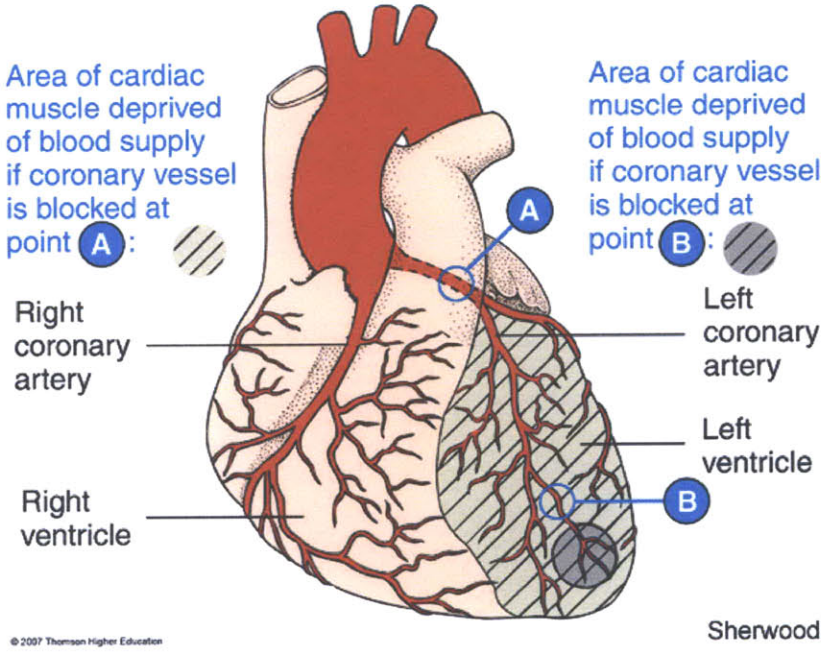

Figure 3.1 Myocardial infarction is characterized by ischemic myocardial death resulting from cardiac artery obstruction. This schematic shows that arterial obstruction at differing sites can produce differing degrees of cell death. Reproduced from Thomson Higher Education.

Classification	Infarction Size
Small	<10% of the left ventricle
Medium	10-30% of the left ventricle
Large	>30% of the left ventricle

Table 3.1 Classification of MI size

MI patients usually complain at presentation of left chest pain ("an elephant sitting on my chest") radiating to the arm, jaw, back, or shoulder. Discomfort is almost always dull and diffuse rather than sharp and localized, and commonly accompanied by vomiting, dizziness, syncope, and/or shortness of breath. Most MI patients possess some subset of these symptoms though others experience none at all. Those in the latter group are subject to greater risk as they do not seek medical treatment. The Framingham study found that acute instances of MI were not recognized in 26% of men and 34% of women. "Approximately half of the [patients in this group] had no symptoms whatsoever, whereas the remainder experienced nonspecific symptoms that at the time were not perceived to be the consequence of myocardial infarction" (2). Early clinical intervention is important for saving ischemic myocardium ("time is muscle") so the high incidence of unrecognized and un-treated MI is an important public health concern.

3.1.2 Diagnosis

Acute onset of MI can be diagnosed through "pathologic examination, measurement of myocardial proteins in the blood, ECG recordings (ST-T segment wave changes, Q waves), imaging modalities such as myocardial perfusion imaging, echocardiography and contrast ventriculography" (3). Table 3.2 provides a summary of the common pathological findings under each modality.

Modality	Finding
Pathology	Myocardial cell death
Biochemistry	Markers of myocardial cell death recovered from blood samples
Electrocardiography	Evidence of myocardial ischemia (ST-T segment changes) Evidence of loss of electrically functioning cardiac tissue (Q waves)
Imaging	Reduction or loss of tissue perfusion Cardiac wall motion abnormalities

Table 3.2 Aspects of MI by Different Techniques. Reproduced from Alpert, *et al.*(3)

We focus in this chapter on functional proteins—cardiac Troponin I (TNI), Myoglobin (Myo) and CK-MB—MI biomarkers that leach from necrotic myocardium after an acute infarction. The serum dynamics of these markers are well studied: Myoglobin rises and falls rapidly over 24 hours while CK-MB remains above baseline for 3-4 days and Troponin I for 7-10 days. Clinically, serum levels above the 99th percentile of the normal population are considered confirmatory of MI. The actual magnitudes of the measurements are not used to predict infarct size because of individual-to-individual variation and timing uncertainties. The diagnostic value of these three markers also varies. TNI possesses a near complete specificity for MI while CK-MB is less cardiac specific. Myoglobin is a marker of general muscle damage but is nonetheless useful when measured in combination with TNI and CK-MB in the standard cardiac panel. Figure 3.2 shows typical temporal release profiles of each of the three biomarkers. Cardiac biomarker elevation satisfies the clinical standard for diagnosis of acute MI. We are thus motivated to develop sensors capable of monitoring and quantifying them.

3.2 Motivation

Magnetic resonance is an attractive output for implanted sensors because it can be measured non-invasively through tissue. Daniel *et al.* (4) first described the use of MRSw sensors for *in vivo* detection of a soluble protein biomarker. They targeted human chorionic gonadotropin, a marker of testicular and ovarian cancer (5-7), in a murine model. Functionalized MRSw were adapted for *in vivo* use by encapsulation of the nanoparticles within small discrete substrates enclosed by size-exclusion membranes (Figure 3.3a). A membrane pore size between that of the nanoparticles and the target analyte was chosen to prevent the escape of nanoparticles while allowing for the inward diffusion of analyte. Sensor efficacy was tested by implantation within mice possessing xenografted hCG-releasing tumors (Figure 3.4); measurements were made with both a single-sided proton NMR relaxometer on explanted sensors and a MRI scanner on still-implanted sensors. Their results demonstrate that MRSw enclosed within small discrete volumes can indeed be made to detect soluble markers.

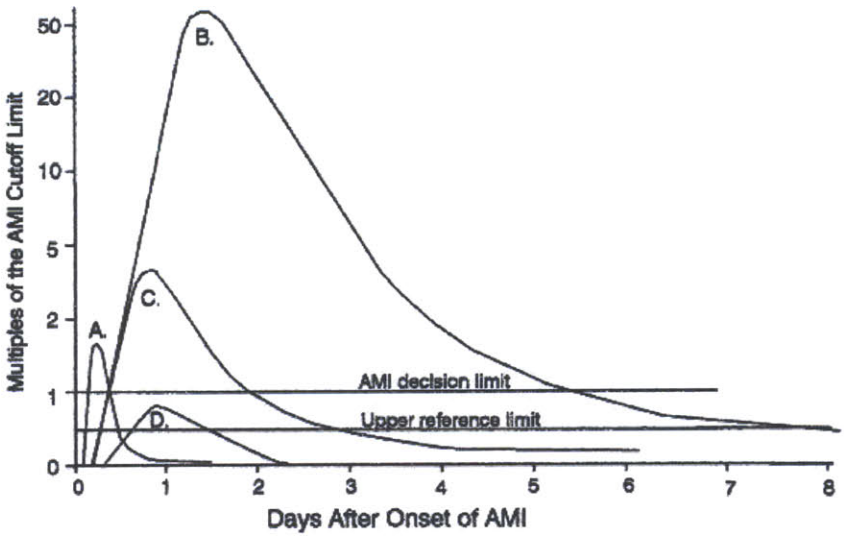

Figure 3.2 Timing of release of various biomarkers following acute, ischemic myocardial infarction. Peak A, early release of Myoglobin after AMI; peak B, cardiac Troponin after AMI; peak C, CK-MB after AMI; peak D, cardiac Troponin after unstable angina. Data are plotted on a relative scale, where 1.0 is set at the AMI cutoff concentration. Reproduced from Wu *et al.*(8)

Cancer is an inherently heterogeneous disease. With the exception of prostate specific antigen (for prostate cancer), no biomarkers are currently used for the clinical diagnosis of cancer. Animal models of cancer are also rather poor proxies for the disease. Daniel *et al.*, for instance, grew tumors within mice by exogenous seeding of hCG-releasing cells. They found that tumor growth was poorly controlled; the lesions developed to different sizes, released very different levels of hCG, and did so at far higher levels than would have been found in 'normal' cancers. There was poor correspondence between naturally occurring ovarian/testicular cancer and their model.

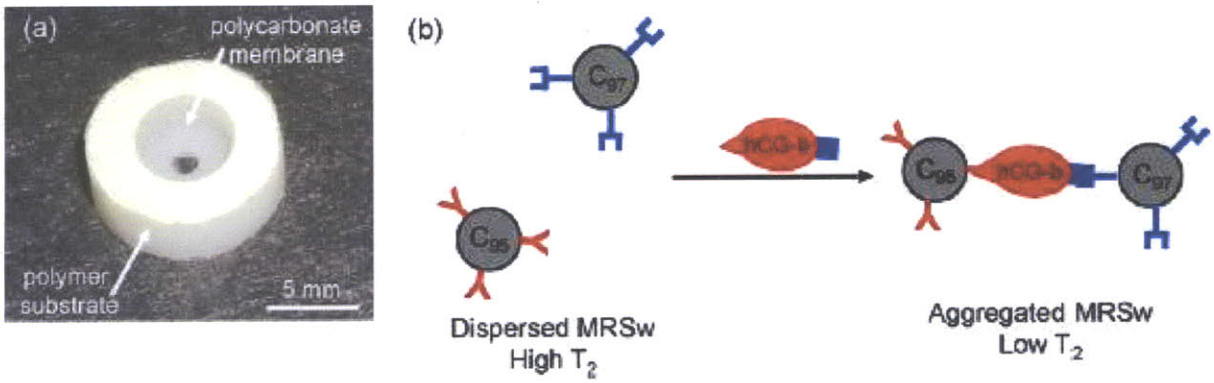

Figure 3.3 a, Photograph of *in vivo* device and **b**, schematic of MRSw aggregation. Two populations of MRSw, each functionalized with a different monoclonal antibody for HCG. Both particle populations must be present for aggregation of MRSw to occur. Reproduced from Daniel *et al.(4)*

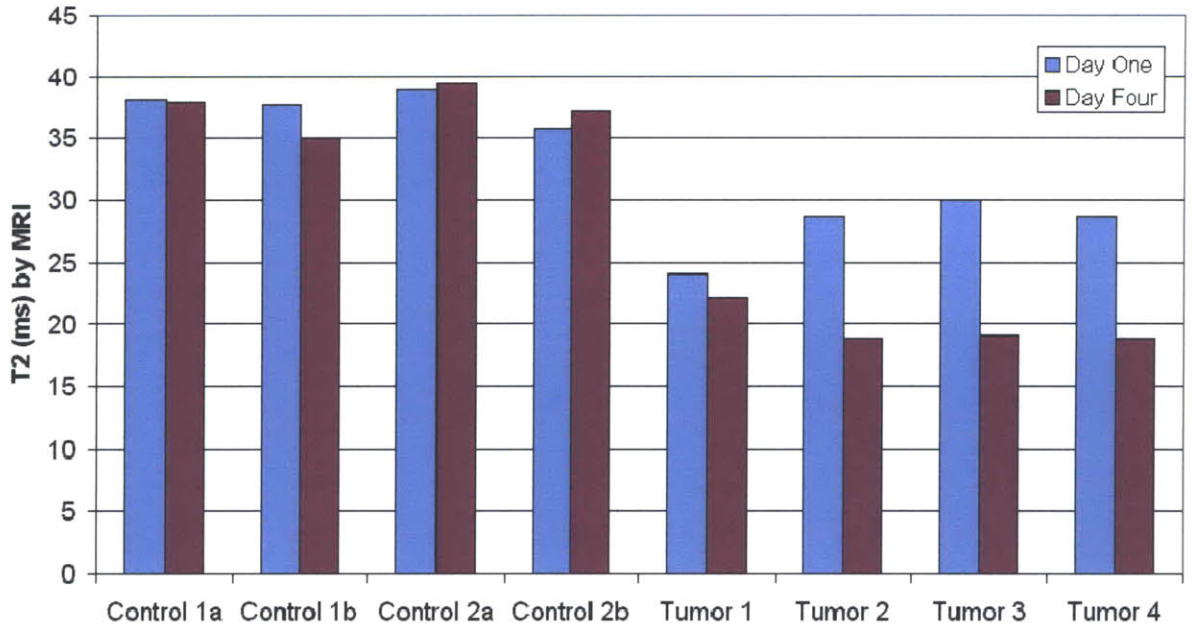

Figure 3.4 T_2 values from MR imaging on days 1 and 4 post-device implantation (error bars represent standard error of measurement). The T_2 values of the four control devices are essentially constant over the two time points, indicating that the MRSw did not aggregate or leak from the device. T_2 values for the sample devices are lower than the control devices at both time points. Reproduced from Karen *et al.*(4)

We describe, in this chapter, the application of MRSw sensors to the *in vivo* detection and measurement of cardiac (or myocardial infarction-associated) biomarkers. MI detection is particularly attractive for this technology because, 1) a panel of three clinically validated cardiac markers exists, 2) the model we use to study MI generates physiological biomarker release, and 3) the sensor measurements can be directly compared with MI size. We investigate the performance of subcutaneously implanted MRSw sensors in detecting physiologically relevant concentrations of clinically validated biomarkers. A left anterior descending (LAD) artery ligation procedure described by Michael *et. al.* (9) was adapted to experimentally replicate myocardial infarction in a C57BL6 murine model.

3.3 Extravasation of Cardiac Biomarkers

The sensors are discrete and designed to sample from the subcutaneous flank when placed *in vivo*. Our intended cardiac targets, traditionally measured in serum (Figure 3.5), must therefore extravasate at measurable concentrations to the flank if *in situ* sensing is to be achieved. Serum levels of cardiac biomarkers after acute MI are well-characterized in the existing literature (10, 11), but their extravasation to the subcutaneous flank had not previously warranted study. We thus experimentally determined the extravasation dynamics (Figure 3.6) under three conditions (summarized Table 3.3). These results confirm the subcutaneous potential space as a viable site for cardiac biomarker detection.

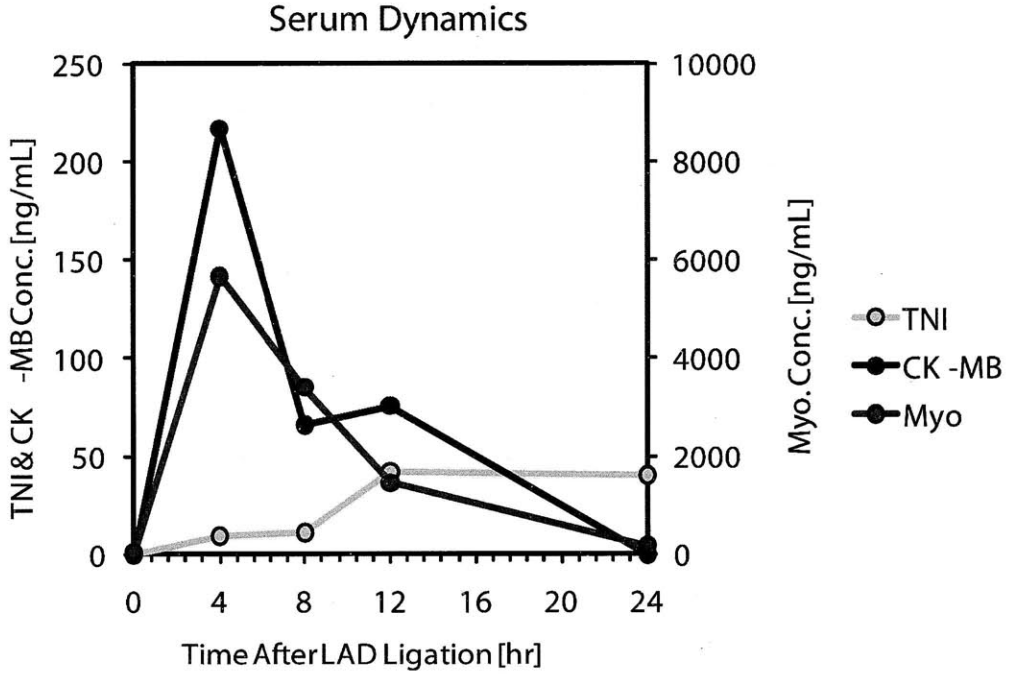

Figure 3.5 Empirically determined serum TNI, Myoglobin and CK-MB levels after LAD ligation are consistent with literature results and confirm the validity of the MI model used in this study. Measurements were made using ELISA and plotted as the mean of n=4 samples. Error bars are omitted to allow for uncluttered visualization.

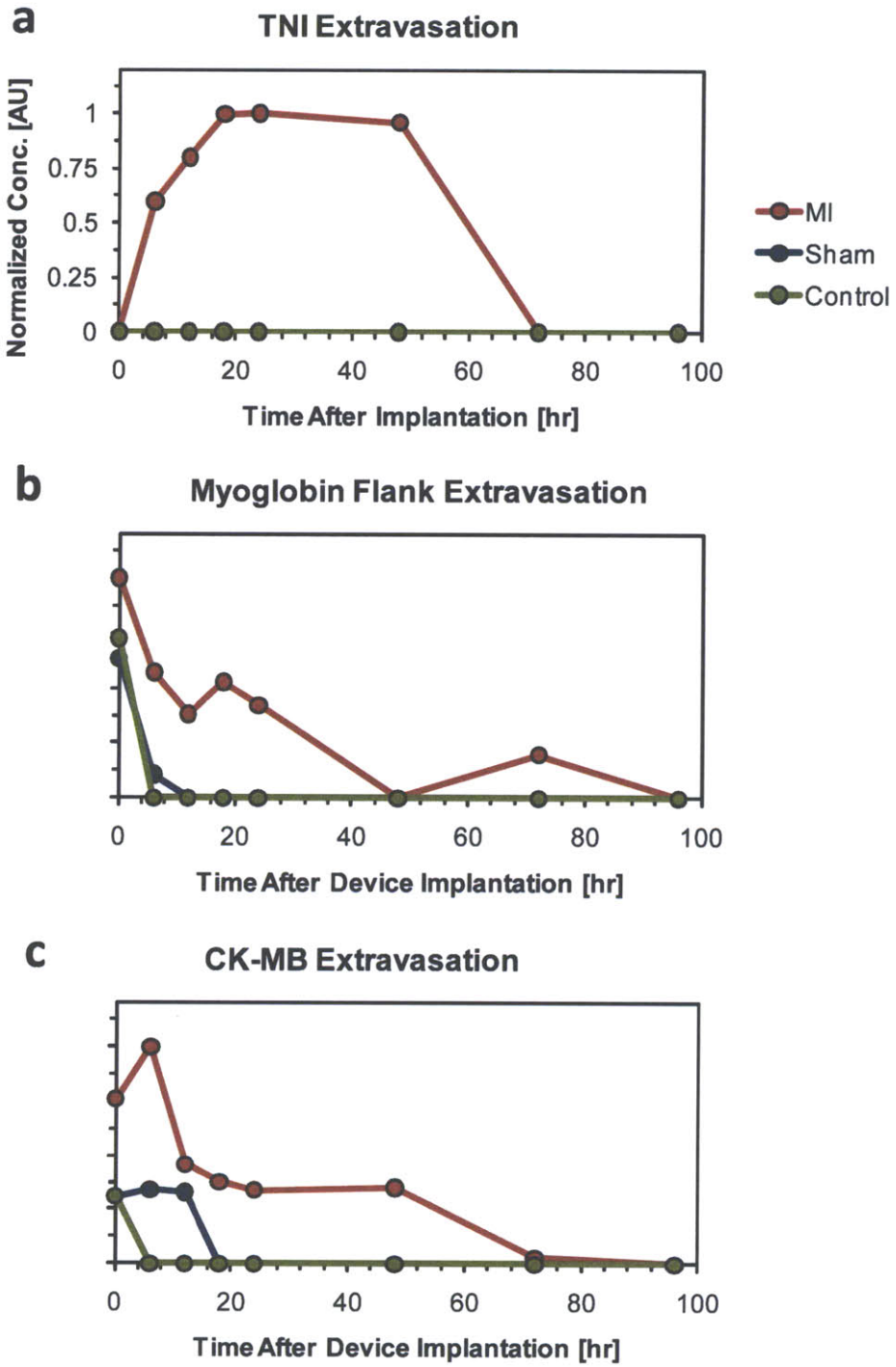

Figure 3.6 All biomarkers extravasate; MI groups are significantly elevated above corresponding Control and Sham groups. High initial levels of Myoglobin and CK-MB are presumably a consequence of implantation-induced injury. Measurements were made using ELISA and plotted as the mean of n=4 samples. Error bars are omitted to allow for uncluttered visualization.

The clearest and most important conclusion we draw from this data is that biomarker elevations in the MI group differ in both degree and intensity from the Sham and Control groups. It should therefore be possible to distinguish between the conditions based on measurements from implanted sensors. There are however some non-zero initial elevations in Myoglobin and CK-MB for the Control and Sham groups which we would expect to be reflected in sensor measurements. Open chest surgery and subcutaneous device implantation causes substantial non-cardiac injury. The early behaviors of these biomarkers are consistent with their differing specificities for cardiac injury; cardiac Troponin I is highly specific to cardiac damage, but CK-MB is less specific and Myoglobin is a marker of general muscle damage. Myoglobin and CK-MB are elevated in the extravasation Control groups so local implantation-induced trauma will likely visible to the implanted sensors. Furthermore, since no significant difference can be found between the Sham and Control groups for any biomarker, chest opening-induced trauma will be unlikely to further ambiguate any *in situ* sensor response.

The following point of experimental methodology bears discussion: in sampling flank extravasate, 1 mL PBS was flushed through the compartment to obtain measurable sample volumes. Dilution of the sample concentrations by some factor from the true subcutaneous levels was thus unavoidable. The reduced flank levels of TNI and CK-MB approached the lower limit of assay detection because the assays were designed to measure serum levels of biomarker. This data was judged, despite the inherent error, to correspond to absolute levels of biomarker (adjusted by some dilution factor) and so sufficient for verifying that cardiac biomarkers do extravasate to the flank at measurable levels. Note that a coarse comparison of maximum serum and flank TNI concentrations suggests a dilution factor on the order of 30x (≈10ng/ml in serum, ≈0.3 ng/ml in flank). Timing differences between the serum and flank measurements also indicates that all three cardiac biomarkers extravasate with a time-delay. This is unsurprising as the biomarkers must cross from circulation into the subcutaneous space.

Experimental Condition	Subcutaneous Sensor Implantation	Chest Opening Surgery	LAD Ligation Surgery
MI	X	X	X
Sham	X	X	
Control	X		

Table 3.3 Summary of procedures employed under each experimental condition.

3.4 *In Vitro* Validation

We functionalized MRSw nanoparticles with polyclonal antibodies against TNI, Myoglobin and CK-MB. The derivatization approach detailed in Chapter 2 was employed. Briefly, secondary antibodies sensitive for the Fc region of goat antibodies were chemically conjugated to the surface of 50 nm iron oxide nanoparticles. Subsets of nanoparticles were then derivatized from this original set by direct incubation with goat-derived primary antibodies. The *in vitro* response of these particles was characterized by combining nanoparticle solution with known concentrations of TNI, myoglobin and CK- MB analyte after derivatization. T_2 changes were determined by single sided proton NMR relaxometry from samples assayed in standard 8-well strips. The response of each derivatized MRSw subset is shown in Figure 3.7.

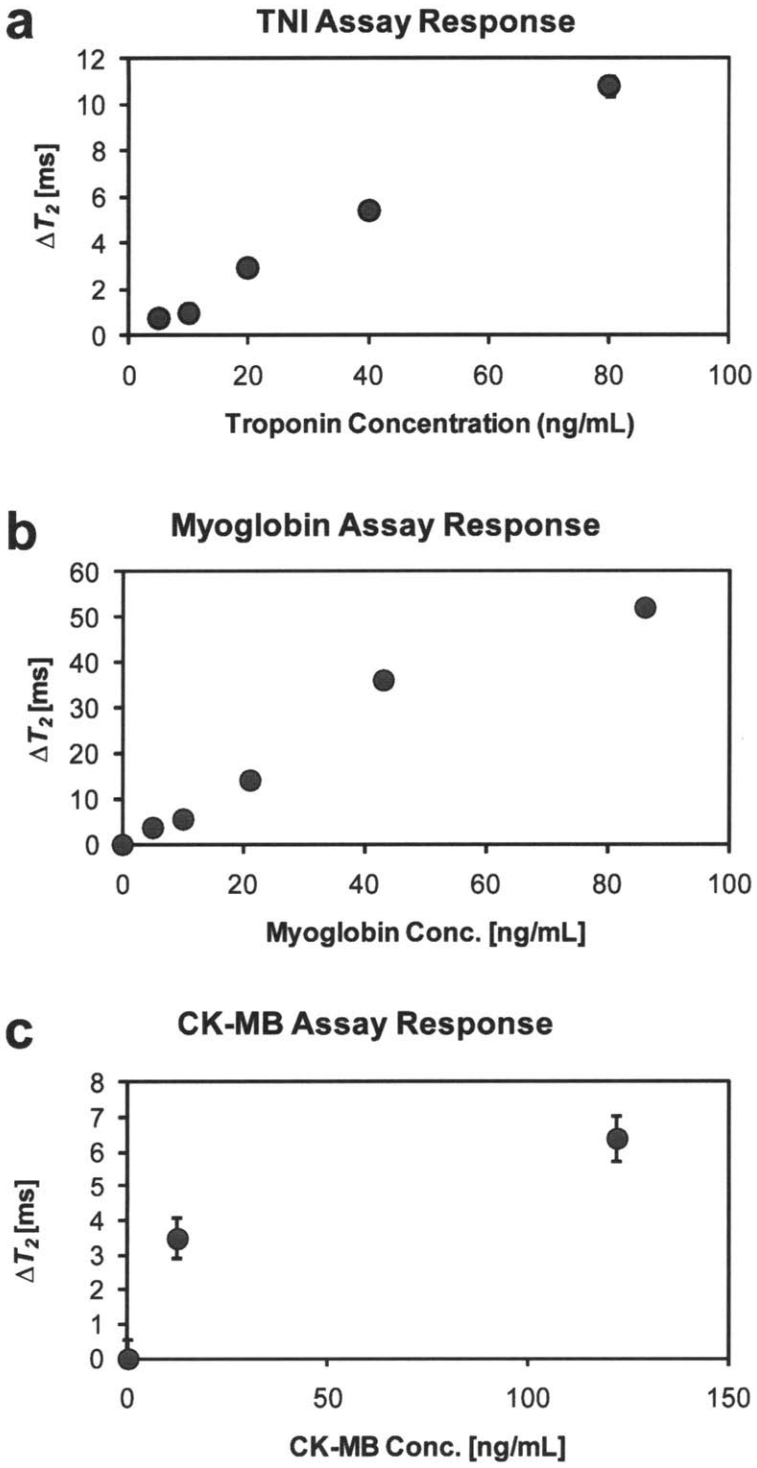

Figure 3.7 The concentration-dependent response of nanoparticles derivatized to target **a**, troponin I, **b**, myoglobin and, **c**, CK-MB. Error bars give the 95% confidence interval of the fit. T_2 values are graphed after a 24 hr incubation period as the difference from the control (0 ng/ml) sample.

3.5 Sensor Fabrication and Calibration

We next enclosed the functionalized magnetic nanoparticles within discrete diffusion sensors (Figure 3.8a) using a method adapted from Daniel *et al.* (5). We began by first affixing size-exclusion 30 nm pore polycarbonate membranes to one end of high density polyethylene cylinders (inner diameter = 4.0 mm, outer diameter = 7.8 mm, thickness = 1.7 mm) with double-sided adhesive. A hole was made in the adhesive prior to attachment to match the opening of the cylinder's inner diameter. This allowed the adhesive to mediate attachment without impeding cross-membrane transport. The internal sensor compartment was then filled with 25 μL MRSw solution, and closed on the opposing end with single-sided adhesive. The sensors were stored in PBS/BSA prior to use.

Sensors and assays usually possess a dynamic range across which measurements are valid and quantitative. Poor matching of dynamic range to measured quantity yields inaccurate results. We therefore attempted to match the sensors' dynamic range to the *in vivo* serum levels of TNI (10^1-10^2 ng/ml), Myoglobin (10^2-10^3 ng/ml) and CK-MB (10^1-10^2 ng/ml) after LAD ligation. TNI and CK-MB particle sets were adjusted by tuning the derivatization valency (described in Chapter 2) before incorporation within the sensor body. Myoglobin sensors were tuned in a different way; rather than adjusting particle chemistry we calibrated the sensors' transport characteristics. This was achieved by reducing the size of the double-sided adhesive's opening (Figure 3.8b) from to 1.7 mm from 0.1 mm, thereby effectively reducing the surface area (which is directly proportional to the flux) by a factor of ≈300. The responses of normal (control) and calibrated (reduced surface area) myoglobin sensors are plotted in Figure 3.8c. We determined this increased dynamic range to be in adequate alignment with the *in vivo* levels of analyte that the sensors were expected to encounter. Varying membrane composition and pore size are alternative methods we could have explored to slow transport but modulation of the exchange surface area was straightforward. The *in vitro* response of the sensors, after calibration, is shown in Figure 3.9.

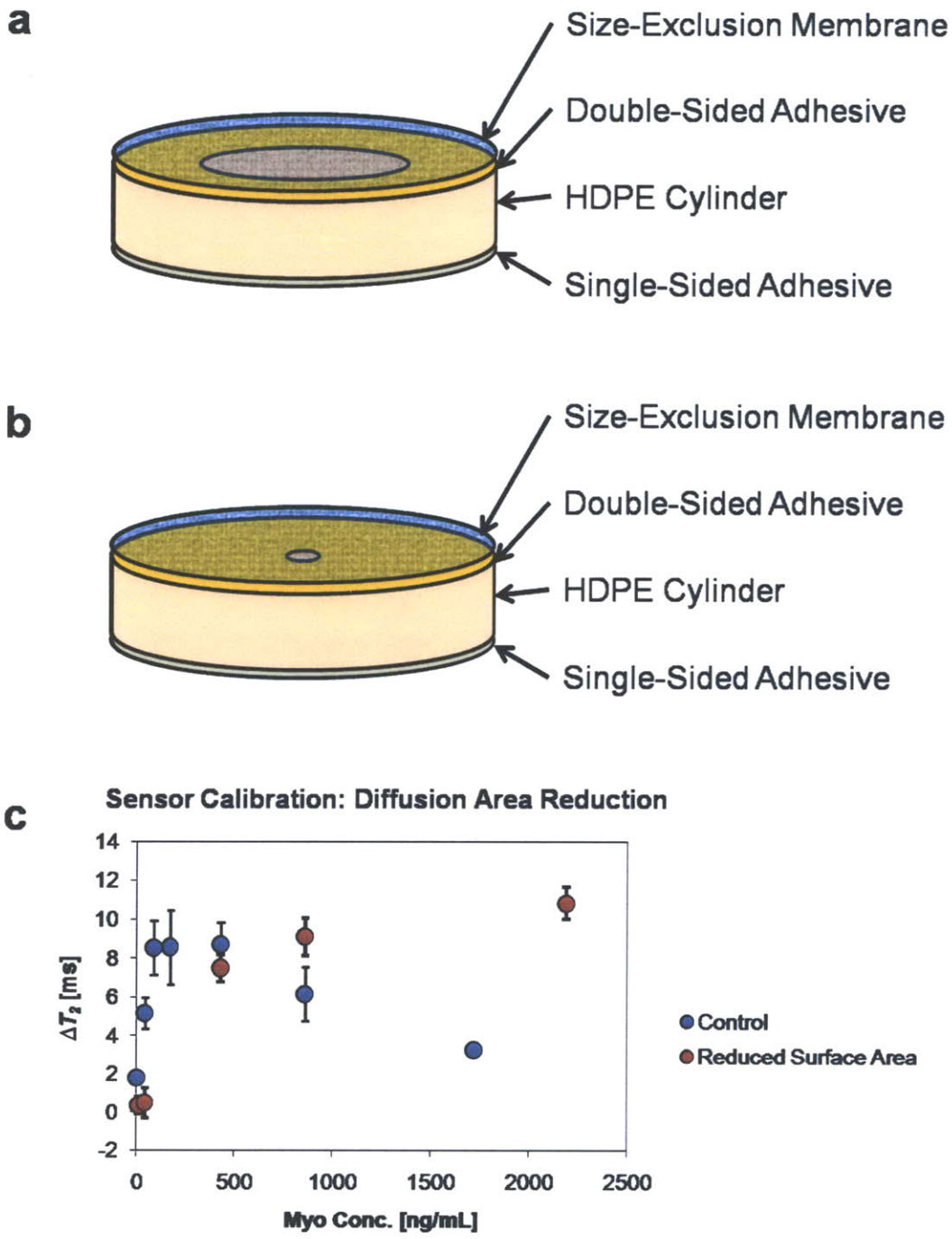

Figure 3.8 Sensor response can be tuned by varying the surface area available for mass transfer. **a**, A large surface area permits more rapid diffusion than, **b**, a smaller surface area. **c**, The sensitivity range of sensors (using Myoglobin as the model analyte) can therefore be shifted by reducing the surface area. Error bars give the 95% confidence interval of the fit error.

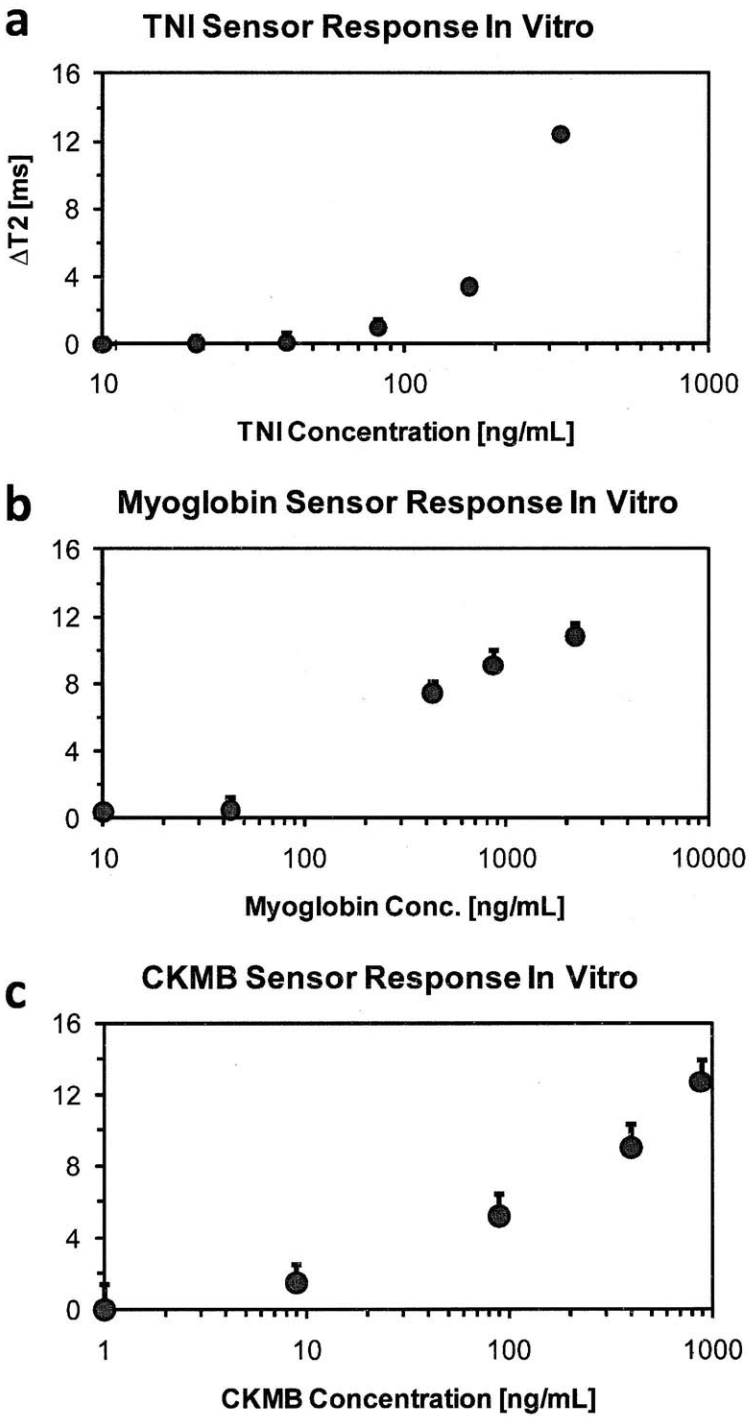

Figure 3.9 Derivatized MRSw particles were encapsulated within discrete sensors and calibrated *in vitro*. Concentration-dependent changes in sensor T_2 (above baseline) were determined after 72 incubation for TNI and 24 hr incubation for Myoglobin and CK-MB. The data is plotted as the mean of n=4 samples. Error bars represent standard errors.

3.6 Dosimetry Characterization

Antibody-antigen binding is the second strongest non-covalent interaction. We tested the proposition that antibody-based MRSw sensors would thus be irreversible and the degree of T_2 change a reflection of cumulative analyte exposure. Myoglobin sensor response to different temporal exposures possessing a common total dose of 516 ng/mL over a 12 hr duration confirms this property (Figure 3.10); the readings are roughly identical in each case. Real-time concentrations can be determined from these sensors by assessing T_2 differentials over time. The capacity to integrate analyte levels over an extended duration could be extremely useful in applications for which a low analyte level may be difficult to detect or quantify at a given instance. We acknowledge that this behavior may be a downside in certain applications as antibody functionalized MRSw are limited to fixed lifetimes reached upon saturation of all binding sites. However, he time frame for these *in vitro* studies is well-matched to the *in vivo* scope of the present work.

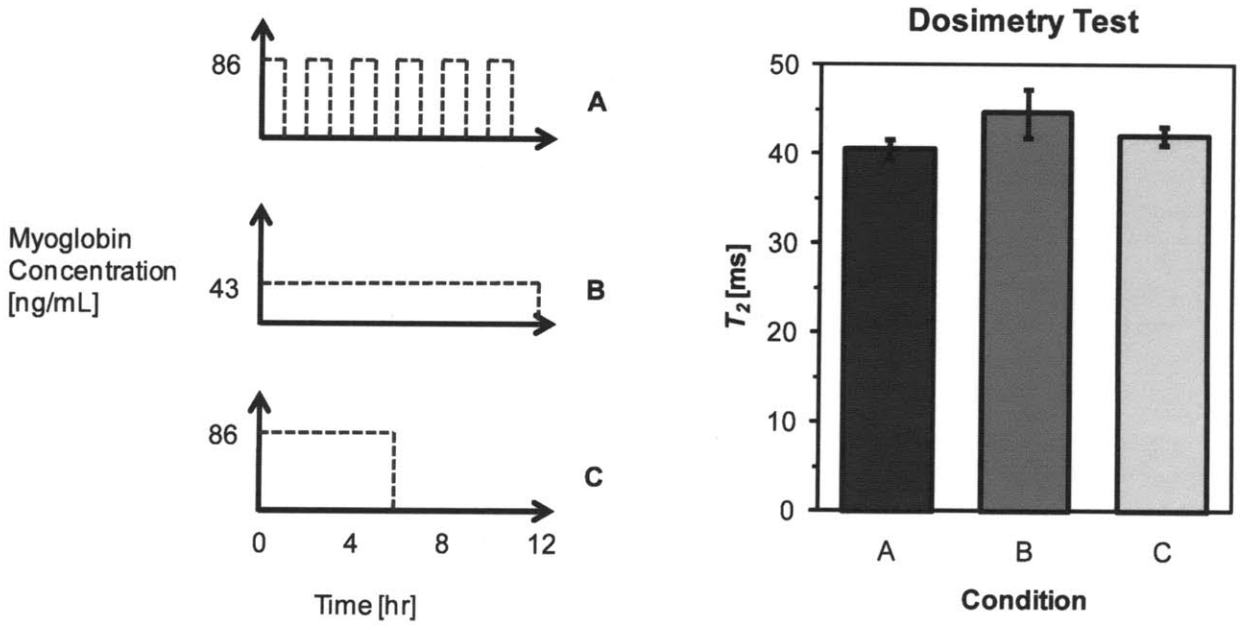

Figure 3.10 Sensor response corresponds to cumulative analyte exposure, as demonstrated here for Myoglobin (and confirmed for TNI and CK-MB); T_2 remains the same regardless of exposure profile. The data is plotted as the mean of n=4 samples. Error bars represent standard errors

3.7 *In Vivo* Measurements

We proceeded to implant sensors specific for each biomarker in the subcutaneous flank of animals belonging to the MI, Sham, and Control groups described above (Table 3.3). *In situ* MRI-based measurements demonstrate that the sensors can be interrogated while implanted (Figure 3.11a). The majority of measurements were taken from explanted sensors read using a single-sided relaxometer. Significant T_2 increases of the MI over the Sham/Control groups for all three biomarkers are evident (Figure 3.11b) despite the limited sensitivity of the single-sided system (discussed in the Materials

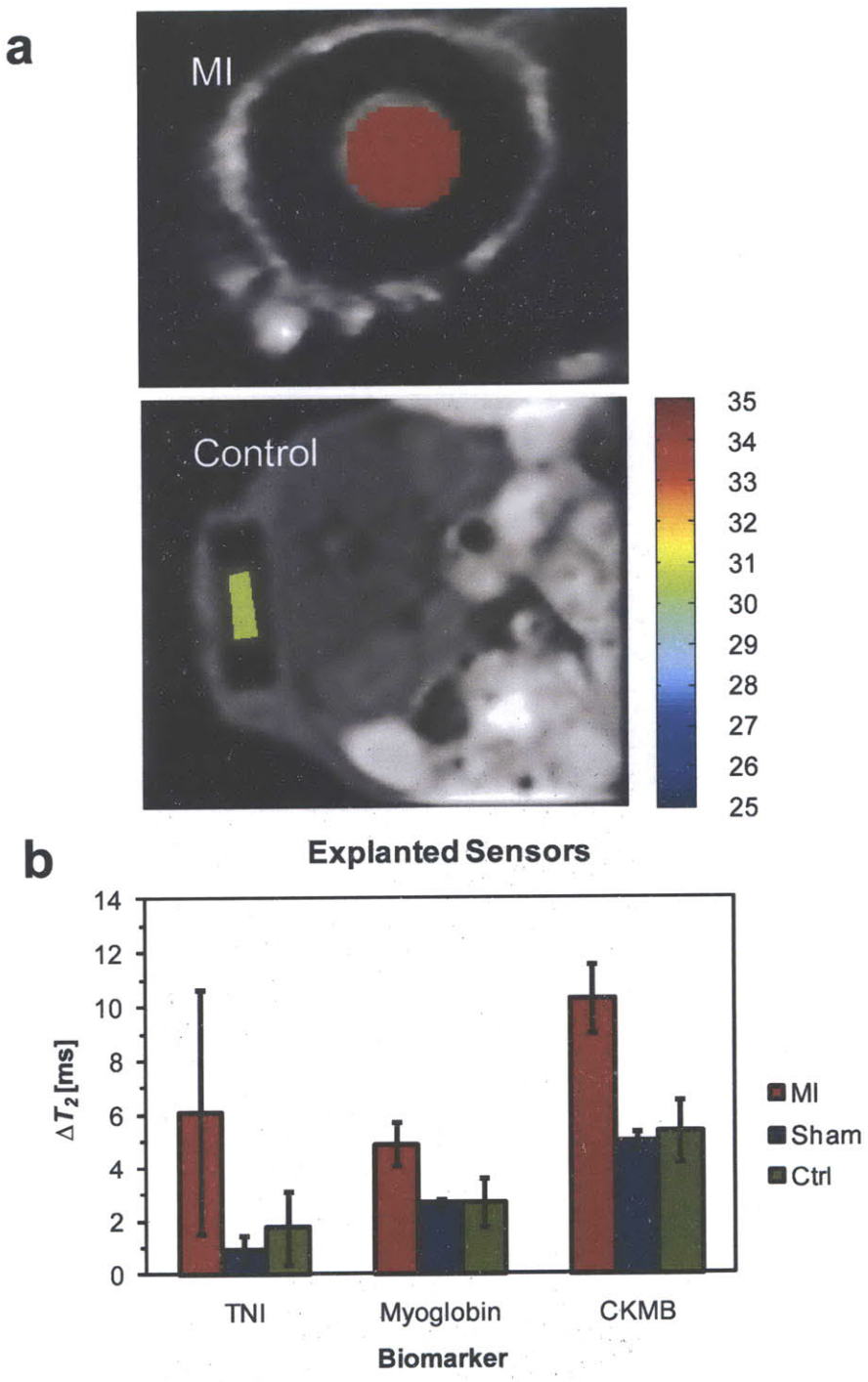

Figure 3.11 The magnitude of sensor response differs between experimental and control groups. **a**, A T_2 map (color bar on the right) super-imposed on T_2-weighted images of Myoglobin sensors demonstrates the feasibility of MRI-based *in situ* measurements. **b**, The T_2's of sensors explanted from the MI group are significantly higher than from the Control and Sham groups; sensors were explanted and measured by single-sided proton relaxometry (after 72 hr implantation for TNI and 24 hr for myoglobin and CK-MB). The data is plotted as the mean across n=6 animals and error bars denote the standard deviation within the groups.

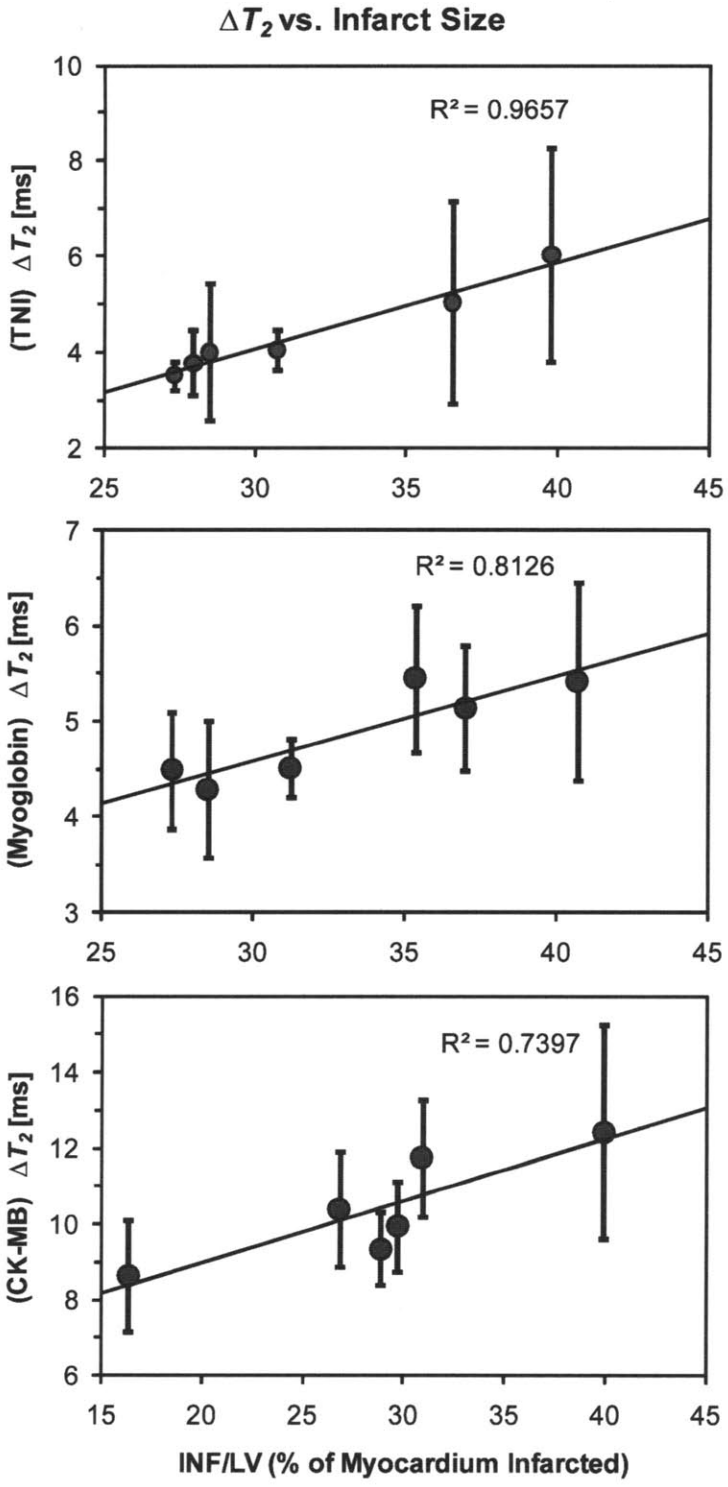

Figure 3.12: T_2 change consistently trends up with increasing infarction size. The error bars correspond to 95% confidence intervals about the mean response of n=6 sensors.

and Methods section). The elevations of Myoglobin and CK-MB in the Sham and Control groups are picked up (as expected) by but do not 'saturate' the sensors. Elevated T_2's for the Myoglobin and CK-MB sensors in the Sham/Control groups likely result from the implantation surgery. Antibody cross-reactivity with similar proteins may also play a role (the CK-MB antibody used here binds to the M subunit and so might also bind to CK-MM, a skeletal muscle variant of creatine kinase).

The infarction zone can be visualized through histology methods and objectively quantified as a fraction of total myocardium. We reasoned that since cardiac biomarkers are functional proteins directly discharged from infarcted tissue, their cumulative release should correspond to the magnitude of infarction. A direct comparison of sensor readings with infarct size (Figure 3.12) shows, despite the relatively large error bars, a consistent trend for all three biomarkers. Clinical cardiac panels are taken at single time points; the concept of cumulative sensing is a significant departure from traditional types of measurements.

3.8 Cardiotoxicity Studies

We studied one further application of these sensors, involving the determination of drug cardiotoxicity. Doxorubicin is a potent anthracycline antibiotic that has found wide clinical use as a cancer chemotherapauetic. Its cardiotoxic effects are well-known; after administration, patients exhibit dose-dependent loss of cardiac myocytes accompanied by serum cardiac biomarker elevation (12). We confirmed serum Myoglobin levels to markedly increase after administration in a murine model, though at an order of magnitude lower concentration than after acute MI (10^2 ng/ml vs. 10^3 ng/ml). Myoglobin sensors were thus left *in vivo* for 72 hr after implantation (as opposed to 24 hr for acute MI). The results show a clear distinction in sensor relaxivity between the Experimental and Control groups and validate sensor efficacy in assaying drug cardiotoxicity. We propose that these sensors can be used in the future to establish the cardiac side effects of novel pharmaceuticals.

3.9 Conclusions

Single time point measurements fit comfortably into the traditional clinical paradigm because they are easy to interpret and practical to obtain. Substantial further investigation will be required before the clinical relevance (or irrelevance) of 'cumulative' biomarker measurements can be established. Such data will in all likelihood prove to possess greater clinical value for some but not all applications. The MRSw molecular sensors described here represent a possible path in that direction. We have shown them to perform adequately in the detection of pathological elevations of disease biomarkers which are soluble, somewhat specific, and extravasate from circulation to the implant site. We aim in the future to explore the utilization of these cardiac sensors as a disease sentinel for groups at high risk for recurrent MI.

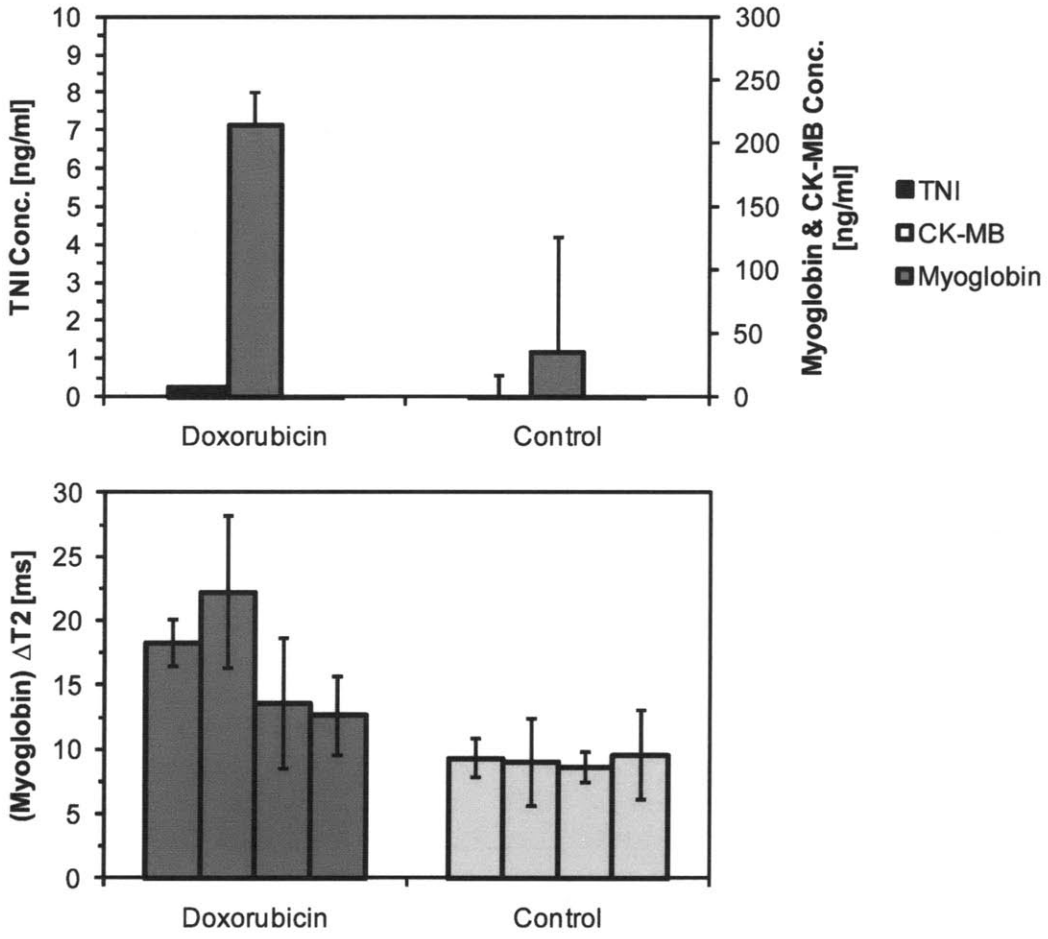

Figure 3.13: The cardiotoxic effect of doxorubicin can be detected *in vivo*. **a**, Doxorubicin induces a marked upswing in serum Myoglobin but has minimal impact on TNI and CK-MB (ELISA measurements). Data bars indicate the average and error bars the standard deviation across n=4 animals per condition. **b**, Myoglobin sensors explanted from a doxorubicin-administered group show significant increases in T_2 over those from a control group. Data bars indicate the average and error bars their corresponding 95% confidence intervals across n=4 sensors per animal.

3.10 Materials and Methods

3.10.1 Preparation of magnetic nanosensors

NanoMag-CLD magnetic iron oxide nanoparticles with amine terminated dextran shells (Micromod, Rostock, Germany) were coupled with monoclonal antibody against goat IgG (Meridian Life Sciences, Sac, ME) using a previously described method(13). These particles were derivatized against specific targets by incubation with goat-produced polyclonal antibodies against myoglobin (BiosPacific, Emeryville, CA) and CKMB (BiosPacific, Emeryville, CA). Unless otherwise specified, nanoparticles were suspended in PBS (Gibco) with 1% bovine serum albumin (Sigma) and 0.1% Penicillin-Streptomycin (Gibco) to minimize bacterial contamination and non-specific adsorption.

3.10.2 Device fabrication and implantation

Derivatized MRSw were encapsulated within small diffusion devices(4). Polycarbonate diffusion membranes (SPI Supplies, West Chester, PA) were affixed by double-sided adhesive to one side of high density polyethylene cylinders. The opposite end of the cylinders was closed off by single-sided adhesive (3M) after the device was filled with 25 μl MRSw solution. Devices (n = 6 per animal) were implanted subcutaneously in flank of animals.

3.10.3 Myocardial infarction surgery

We used 9-10 week old C57BL6 mice. Mouse LAD ligation has been previously described (9). Briefly, an intercostal approach between the 3rd and 4th intercostals spaces was taken to expose the pericardium. Upon opening the pericardium and identifying the LAD under stereo microscopy, a silk ligature was passed underneath and tied around the vessel to induce occlusion. Occlusion was confirmed by observed blanching of the anterior left ventricular wall. The chest cavity was then carefully closed layer by layer. Sham-operated mice underwent the same procedure without tying the LAD ligation suture.

3.10.4 Independent measurements of biomarker levels

Independent measurements of biomarker levels. Enzyme-linked immunoassays (ELISA) were used to independently quantify myoglobin (Life Diagnostics, West Chester, PA), CK-MB (Oxis International, Foster City, CA), and Troponin I (Life Diagnostics, West Chester, PA) levels. Serum samples were taken from the tail vein. Lavage samples were obtained by flushing the flank with 1ml PBS.

3.10.5 Infarct Size Determination

Area at risk and area of infarction were determined by perfusing Evans blue dye into the carotid artery prior to sacrificing the animal. Hearts were then removed and sectioned perpendicular to the long axis into 1 mm slices using a McIlwain tissue chopper (Sterling, Wood Dale, IL) and stained with 1% triphenyltetrazolium chloride (TTC) for 5 min at 37°C. Each slice was analyzed for left ventricular area, area at risk and infarct size.

3.10.6 Doxorubicin Administration

20 mg/kg doxorubicin was administered by intraperitoneal injection 72 hr prior to serum ELISA measurement and device implantation. Myoglobin devices were left *in vivo* for 72 hr prior to MR interrogation.

3.10.7 Measurement of proton relaxation times

Proton relaxation measurements were determined on a custom-built system using a single-sided NMR sensor (0.43T and 25°C; Profile NMR MOUSE, ACT Center for Technology, Aachen, Germany). The sensor's field gradient enables measurements to be made on a single device positioned above the sensor. Transverse relaxation times for the single-sided MR ($T_{2,eff}$) were measured using a Carr Purcell Meiboom Gill (CPMG) sequence with the following parameters: echo time (TE) = 0.035 ms, 5714 echoes, 16 scans, and recovery time (TR) = 3 s. The echo peak intensities were fit to the equation $I = I_0 e^{-t/T2}$ using a custom script running on MATLAB (The Mathworks, Natick, MA).

3.10.8 Magnetic resonance imaging

MRI measurements were made on a 9.4T animal imager (Bruker Biospin). Animals were anesthetized during imaging with 1-1.5% inhaled isoflurane, and monitored during imaging with respiration monitoring. Imaging protocols included a Tri-plane and axial RARE localizer. Multi-slice multiecho (MSME) T_2-weighted imaging was performed using the following parameters: flip angle = 90°; Matrix size (128 x 184); TR = 2330 ms; TE = 16 equally spaced echoes at 8.8 ms intervals ranging from 8.8 ms to 141 ms; field of view (FOV) = 4 cm x 4 cm, slice thickness = 1 mm. T_1-weighted imaging was performed using the following parameters: flip angle = 90°; matrix size (192 x 256); TR = 700 ms; TE = 14 ms; field of view (FOV) = 4 cm x 4 cm, slice thickness = 1mm. Region of interest analysis was performed and T_2 fit was performed using a mono-exponential fitting algorithm for the multi-TE data (Osirix). ROI incorporating the center 2-3 slices of the devices were analyzed. The fitting of the T_2 was modified by subtracting the mean background noise, and onlyu points above this mean baseline threshold were used for the fit.

3.11 Appendix

3.11.1 MRI-Based Measurements

Daniel *et al.* previously demonstrated that MRI-based T_2 measurements could be made on discrete implanted sensors possessing MRSw contrast agents (4). The form factor of their sensors were, however, much larger than the one we use in this work. We could not assume, given the resolution limitations of MRI, that the transverse relaxivities of these far smaller sensors could be reliably measured by imaging. Figure 3.14 shows a series of T_2-weighted images of a closed sensor (i.e. possessing no size-exclusion membrane and contained on both sides by single-sided adhesive) containing a suspension of magnetic nanoparticles. The sensors can clearly be imaged *in situ*. Sensor T_2 was determined from these images by fitting mean signal intensity within the sensor area to the equation $I = I_0 e^{-t/T2}$.

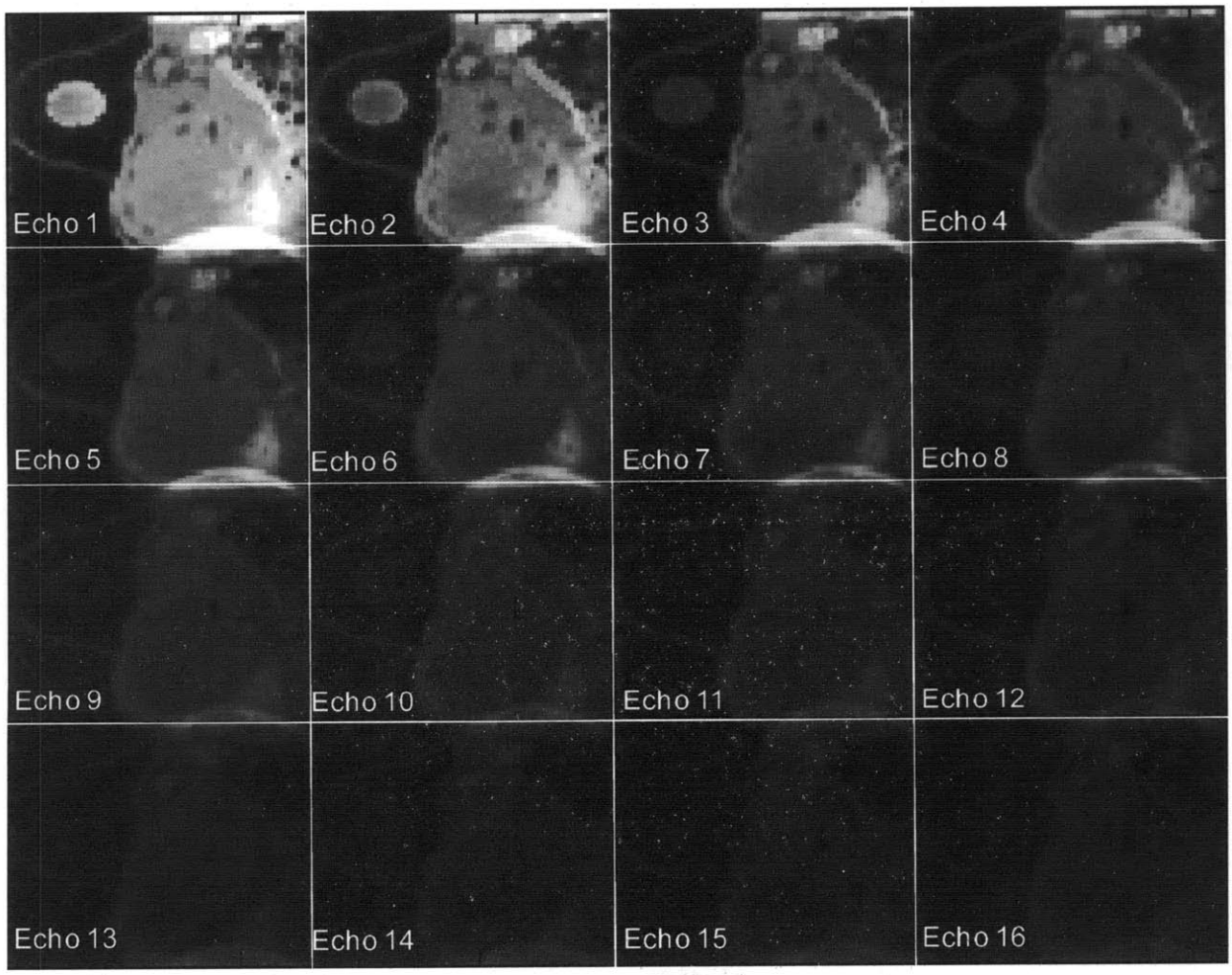

Figure 3.14: A sequence of T_2-weighted images acquired at 16 linearly increasing echo times. T_2 is measured by quantifying signal decay within the sensor area.

The reliability of these MRI-based measurements was probed by comparing the relaxivities of, 1) the sensors as measured from axial and sagittal slices, and 2) implanted and non-implanted sensors. Stacks of 4 closed sensors possessing 100 μg/mL, 50 μg/mL, 25 μg/mL, and 12.5 μg/mL (Fe concentration) of magnetic nanoparticle were fabricated. The transverse relaxivities of sensors from two stacks (Figure 3.15), implanted and non-implanted, were acquired (Figure 3.16). Measurements made from axial and sagittal slices appear to differ by no more than 3 ms. Correspondence between implanted and non-implanted sensors also falls within roughly 3 ms, with the exception of an outlier at 12.5 μg/mL condition.

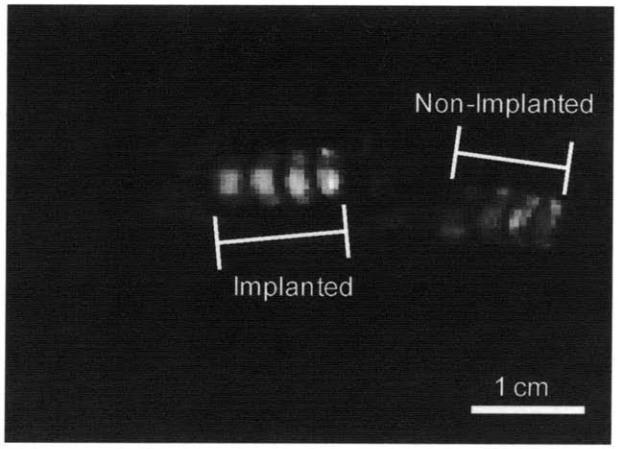

Figure 3.15: A T_1-weighted image of two stacks of sensors. One stack is implanted while the other stack is not.

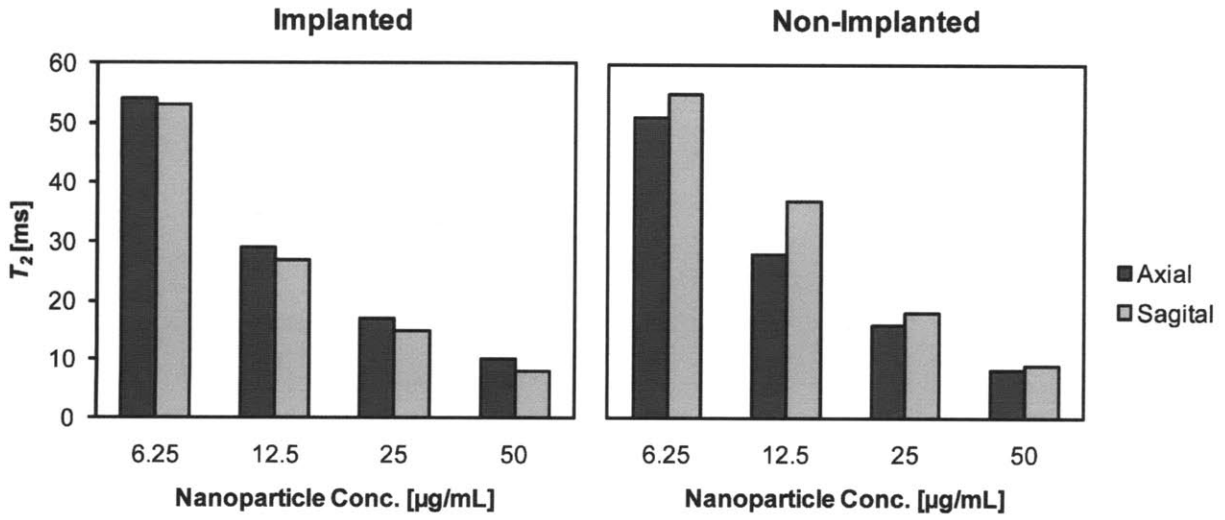

Figure 3.16: MRI-based T_2 measurements acquired from closed sensors, either implanted (left) or non-implanted (right), possessing differing nanoparticle concentrations. Error bars are omitted but 95% confidence intervals for the fit are <1 ms in all cases.

3.12 References

1. Lilly LS (1998) *Pathophysiology of Heart Disease* (Lippincott Williams and Wilkins) p 401.
2. Sheifer SE, Manolio TA, & Gersh BJ (2001) Unrecognized myocardial infarction. *Ann Intern Med* 135(9):801-811 .
3. Alpert JS, Thygesen K, Antman E, & Bassand JP (2000) Myocardial infarction redefined--a consensus document of The Joint European Society of Cardiology/American College of Cardiology Committee for the redefinition of myocardial infarction. *J Am Coll Cardiol* 36(3):959-969 .
4. Daniel KD, *et al.* (2009) Implantable diagnostic device for cancer monitoring. *Biosens Bioelectron* 24(11):3252-3257 .
5. Badgwell D & Bast RC, Jr. (2007) Early detection of ovarian cancer. *Dis Markers* 23(5-6):397-410 .
6. Duffy MJ (2001) *Critical Reviews in Clinical Laboratory Sciences* 38:225-262.
7. Grossman MH, R.; Gocze, P.M.; Ott, M.; Berger, P.; Mann, K.; (1995) *European Journal of Clinical Investigation* 25:867-873.
8. Wu AH, *et al.* (1999) National Academy of Clinical Biochemistry Standards of Laboratory Practice: recommendations for the use of cardiac markers in coronary artery diseases. *Clin Chem* 45(7):1104-1121 .
9. Michael LH, *et al.* (1995) Myocardial ischemia and reperfusion: A murine model. *Am J Physiol-Heart C* 38(6):H2147-H2154 .
10. Alpert JS, *et al.* (2000) Myocardial infarction redefined - A consensus document of the Joint European Society of Cardiology/American College of Cardiology Committee for the Redefinition of Myocardial Infarction. *Eur Heart J* 21(18):1502-1513 .
11. Wu AHB, *et al.* (1999) National Academy of Clinical Biochemistry standards of laboratory practice: Recommendations for the use of cardiac markers in coronary artery diseases. *Clin Chem* 45(7):1104-1121 .
12. Wallace KB, *et al.* (2004) Serum troponins as biomarkers of drug-induced cardiac toxicity. *Toxicol Pathol* 32(1):106-121 .
13. Wunderbaldinger P, Josephson L, & Weissleder R (2002) Crosslinked iron oxides (CLIO): a new platform for the development of targeted MR contrast agents. *Acad Radiol* 9 Suppl 2:S304-306 .

Chapter 4

MR Readable Calcium Sensor

Past strategies for MR based sensing relied upon analyte-mediated changes to the aggregation state of functionalized magnetic nanoparticles. We describe here a method for calcium detection which does not depend on this phenomenon but rather on polymerization driven changes in the MR contrast of alginate hydrogels. Sensitivity and robustness in the presence of potentially interfering ions are determined.

4.1 Motivation

It has not been previously recognized that alternatives to nanoparticle aggregation exist for generating analyte specific contrast in MR readable sensors. Our primary motivation in this chapter was thus to provide the first demonstration of a MR readable sensor incorporating a wholly different mechanism. Calcium was chosen as the target for its importance in biological processes such as signal transduction (1, 2). Calcium dysregulation has also been implemented in pathologies ranging from neuropathic disorders (3, 4) to cancer (5) to osteoarthritis (6), making it an attractive marker for physiological monitoring.

Two groups have previously developed nanoparticle-based MR readable calcium sensors. The Jasanoff group exploited the calcium-dependent interaction of calmodulin with M13 peptide sequence (7, 8). They showed that nanoparticles conjugated to calmodulin would couple, in the presence of calcium, to nanoparticles conjugated to M13. The Josephson group subsequently produced calcium sensitive particles based on traditional electrode chemistry (9). Their work departed from Jasanoff's in that it used Chel (a derivative of diglycolic anhydride) as the calcium-binding moiety. The specific identity of the binding moieties aside, both groups relied on the same underlying nanoparticle aggregation mechanism to generate T_2 contrast. Calcium concentration-dependent T_2 changes were found to be tune-able in both cases. Sensor reversibility was also somewhat limited in both cases; de-aggregation could only be achieved through the addition of calcium chelating agent EDTA. Perhaps neither assay was capable of de-clustering with the simple removal of calcium because of the strength of attachment between calcium and the binding moieties used.

4.2 Alginate Polymerization

Hydrogels are liquid-swollen hydrophilic polymers commonly found in commercial (contact lenses) and research (tissue engineering (10, 11), drug deliver (12, 13)) applications. They are, like most other polymers, composed of chemical chain repeats tethered together by cross-linking agents. Addition of crosslinker to liquid pre-gel induces onset of gelation and transformation into a solid.

NMR spectroscopy has been employed in the past to study the chemistry and underlying structure of this important class of materials (14-16). It is known as a consequence of these studies that the relaxivities of water in liquid pre-gel and solid hydrogel dramatically differ. We exploit this behavior to create a cross-linker sensitive MR readable sensor. Calcium/alginate is the model crosslinker/hydrogel pair used.

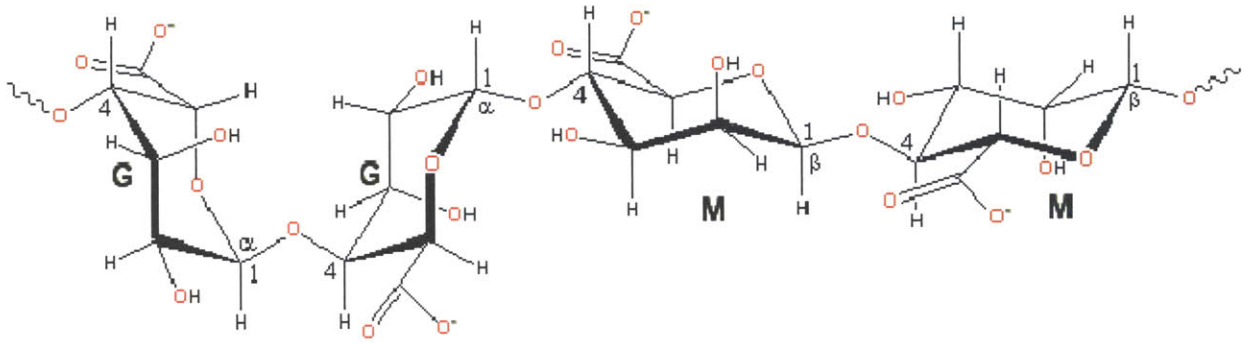

Figure 4.1: Alginate chains are linear sequences of D-mannuronic (M) and L-guluronic (G) acids. Divalent cations complex with reactive carboxyl groups to link adjacent strands and enable network formation.

Alginate is a linear unbranched polymer derived from brown algae which has been employed in cell encapsulation (17-20), drug delivery (21, 22) and wound dressing (23-25) applications. The polysaccharide strands (Figure 4.1) comprised of D-mannuronic and L-guluronic acid sequences are water soluble and may be cross-linked by calcium or other divalent cations (26). Crosslinkers are thought to function by binding the carboxylic acid sites of adjacent strands. Addition of $CaCl_2$ to alginate pre-polymer solution yields rapid formation into solid hydrogel.

4.3 Chemical Exchange T_2 Contrast Mechanism

Our primary concern is experimental but this section will provide a brief discussion of the underlying T_2 contrast mechanism. *All* protons within a sample are excited in proton NMR. Measurements of pure H_2O produce a clean water signal but measurements of biological tissues are more complex, reflecting a combination of the water protons along with those attached to carbohydrates, lipids, and proteins. We are concerned with the relaxivity of alginate, which as a hydrogel is composed of mostly water (95%) in its pre-gel and gelled states. A hydrogel's MR signal is complex but water should dominate in proportion to its abundance in this material.

The MR response of a system comprised of non-interacting components x and y is the sum of the two: $S_{total}(t) = S_x(t) + S_y(t)$. Signal decay is best described in this situation by a bi-exponential. The combination, in practice, of a sufficiently brief MR signal with a relatively long one obfuscates the shorter signal. The extremely rapid decay of many polymer-associated protons (on the order of 100 μs as opposed to seconds for free water) therefore makes them invisible in the aggregate signal of a hydrogel. If, however, the polymer protons chemically exchange with the surrounding water, then the short T_2 of these protons (as in the case of hydroxyl groups on alginate) will bleed into the measured single-exponential T_2 (27). A mathematical description of relaxivity in systems undergoing chemical exchange was first developed in the 1960's by Swift and Connick (28) and has subsequently been modified to describe hydrogels (29, 30). We adopt a version of this model to describe hydrogel transverse relaxation as a function of cross-linking density. The idea is to treat the system as

composed of two proton pools (free water, polymer) coupled by chemical exchange. The observed/measured T_2 is described by:

$$\frac{1}{T_2} = \frac{1-p}{T_{2fw}} + \frac{p}{T_{2\,polymer} + \tau_{ex}}$$

where T_2 is the observed relaxivity, T_{2fw} is the relaxivity of free water protons, $T_{2polymer}$ is the relaxivity of alginate-associated protons, τ_{ex} is the characteristic lifetime of hydrogel-associated protons, and p is the fraction of protons in the hydrogel pool. This model assumes that: 1) p is very small, 2) the characteristic lifetime of free water protons is much longer than τ_{ex}, and 3) $T_{2polymer} << T_{2fw}$. Kennan *et al.* noted that cross-linking density should not impact T_{2fw}, $T_{2polymer}$, or p (31); however, they empirically determined τ_{ex} to decrease with increased cross-linking. The polymer is, in other words, analogous to a transverse relaxation sink which can cycle more rapidly through free water protons as it becomes more cross-linked. We therefore expect to find T_2 decreases as a function of increasing polymerization.

4.4 Sensor Performance

4.4.1 Dynamics and Sensitivity

The sensors are fabricated as alginate (5% w/v) pre-gel enclosed within Slide-a-Lyzer MINI Dialysis Units (Pierce). Their membranes function as a size-selective diffusion barrier, facilitating the entry of small molecules while preventing the outward escape of alginate. Measurements were made after incubating the sensors in calcium chloride baths of controlled concentrations. We refer for simplicity to the duration between placement of sensors within sample baths and T_2 measurement as the 'equilibration time.'

A representative T_2 time course of alginate sensors incubated in calcium solutions of defined concentrations is plotted in Figure 4.2. The T_2 of the control sample (0 mM) remained unchanged while the T_2 of the two experimental samples (100 mM and 500 mM) decreased. The results from the two experimental conditions differ by the rate at which their respective T_2 values reached a baseline of ~40 ms. This baseline T_2 towards which the sensors equilibrated was the same for all calcium concentrations tested (as low as 10 mM). Alginate might therefore be considered to act as a sink for calcium, achieving full polymerization upon binding a sufficient number of calcium ions. A T_2 value of ~40 ms must then correspond to a fully polymerized slab of calcium alginate. Note, however, that the speed of polymerization does increase for higher concentrations of calcium; from Fick's law we know that the rate of diffusion across a membrane increases with the gradient across it. Differences in calcium diffusion must therefore drive differences in the rate at which T_2 converges towards ~40 ms. Adjustment of the equilibration time is a straightforward means of tuning the dynamic range. The sensor does not provide an instant response, but the necessary equilibration times are relatively short in comparison to those required by nanoparticle-based assays.

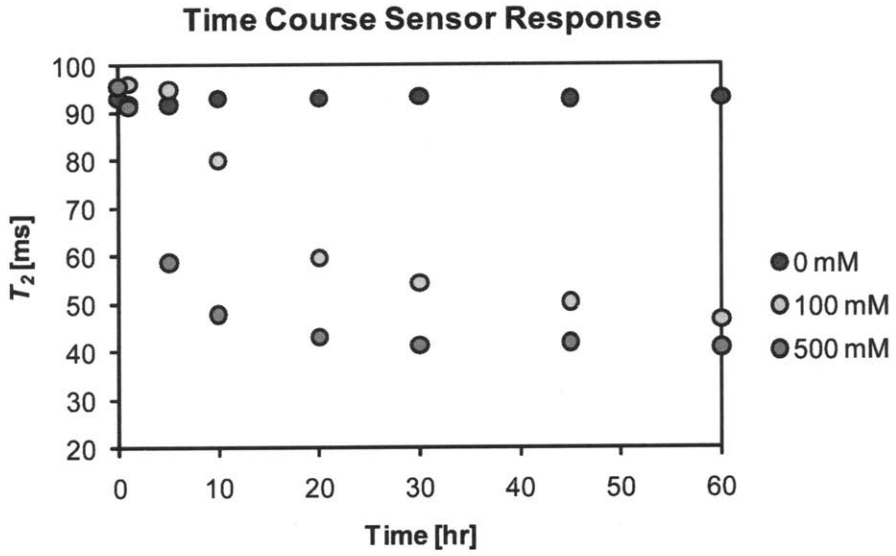

Figure 4.2. A representative T_2 time course of alginate sensors placed within $CaCl_2$ baths of 0 mM, 100 mM, and 500 mM. Error bars are omitted to facilitate uncluttered visualization.

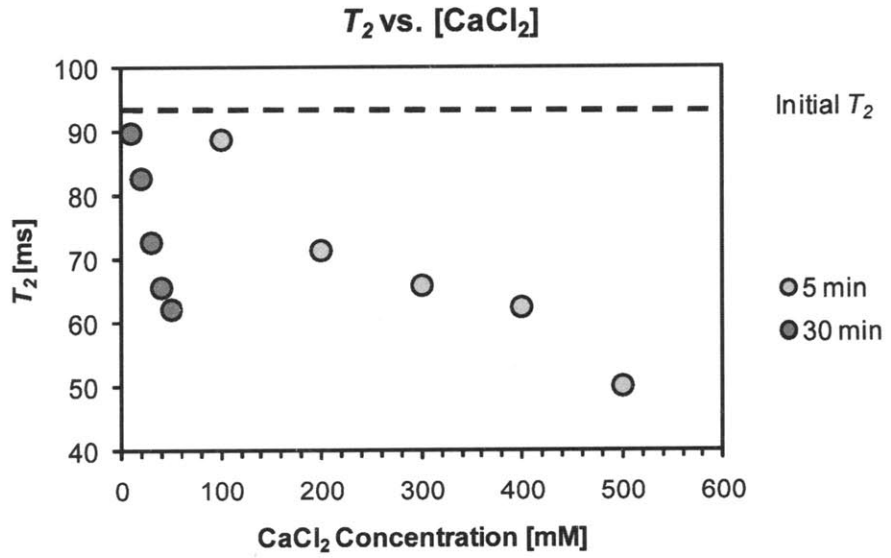

Figure 4.3. The T_2 of alginate sensors as a function of $CaCl_2$ concentration (n=3). The dotted line indicates the initial sensor T_2; light and dark data points correspond to the T_2. It is the rate of T_2 change which corresponds to calcium concentration so the dynamic range of alginate sensors can be tuned by varying the equilibration time. The T_2 of sensors placed within higher calcium concentrations can thus be measured at a shorter equilibration time (5 minutes) while the T_2 of sensors placed within lower calcium concentrations can be measured at a longer equilibration time (30 minutes) (Figure 4.3). of sensors after 5 minutes and 30 minutes, respectively, of exposure in $CaCl_2$ baths. Error bars are omitted to facilitate uncluttered visualization.

4.4.2 Robustness and Reversibility

The specificity of these alginate-based sensors in the presence of potentially interfering non-calcium ions was next explored (Figure 4.4). Our findings show the sensor to be robust in PBS as well as in the presence of Mg^{2+}, K^{+}, and NH_4^{+}. Calcium-induced T_2 change in samples containing Li^{+} appears somewhat affected although this effect could be accounted for during measurement by calibration against appropriate standards. Importantly, the sensors do not respond to these ions under the control condition (0 mM $CaCl_2$). This result compares favorably against that of the Josephson group's Chel-decorated nanoparticles which exhibit a partial response to Mg^{2+}. Other divalent cations known to induce alginate polymerization would however be expected to trigger changes in relaxivity.

Reversibility was assessed by incubating previously calcium-exposed sensors in calcium-deficient buffers. The low T_2 of these gelled sensors did not appreciably increase over a 24 hr measurement window. It is possible that constant refreshing of the calcium-deficient buffer could facilitate reversibility over a longer time scale. Such a procedure would, however, be of limited practical significance for real-time *in vivo* monitoring applications. The calcium chelator EDTA, when loaded into the calcium-deficient buffer, did induce the sensors to reverse in a general sense (Figure 4.5). While this means of achieving reversibility is not adequate for *in vivo* use, it is on par with the responses of the two nanoparticle-based calcium sensors described in Section 4.1.

4.5 Conclusions

Our efforts here demonstrate that a polymerization-driven MR contrast mechanism can be effectively deployed within the format of a discrete sensor. We focus on calcium sensing as a model but emphasize that this novel MR contrast mechanism may be applied to other hydrogels which crosslink with the introduction of alternative analytes of interest. A lack of true reversibility hinders the use of these sensors for *in vivo* applications. Future efforts could therefore be geared towards modifying alginate or alginate-derivatives in a manner allowing for improved sensor reversibility. Limiting the alginate sensing media to a much smaller sensor volume may also enhance sensor response if reliable MR relaxometry measurements could be made on such reduced volumes.

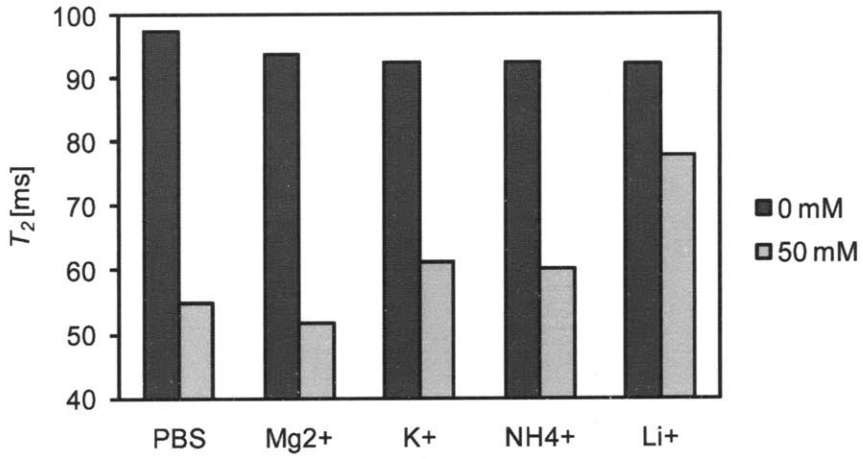

Figure 4.4: The T_2 response of alginate sensors to solutions of 0 mM and 50 mM $CaCl^2$containing additional ions.

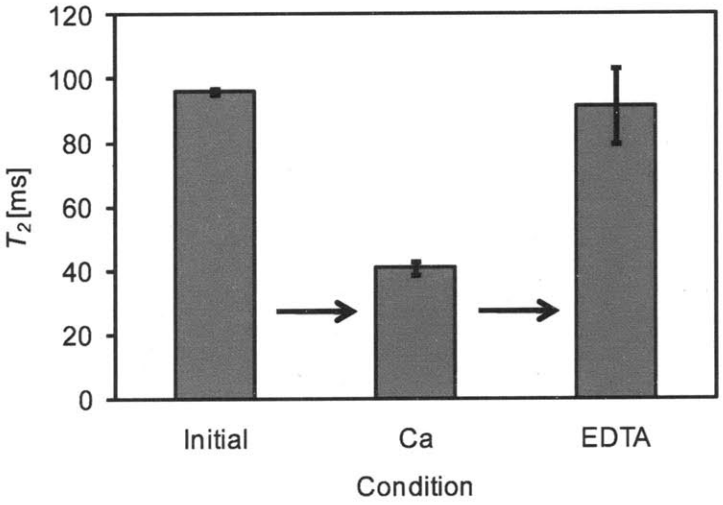

Figure 4.5: A sensor which has been exposed to calcium can be reversed by equilibration within an EDTA buffer. EDTA sequesters calcium. The data is plotted as the mean of n=3 samples and the error bars correspond to the standard error.

4.6 Materials and Methods

4.6.1 Device Preparation

Alginate (Sigma) was dissolved in deionized water at 5% w/v by mixing for 24 hr at room temperature. 100 μL of alginate pre-gel was next transferred to and enclosed within Slide-a-Lyzer MINI Dialysis Units (Pierce), shown in Figure 4.6, and placed within 1 mL sample baths containing $CaCl_2$ and other ions (as specified) to allow for sensor equilibration. Relaxivity measurements were made on a single sided proton NMR relaxometer; the devices were briefly removed from the sample baths for the duration of the measurement.

Figure 4.6: Image of a Slide-a-Lyzer MINI Dialysis Unit. The alginate pre-gel is loaded into the reservoir; the unit can then be equilibrated with $CaCl_2$ solution through the membrane. Image reproduced from Pierce.

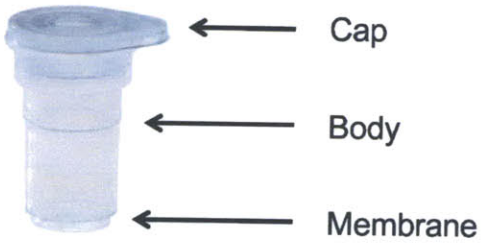

4.6.2 Determination of Proton Relaxation Time

Proton relaxation measurements were obtained on a custom-built system using a single-sided nuclear magnetic resonance (NMR) sensor (0.43 T and 25°C; Profile NMR MOUSE, ACT Center for Technology, Aachen, Germany). Transverse relaxation times were measured using a Carr Purcell Meiboom Gill (CPMG) sequence with the following parameters: echo time (TE) = 0.035 ms, 5714 echoes, 16 scans, and recovery time (TR) = 3 s. The echo peak intensities were fit to the equation $I = I_0 e^{-t/T2}$ using a custom script running on MATLAB (The Mathworks, Natick, MA). Transverse relaxation time constants measured on the single-sided system are lower than T_2 measured on a homogeneous field magnet system. Note that the amount by which the value is reduced is dependent upon the field gradient, the pulse sequence parameters and a combination of the sample's T_1 and T_2.

4.8 References

1. Stosiek C, Garaschuk O, Holthoff K, & Konnerth A (2003) In vivo two-photon calcium imaging of neuronal networks. *Proc Natl Acad Sci U S A* 100(12):7319-7324 .
2. Wallingford JB, Ewald AJ, Harland RM, & Fraser SE (2001) Calcium signaling during convergent extension in Xenopus. *Curr Biol* 11(9):652-661 .
3. Biessels G & Gispen WH (1996) The calcium hypothesis of brain aging and neurodegenerative disorders: significance in diabetic neuropathy. *Life Sci* 59(5-6):379-387 .
4. Siau C & Bennett GJ (2006) Dysregulation of cellular calcium homeostasis in chemotherapy-evoked painful peripheral neuropathy. *Anesth Analg* 102(5):1485-1490 .
5. Peterlik M, Grant WB, & Cross HS (2009) Calcium, vitamin D and cancer. *Anticancer Res* 29(9):3687-3698 .
6. Peterlik M & Cross HS (2009) Vitamin D and calcium insufficiency-related chronic diseases: molecular and cellular pathophysiology. *Eur J Clin Nutr* 63(12):1377-1386 .
7. Atanasijevic T, Shusteff M, Fam P, & Jasanoff A (2006) Calcium-sensitive MRI contrast agents based on superparamagnetic iron oxide nanoparticles and calmodulin. *Proc Natl Acad Sci U S A* 103(40):14707-14712 .
8. Atanasijevic T & Jasanoff A (2007) Preparation of iron oxide-based calcium sensors for MRI. *Nat Protoc* 2(10):2582-2589 .
9. Taktak S, Weissleder R, & Josephson L (2008) Electrode chemistry yields a nanoparticle-based NMR sensor for calcium. *Langmuir* 24(14):7596-7598 .
10. Hwang YS, *et al.* (2009) The use of murine embryonic stem cells, alginate encapsulation, and rotary microgravity bioreactor in bone tissue engineering. *Biomaterials* 30(4):499-507 .
11. Murphy CL & Sambanis A (2001) Effect of oxygen tension and alginate encapsulation on restoration of the differentiated phenotype of passaged chondrocytes. *Tissue Eng* 7(6):791-803 .
12. Nakamura K, *et al.* (2004) Oral insulin delivery using P(MAA-g-EG) hydrogels: effects of network morphology on insulin delivery characteristics. *J Control Release* 95(3):589-599 .
13. Kim B & Peppas NA (2003) In vitro release behavior and stability of insulin in complexation hydrogels as oral drug delivery carriers. *Int J Pharm* 266(1-2):29-37 .
14. Baumgartner S, Lahajnar G, Sepe A, & Kristl J (2002) Investigation of the state and dynamics of water in hydrogels of cellulose ethers by 1H NMR spectroscopy. *AAPS PharmSciTech* 3(4):E36 .
15. McConville P, Whittaker MK, & Pope JM (2002) Water and polymer mobility in hydrogel biomaterials quantified by H-1 NMR: A simple model describing both T-1 and T-2 relaxation. *Macromolecules* 35(18):6961-6969 .
16. Paradossi G, Cavalieri F, & Crescenzi V (1997) 1H NMR relaxation study of a chitosan-cyclodextrin network. *Carbohydr Res* 300(1):77-84 .
17. Shoichet MS, Li RH, White ML, & Winn SR (1996) Stability of hydrogels used in cell encapsulation: An in vitro comparison of alginate and agarose. *Biotechnol Bioeng* 50(4):374-381 .
18. Lu MZ, Lan HL, Wang FF, Chang SJ, & Wang YJ (2000) Cell encapsulation with alginate and alpha-phenoxycinnamylidene-acetylated poly(allylamine). *Biotechnol Bioeng* 70(5):479-483 .
19. Koch S, Schwinger C, Kressler J, Heinzen C, & Rainov NG (2003) Alginate encapsulation of genetically engineered mammalian cells: comparison of production devices, methods and microcapsule characteristics. *J Microencapsul* 20(3):303-316 .

20. Ghidoni I, *et al.* (2008) Alginate cell encapsulation: new advances in reproduction and cartilage regenerative medicine. *Cytotechnology* 58(1):49-56 .
21. Wan LS, Heng PW, & Chan LW (1992) Drug encapsulation in alginate microspheres by emulsification. *J Microencapsul* 9(3):309-316 .
22. Wang SB, Chen AZ, Weng LJ, Chen MY, & Xie XL (2004) Effect of drug-loading methods on drug load, encapsulation efficiency and release properties of alginate/poly-L-arginine/chitosan ternary complex microcapsules. *Macromol Biosci* 4(1):27-30 .
23. Gilchrist T & Martin AM (1983) Wound treatment with Sorbsan--an alginate fibre dressing. *Biomaterials* 4(4):317-320 .
24. Lam PK & Chan ES (2000) In vitro elution of antibiotic from antibiotic-impregnated biodegradable calcium alginate wound dressing. *J Trauma* 48(2):361-362 .
25. Matthew IR, Browne RM, Frame JW, & Millar BG (1993) Tissue response to a haemostatic alginate wound dressing in tooth extraction sockets. *Br J Oral Maxillofac Surg* 31(3):165-169 .
26. Franzesi GT, Ni B, Ling Y, & Khademhosseini A (2006) A controlled-release strategy for the generation of cross-linked hydrogel microstructures. *J Am Chem Soc* 128(47):15064-15065 .
27. McConville P & Pope JM (2001) H-1 NMR T-2 relaxation in contact lens hydrogels as a probe of water mobility. *Polymer* 42(8):3559-3568 .
28. Swift TJ & Connick RE (1962) Nmr-Relaxation Mechanisms of 017 in Aqueous Solutions of Paramagnetic Cations and Lifetime of Water Molecules in First Coordination Sphere. *Journal of Chemical Physics* 37(2):307-& .
29. Ablett S, Lillford PJ, Baghdadi SMA, & Derbyshire W (1978) Nuclear Magnetic-Resonance Investigations of Polysaccharide Films, Sols, and Gels .1. Agarose. *Journal of Colloid and Interface Science* 67(2):355-377 .
30. Barbieri R, Quaglia M, Delfini M, & Brosio E (1998) Investigation of water dynamic behaviour in poly(HEMA) and poly(HEMA-co-DHPMA) hydrogels by proton T-2 relaxation time and self-diffusion coefficient nmr measurements. *Polymer* 39(5):1059-1066 .
31. Kennan RPR, K.A.; Zhong, J.; Maryanski, M.J.; Gore, J.C. (1996) The Effects of Cross-Link Density and Chemical Exchange on Magnetization Transfer in Polyacrylamide Gels. *Journal of Magnetic Resonance, Series B* 110(3):267-277.

Chapter 5

MR Readable pH Sensor

MR measurements can be made at a distance and through intervening layers of matter. This property makes magnetic resonance imaging possible and MR parameters an attractive readout for implanted sensors. We described, in Chapters 2 and 3, MR readable assays that rely on analyte mediated clustering or dispersal of superparamagnetic iron oxide nanoparticles. We report here on a novel implantable pH sensor which does not depend on the MRSw phenomenon. MR contrast is instead generated by pH-responsive hydrogels. We characterize its sensitivity and dynamic response. Preliminary experiments suggest differences in proton chemical exchange rate to underlie its operational mechanism.

5.1 Motivation

pH is an important physiological parameter and a useful disease biomarker (1). Lindner and Raghavan showed (Figure 5.1), for instance, that drug-sensitive melanomas exhibit marked changes in *in vivo* pH after doxorubicin (a chemotherapeutic) administration whereas drug-resistant melanomas do not (2). The implication is that periodic tumor pH measurements could provide early insight into treatment effectiveness.

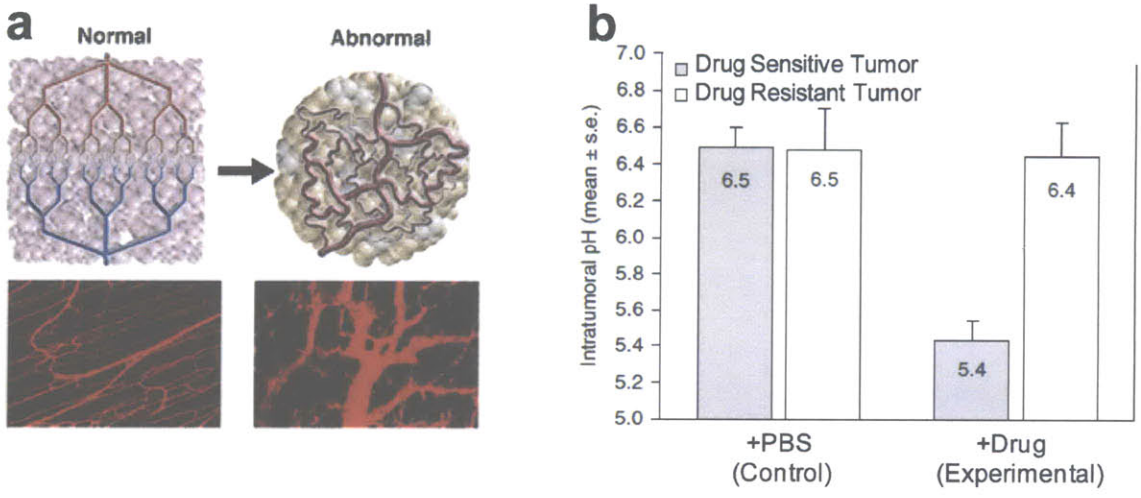

Figure 5.1: A deranged tumor vasculature leads to pH dysregulation of the interstitial space. **a**, Tumor vasculature is tortuous and irregular as compared to normal vasculature. **b**, Lindner and Raghavan (2) showed the pH of drug-sensitive tumor to drop in response to therapy whereas the drug-resistant tumor exhibits no change.

Current measurement techniques are not practical for high-frequency pH sampling. The standard method for *in vivo* pH determination is direct sampling via a needle electrode. The technology is reliable and the approach straightforward but measurement is invasive, making periodic sampling impractical. An alternative strategy, based on chemical exchange saturation transfer (CEST) MRI, affords spatial resolution (3). The expense of the equipment and complexity of the method, however, makes CEST MRI impractical for periodic sampling as well. This motivates us to develop a discrete MR readable sensor for which pH modulates T_2 and which can be rapidly interrogated using relatively straightforward proton NMR relaxometry. There was no clear way to adapt MRSw for the measurement of pH so we chose instead to exploit the chemical exchange mechanism of a pH-sensitive hydrogel. Poly[(diethylaminoethyl methacrylate)-*graft*-(ethylene glycol)], henceforth referred to as p(DEAEM-*g*-EG), was chosen because it possesses pH-sensitive amine groups (5).

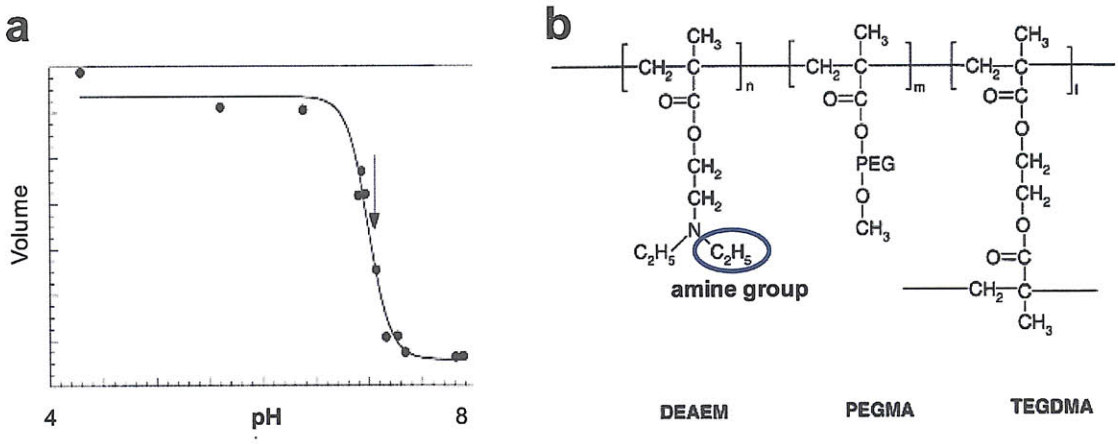

Figure 5.2: The molecular structure of p(DEAEM-*g*-EG) gels makes them sensitive to the pH of the hydration buffer. **a**, The swelling/shrinking behavior of p(DEAEM-*g*-EG) gels is thought to be driven by, **b**, the pH sensitivity of the polymer's amine groups. This figure is reproduced from Podual *et. al* (4).

These functional groups make the gel swell and shrink in response to the pH of its hydration buffer (Figure 5.2). We posited the hydrogel's exchangeable protons can serve as a source of relaxation for water so pH-dependent differences in exchange rates would drive corresponding differences in water proton relaxation.

5.2 p(DEAEM-g-EG) Characterization

Many macromolecules in solution possess loosely bound protons (usually hydroxyl, amine, sulfide) capable of undergoing direct chemical exchange with free water (6-8). The relaxation properties of a non-water proton source can transfer to water when exchange is sufficiently rapid (Figure 5.3). We began our investigation of p(DEAEM-*g*-EG) gels as a pH-sensitive MR contrast medium by finding the T_2 of gels to be an order of magnitude shorter than the T_2 of deionized (DI) water as measured on a standard proton NMR relaxometer. This behavior is consistent with the chemical exchange mechanism. More relevant to our present aim, the transverse relaxivity of the gels varies with the pH of the hydration buffer (Figure 5.4a). A consideration of the contrast mechanism follows.

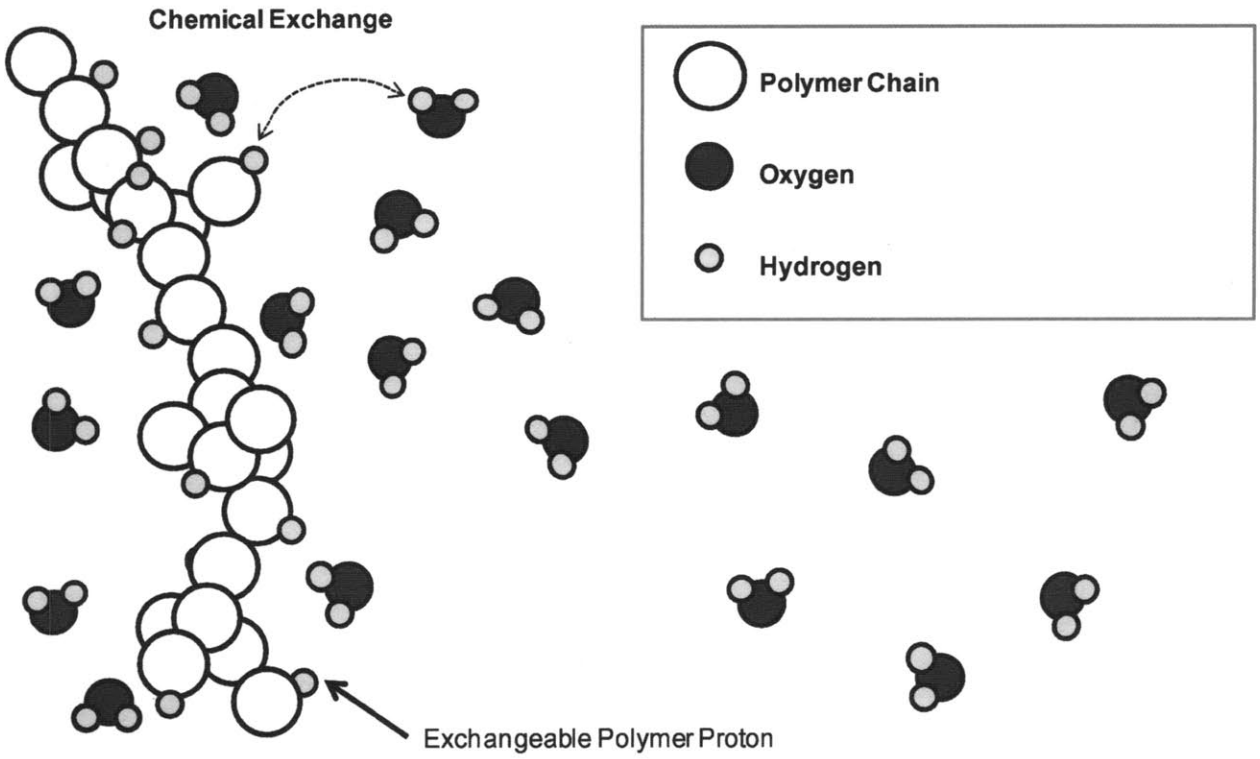

Figure 5.3: Exchangeable polymer protons reduce the relaxivity of free water.

5.2.1: Hydrogel Relaxation

Hydrogels are hydrophilic polymers composed primarily of water. The magnetic relaxation of water can be described by a single exponential but the relaxation of a hydrogel is more complex. The primary reasons are: 1) the polymer protons themselves contribute to the NMR signal, 2) the mobility of polymer 'bound' water molecules is decreased and these protons relax more quickly, 3) dipole-dipole cross-relaxation of water molecules can occur through the nuclear Overhauser effect (NOE), 4) chemically exchangeable polymer protons can directly transfer their magnetization to water. Several 'pools' of protons may therefore be represented in the magnetic relaxation of a hydrogel. These complexities notwithstanding, hydrogel relaxation is most often modeled as two components coupled by chemical exchange. This model, adapted from McConville et al. (9) and Ablett et al. (10), assumes the long T_2 component to be free water and the short T_2 component to be exchangeable polymer protons:

$$\frac{1}{T_2} = \frac{1-p}{T_{2fw}} + \frac{p}{T_{2polymer} + \tau_{ex}}$$

T_2 is the measured single exponential transverse relaxation time of the overall signal. T_{2fw} is the transverse relaxation time of the free water pool. $T_{2polymer}$ is the transverse relaxation time of exchangeable polymer protons. p is the fraction of polymer protons within the overall system. τ_{ex} is the mean dwelling time of exchangeable polymer protons. This model approximates hydrogel relaxation as that of a single pool of relaxivity-enhanced water. It is considered adequate because the

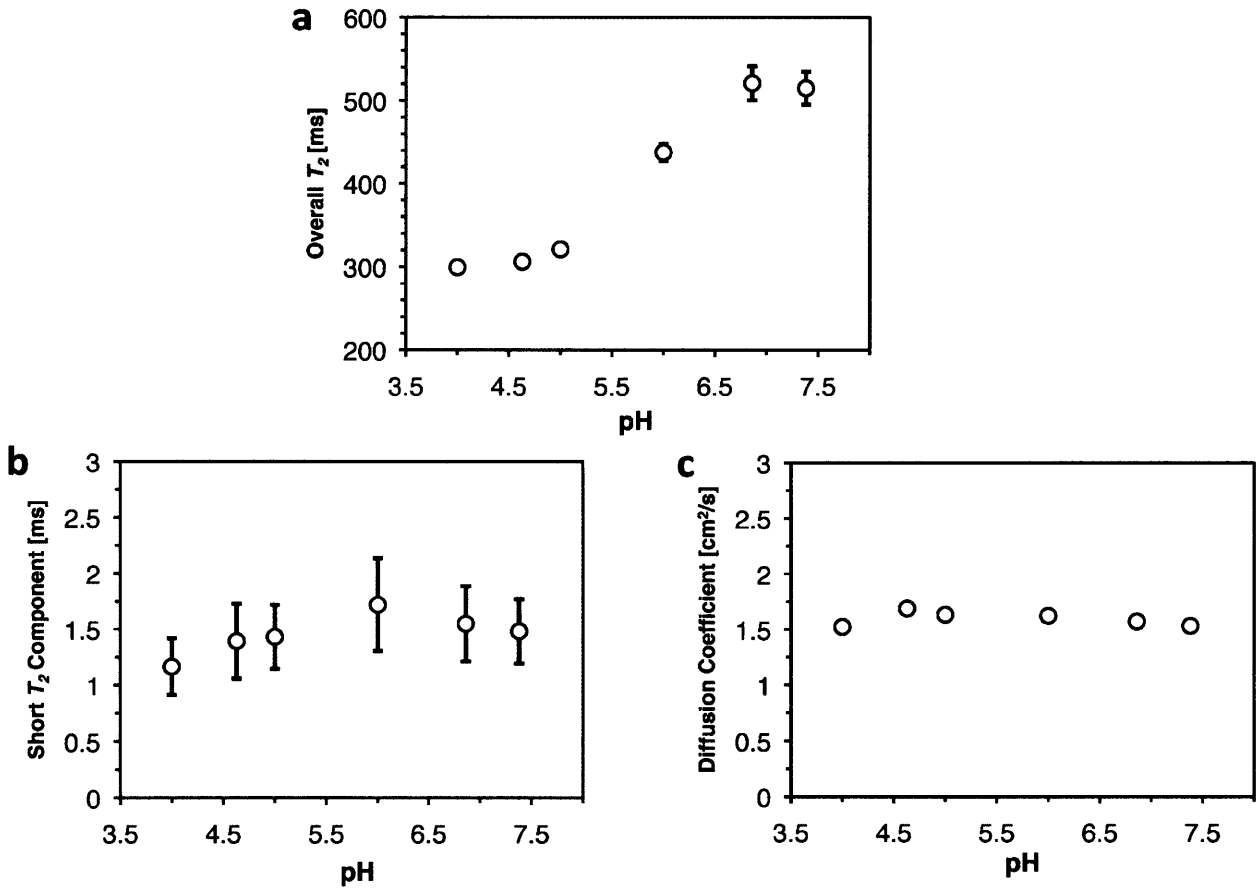

Figure 5.4: The overall T_2 of p(DEAEM-g-EG) gel varies with pH while water diffusivity and the short component of relaxation do not. **a**, Overall transverse relaxivity markedly increases with increasing pH (determined by the MiniSpec proton relaxometer). **b**, pH does not significantly influence the short T_2 component (determined in the MiniSpec proton relaxometer) or, **c**, water diffusivity within the gels (determined by diffusion MRI). Error bars correspond to the 95% confidence interval for the fit.

relaxivities of non-water sources are over two orders of magnitude shorter than that of free water (9). These sources contribute additional exponential decays atop the water signal but they are so brief as to be either NMR invisible (shorter than the echo time) or of no effective consequence when fitting a single-exponential decay to the overall signal.

5.2.2: Alternative Relaxation Mechanisms

Proton exchange rates are naturally pH-dependent. One study of amino acids in water, for example, showed the exchange rate to vary by several orders of magnitude with pH (11). A pH-dependent chemical exchange rate, captured in the model by τ_{ex}, therefore seems a reasonable candidate mechanism for driving the empirically observed pH dependence of the overall T_2. We noticed however, that the variables T_{2fw} and $T_{2polymer}$ may also respond to pH and so attempted to gauge their effect. Recall that p(DEAEM-g-EG) gels shrink and swell with pH. Excess protons accumulate on the polymer when the pH of the hydration buffer falls below the pKa of its amine groups. Electrostatic forces in turn cause the mesh to expand. We reasoned that physical rearrangement of the polymer chains might alter the energy transfer (i.e. spin coupling) properties between chemical

bonds thereby influencing the relaxivity of the polymer protons ($T_{2polymer}$). The short T_2 relaxation component was thus isolated (Figure 5.4b). There is a marked change in the overall T_2 as a function of pH, but no concomitant change in the short T_2 component. We next considered the possible role of intra-hydrogel water diffusivity, which could also be influenced by mesh size (i.e. swelling or shrinking). A sufficient reduction in water diffusion should be able to alter the relaxivity of free water (T_{2fw}). Diffusion MRI measurements (discussed in detail in section 5.5.3 below) revealed that intra-hydrogel water diffusivity does differ from that of water alone (~2.3 cm^2/s) but does not significantly vary over the pH range for which the overall T_2 varies (Figure 5.4c). These results suggest chemical exchange as likely to be the sole mechanism driving the pH dependence of T_2 in p(DEAEM-*g*-EG) gels. Direct measurements of chemical exchange by NMR spectroscopy were also acquired (described in Section 5.6.2); the results are qualitatively consistent with the hypothesis outlined above.

5.3 Sensor Performance

5.3.1 Response and Sensitivity

We designed sensors comprised of polyethylene shells which encapsulate the sensing media (described in Section 5.5.1). The enclosure incorporates a size-exclusion polycarbonate membrane to facilitate equilibration of sensing media with the external environment (Figure 5.5a). This form factor makes automation of periodic multi-sample measurements facile when using a single-sided proton relaxometer. Our subsequent sensor data was thus acquired using this instrument, which possesses substantially reduced sensitivity as compared to a MRI scanner or the MiniSpec proton relaxometer. The pH dependence of p(DEAEM-*g*-EG) gel (independent of the sensor) relaxivity was confirmed, prior to encapsulation within sensors, to be measurable by single-sided relaxometry despite the instrument's reduced sensitivity (Figure 5.5b, orange squares). Relaxivity-enhancing magnetic nanoparticles (5 μg/mL Fe concentration) were then added to the hydration buffer so as to reduce the requisite measurement time (Figure 5.5b, grey circles). We chose, based on these results, to include the nanoparticles (which are too large to diffuse through the membrane pores) in the sensor because this additional component had no meaningful effect on T_2 differences across the pH range of interest.

Measurements were taken from sensors immersed in buffer. The measured signals consequently possess a contribution from the surrounding aqueous phase as the sensors are slightly smaller than the measurement volume of the single-sided relaxometer. This accounts for the attenuation of the pH-dependent T_2 differences of sensor measurements (Figure 5.5c) as compared to gel measurements (Figure 5.5b, orange squares). The sensor T_2 response curve appears similar to that obtained from bulk material (Figure 5.4a) and roughly linear with pH in the physiologically interesting 5 to 7.4 range. Its sigmoidal shape also qualitatively resembles that of the swelling-ratio curves previously reported for p(DEAEM-*g*-EG) gel.

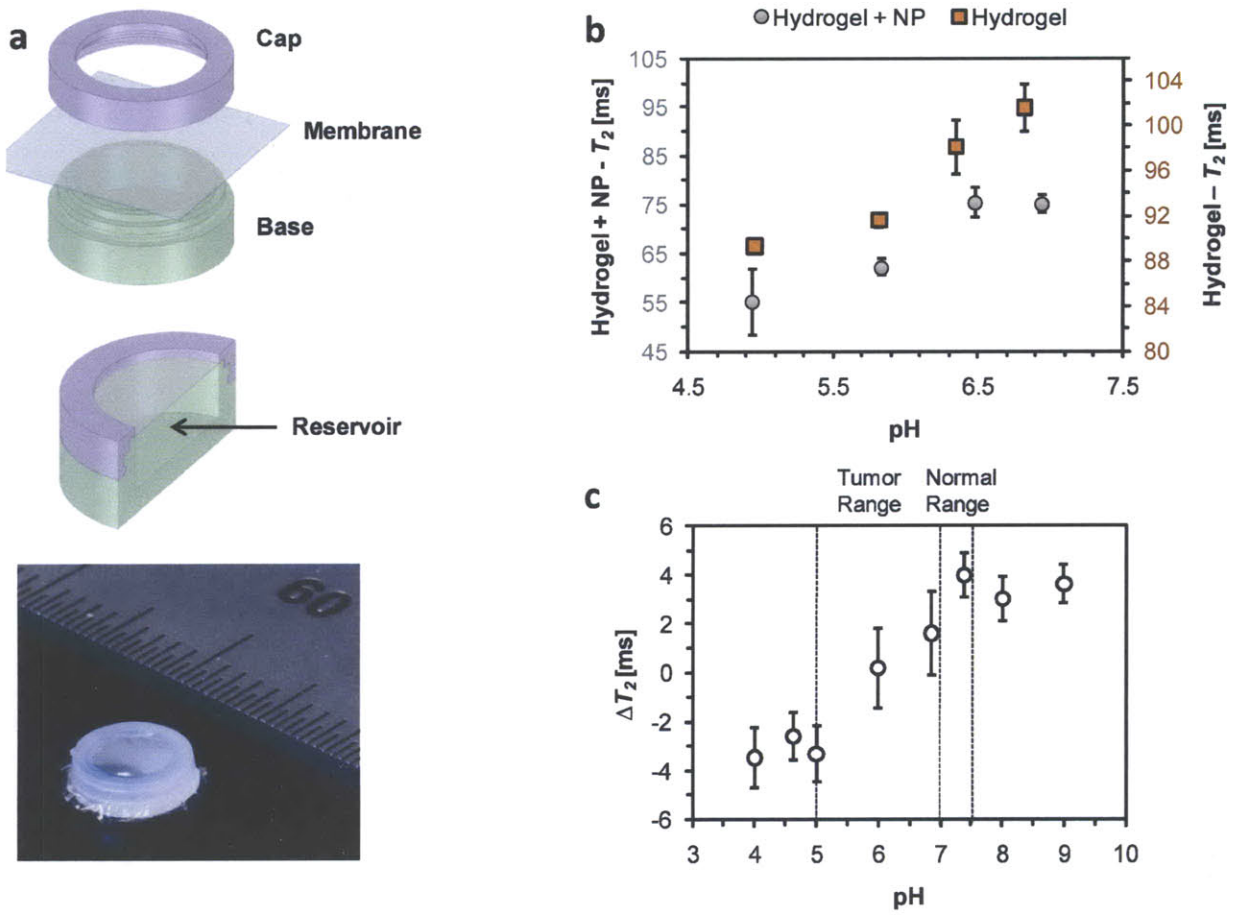

Figure 5.5: p(DEAEM-*g*-EG) gel can be incorporated within sensors which may be read by a single-sided proton relaxometer. **a**, The sensor body consists of a cap and base which snap fits to sandwich a size-exclusion membrane and form an enclosed reservoir. **b**, A positive correlation between pH and T_2 holds both with (light grey) and without (dark grey) the additional presence of relaxivity-enhancing SPIO nanoparticles (measured using a single-sided proton relaxometer). **c**, When encapsulated within discrete sensors the gels continue to exhibit pH dependent relaxivities. Characteristic tumor extracellular pH and normal tissue pH ranges are indicated. Error bars correspond to a 95% confidence interval of the average measured T_2 across n=3 samples.

5.3.2 Dynamics

Results from a time course study (Figure 5.6a) indicate that sensor equilibration requires no more than ~30 hr. Importantly, we find the sensors to be reversible (Figure 5.6b). Equilibration back to pH 7, which occurs within the 4 hr sampling period used, is more rapid than towards pH 4; this is consistent with literature showing more rapid pH-induced p(DEAEM-*g*-EG) shrinking than swelling (12). No MRSw assays have to date been shown to exhibit reversible nanoparticle clustering, perhaps as a result of the high-affinity binding moieties used. Taktak *et al.* reported (13), for instance, that MRSw functionalized to cluster about calcium ions only dispersed with the further addition of the calcium chelator EDTA. Such a strategy may be appropriate for *in vitro* assays but would be difficult to adapt for tracking real-time calcium levels *in vivo*. The reversible property of this gel-based sensor is hence a significant departure from the performance characteristics of MRSw based sensors.

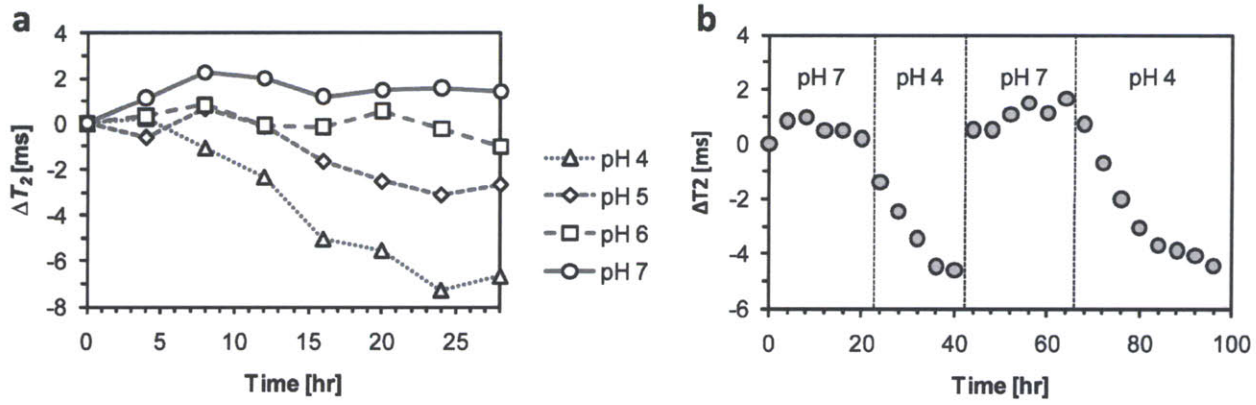

Figure 5.6: Sensor equilibration is not instant though its response is reversible. **a**, The dynamic response of sensors immersed in pH buffer shows equilibration to require no more than 30 hr. **b**, Sensor T_2 switches back-and-forth when the equilibration buffer is alternated between pH 7 and pH 4. Data points are plotted as the average across n=4 samples. Error bars (<1ms for each data point) are withheld to allow for easy visualization.

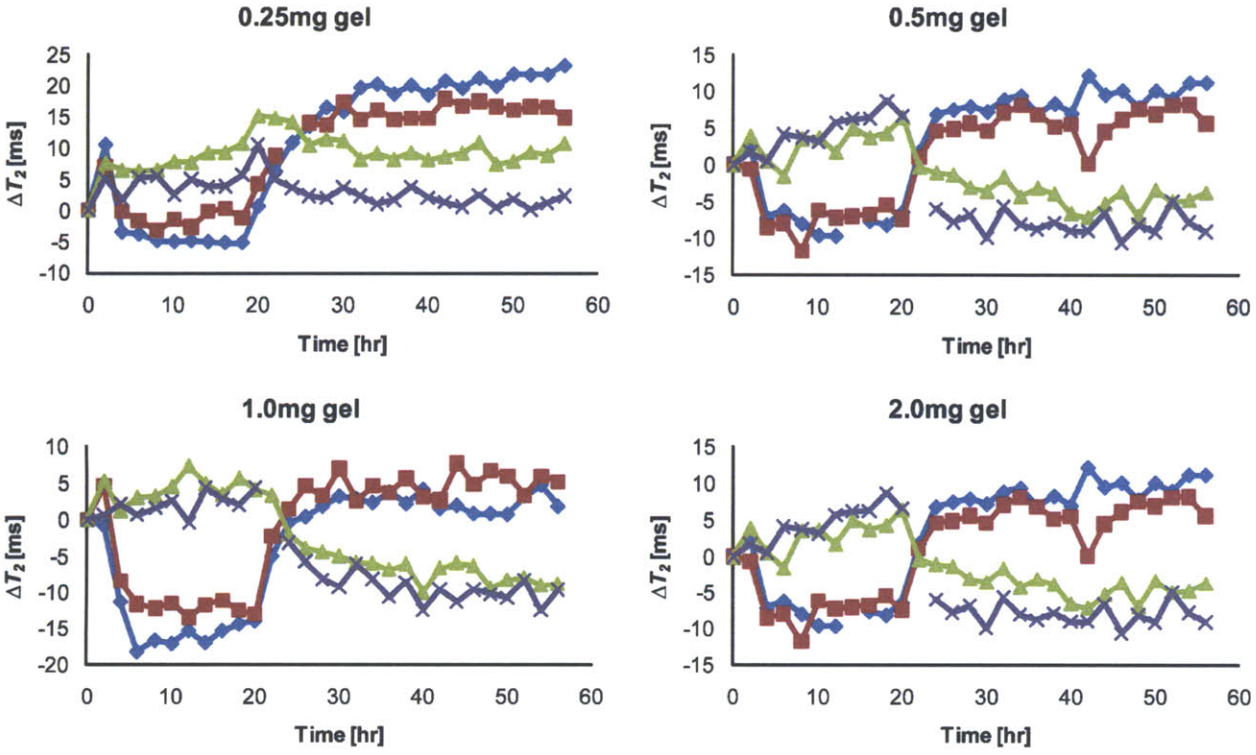

Figure 5.7: The response of sensors containing differing quantities of p(DEAEM-g-EG) gel is shown. Data points are plotted for individual devices. Red/blue data points correspond to devices moved from pH4 to pH7 at 20 hr; green/purple data points correspond to devices moved from pH7 to pH4 at 20 hr. Error bars (<1ms for each data point) are withheld to allow for easy visualization.

We further explored the effect of gel quantity on sensor response (Figure 5.7). The results indicate that at least 0.5 mg of gel is needed to produce a consistent result. It is likely that the read volume of the single-sided relaxometer is larger than the gel volume when gel quantity falls below 0.5 mg. The results previously shown in Figure 5.6 were acquired from sensors containing 1.0 mg of gel.

5.4 Conclusions

We have shown that p(DEAEM-*g*-EG) gels possess pH-dependent relaxivities and can be incorporated within discrete sensors to provide T_2 contrast. This is a break from past work with discrete MR sensors which relied on derivatives of the MRSw concept; it is also a second demonstration that mechanisms other than magnetic nanoparticle clustering can provide contrast for a MR readable sensor. Measurements made with a relatively insensitive single-sided relaxometer capture the pH response dynamics, and demonstrate sensor reversibility. We emphasize that resolution can be substantially enhanced (as seen in the gel characterization results) by using relaxometers possessing more homogeneous B_0 fields and are in the process of constructing a system specifically designed to measure small discrete sensors. Characterization results indicate the pH dependence of proton chemical exchange rates to drive differences in the measured overall T_2. We are at present applying these pH sensors for tracking cancer progression and response to therapy.

5.5 Materials and Methods

5.5.1 Device Preparation

Hydrogel Synthesis. 3.5 mL diethylaminoethyl methacrylate (DEAEM) and 1.9 g poly(ethylene glycol) monomethacrylate (PEGDMA) were dissolved in 1 mL EtOH and 1.2 mL 37% HCl. 68 μL tetraethylene glycol dimethacrylate (TEGDMA) crosslinker was added and the mixture was bubbled with nitrogen for 30 min. A redox pair, 0.12 mg ammonium persulfate (APS) and 0.12 mg sodium metabisulfite separately dissolved in 0.5 mL PBS, was then added to the above mixture to facilitate overnight polymerization at room temperature. Gel slabs were washed with DI H_2O, dried at 80°C for 2 days, cryomilled (SPEX Certiprep 6850 Freezer/Mill) to a powder of sub-100 μm particles, and stored under vacuum.

Sensor Fabrication. 1 mg hydrogel powder was enclosed within the snap-on sensor and hydrated by phosphate-buffered saline (PBS) or 5 μg/mL NanoMag-CLD 50 nm suspension (MicroMod). The sensor body consisted of a cap and base which can sandwich a 30 nm pore polycarbonate membrane (SPI Supplies) to form a discrete enclosed volume. The original CAD design for can be found on the next page in Figure 5.8. The cap and base were custom designed so as to easily snap together through application of manual pressure. Any excess membrane was then manually trimmed away.

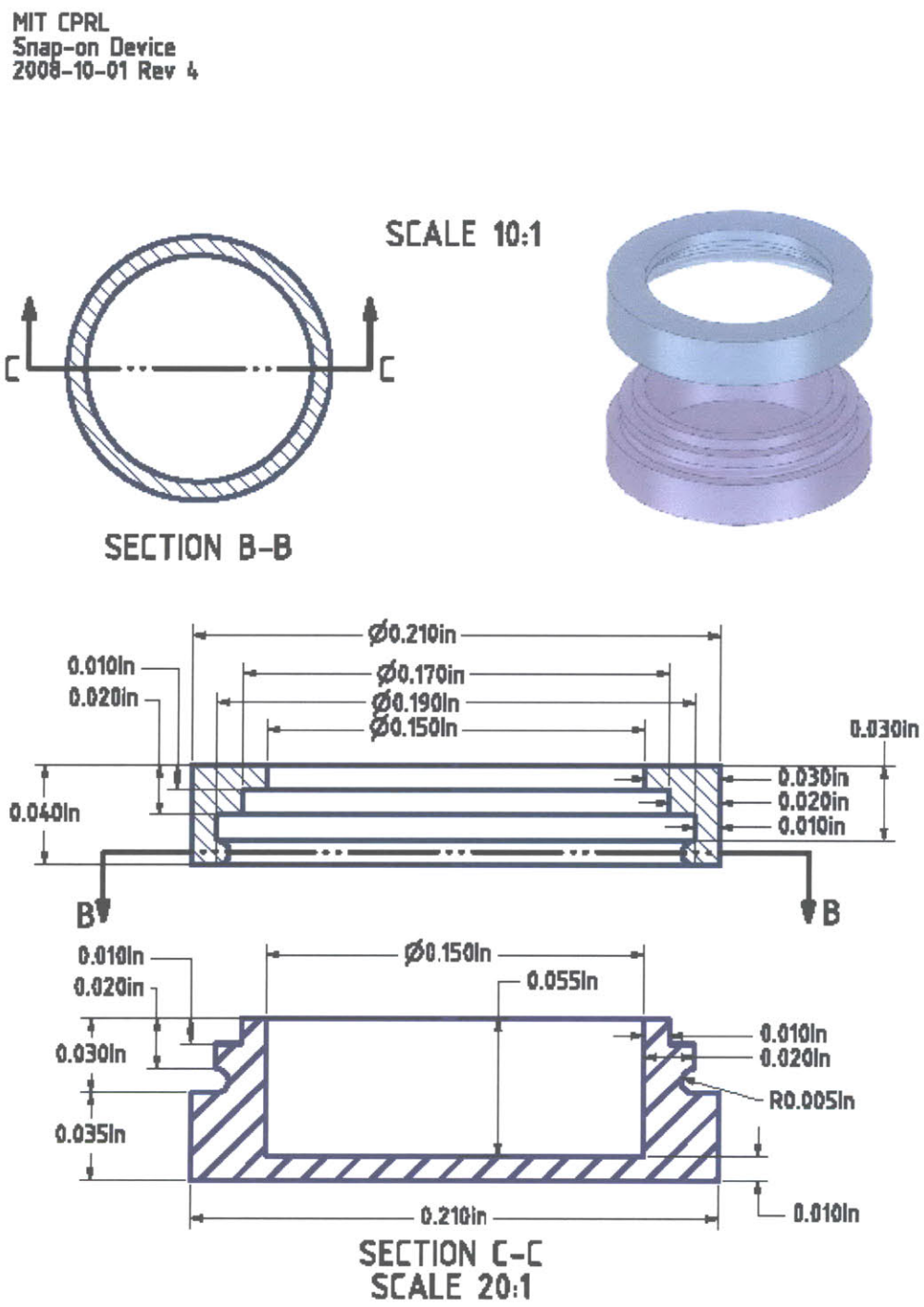

Figure 5.8: CAD drawing of snap-fit sensor device.

5.5.2 Relaxometry Measurements

The MR systems used in this work are summarized in Figure 5.9 below. Note that hydrogel transverse relaxivity is longer than water relaxivity when measured on the single-sided relaxometer but shorter than water relaxivity when measured by MiniSpec and MRI. The inherent lack of B_0 field homogeneity makes the single-sided relaxometer especially sensitive to reduced water diffusion within a hydrogel.

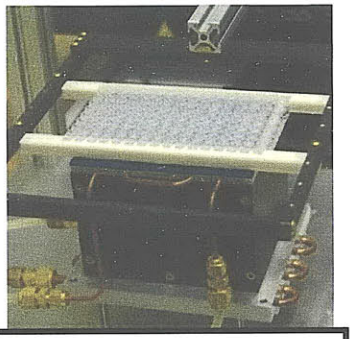

	MRI	Minispec	Single-Sided
Machine Operation	Requires shielded room, trained technician,	Benchtop, researcher operated	Benchtop, researcher operated
Scheduling	Must reserve time on machine weeks in advance	Accessible as typical laboratory instrument	Accessible as typical laboratory instrument
Throughput	~1 hour for: 16 wells in a 384-well plate 1 *in vivo* device	Can read one sample at a time, at ~1 minute/sample	Can automatically read up to 128 wells in sequence at ~ 30s/sample
Field Strength	7 T	0.47 T	0.43 T
Homogeneous Field	Yes	Yes	No
Controlled Gradients	Yes	No	No
DI Water T_2 (ms)	539 ± 4.2	3576 ± 20.3	88.3 ± 1.5
Hydrogel T_2 (ms)	286 ± 2.3	527 ± 17.8	102 ± 1.5

Figure 5.9: A summary of the practical and technical properties of the three MR systems used. Errors correspond to 95% confidence intervals.

Bruker MiniSpec Proton Relaxation Measurements. 25 mg hydrogel powder was hydrated with 8.5 mL pH buffer within 10 mm diameter NMR tubes. 7.5 mL of excess pH buffer was removed after 72 hr equilibration and prior to MR interrogation. Transverse relaxation times were measured using a Carr Purcell Meiboom Gill (CPMG) sequence with the following parameters: TE = 0.4 ms, 4 scans, TR = 40 s. The echo peak intensities were fit to the equation $I = I_0 e^{-t/T2}$ using a custom script running on MatLab (The Mathworks, Natick, MA). The short T_2 component was determined by fitting the initial 4 ms of data to a similar equation $I = I_0 e^{-t/T2} + C$ which possesses an additional offset constant.

Single-Sided Proton Relaxation Measurements. Device measurements were made using a custom-built single-sided magnetic resonance relaxometer (0.43 T and 25°C; Profile NMR MOUSE, ACT Center for Technology, Aachen, Germany). The unit's field gradient enables measurement of samples placed at a fixed location close (~300 μm) but external to the magnets. Contrast this measurement scheme with that used for proton NMR relaxometers possessing fairly homogeneous B_0 fields (such as the Bruker MiniSpec described above) for which the sample must be lowered into the magnetic coil. The unit was retrofitted with a programmable motion stage which could hold standard 8-well strips, thus enabling automated measurement of multiple samples over time. Individual devices (the construction of which is describe below) were measured upon being affixed to the bottom of 8-well strips and immersed in pH buffer. The relaxation of hydrogel alone (i.e. independent of the sensors) was also determined using macroscale vessels (described below in Section 5.5.3) manually placed atop the platform. Transverse relaxation times were measured using a CPMG sequence with the following parameters: TE = 0.035 ms, 5714 echoes, 16 scans, and TR = 3 s. The echo peak intensities were fit to the equation $I = I_0 e^{-t/T2}$ using a custom MatLab script. T_2 measured on this single-sided MR unit is lower than T_2 measured on a homogeneous field magnet system. The amount by which the value is reduced is dependent upon the field gradient, the pulse sequence parameters and a combination of the sample's T_1 and T_2.

5.5.3 Diffusivity Measurements

Diffusion MRI Measurements. Diffusion MRI measurements were obtained on a 7 T Bruker scanner (Billerica, MA) from hydrogel samples enclosed within macroscale containers. Specifically, 1 g p(DEAEM-*g*-EG) powder was hydrated with 8 mL pH buffer in diffusion vessels (Macro Fast DispoDIALYZER™, Harvard Apparatus) enclosed by 30 nm pore polycarbonate membranes. The vessels were equilibrated in 500 mL pH buffer for over 1 week before measurement. Diffusivity was determined by fitting signal intensity to the equation $A \propto e^{-bD}$ across approximately 1 cm x 2.5 cm regions of interest. Parameter *b* was experimentally varied by tuning gradient amplitude. All pH buffers (BDH) were adjusted to 0.15 mM with NaCl before use.

Description of Diffusion MRI. This section provides a brief discussion of MRI based diffusion measurements. Water molecules in an aqueous sample are constantly moving. They tumble and collide with one another, exhibiting both rotational and translational displacement over time. Though the movement of individual molecules is random and unpredictable, the dynamics of a population can be described by a statistical process. The key idea is that a set of particles which begin at a single location will disperse over time. The variance of this population along a single axis x will after time T possess a variance of $\sigma_x^2 = 2DT$.
D, given in units of [distance^2]/[time], is a characteristic diffusion constant describing the rate of particle dispersion. Note the square relationship; the characteristic diffusion distance σ_x doubles when T is quadrupled. This makes diffusion-based movement fairly efficient over short distances but very slow across long distances.

It is possible to directly measure diffusion in MR by using a pair of mutually offsetting gradient pulses after application of a 90° excitation pulse (Figure 5.10). Let us for simplicity assume $\delta t << T$. The spatial location of water molecules is therefore encoded by the (brief) first gradient pulse, acquiring a position-dependent phase of $\theta=\gamma G x \delta t$ (γ is the gyromagnetic ratio, G is gradient amplitidue and δt its duration, and x is the spatial location). Water is free to diffuse through duration T. If a molecule remains stationary, the second (reversed) gradient will perfectly unwind the original phase encoding. If however a molecule diffuses Δx away from its original position, it will experience phase dispersion in proportion to the magnitude of its displacement, $\theta=\gamma G(\Delta x)\delta t$. This effect attenuates the cumulative signal of the dispersed/diffused water molecules. As the spatial dispersal subsequent to diffusion of a population follows a Gaussian distribution, so must its phase dispersal $\sigma_\theta^2 = 2DT(\gamma G \delta t)^2$. Gaussian phase dispersal produces an exponential signal attenuation so readout amplitude A(D) is a function of the diffusion coefficient D:

$A(D) = e^{-bD}$

The parameter $b = (\gamma G \delta t)^2(T-\delta t/3)$, can be experimentally varied by modulation of the gradient amplitude (or duration). The diffusion constant can therefore be measured in MR by finding the parameters for a curve fit to two or more points along the attenuation curve.

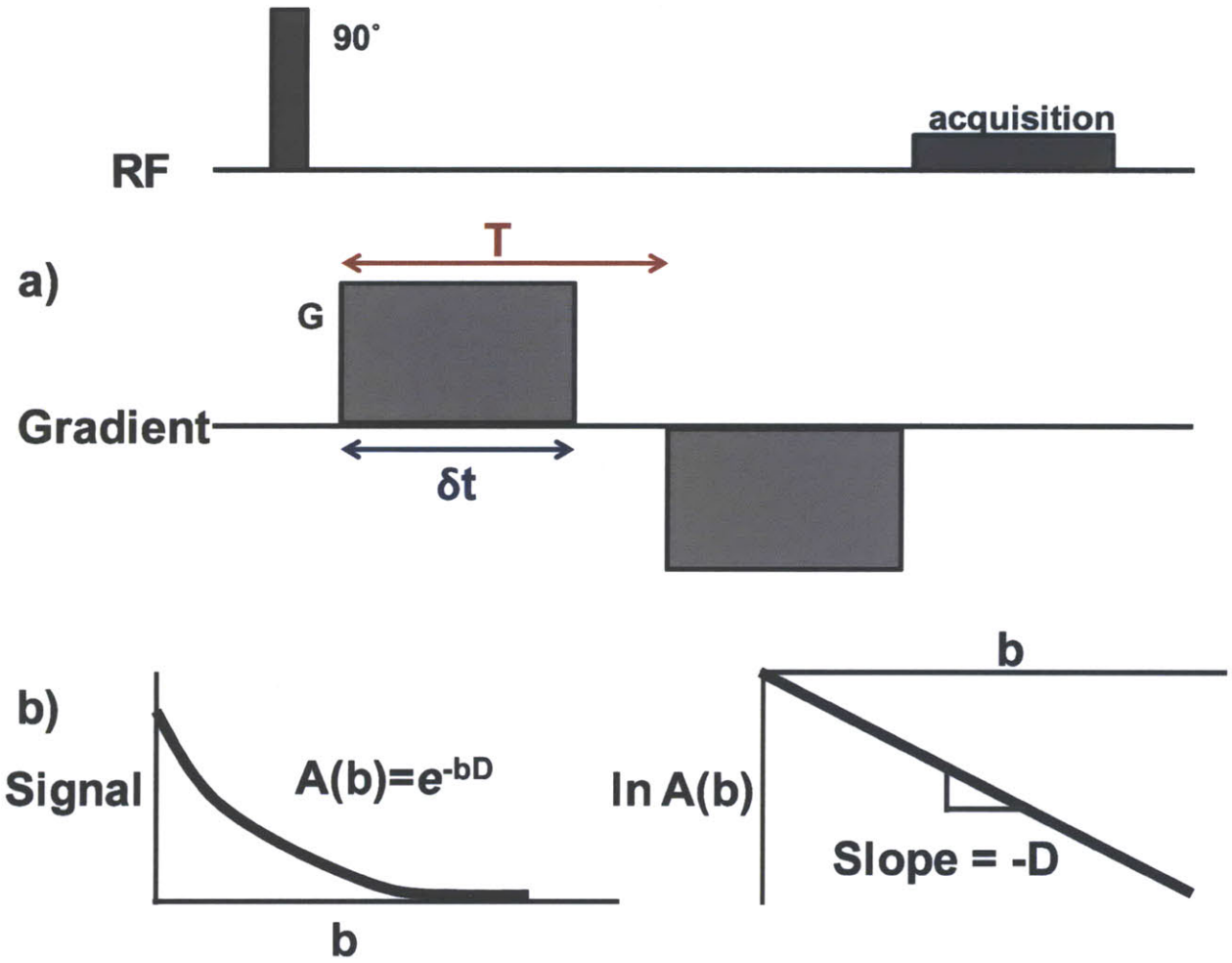

Figure 5.10: **a**, The MR signal is made sensitive to diffusion by applying a bipolar gradient pulse between signal excitation and signal detection. **b**, If spins were stationary, the additional position-dependent precessional phase acquired during the first gradient pulse would be precisely unwound by the second gradient pulse, and there would be no effect on the net measured signal. With diffusion, the random displacements of water molecules between the two gradient pulses produce random phase offsets and signal attenuation. The attenuation is exponential in the term bD, where b is an experimental parameter that depends on the gradient strength and duration, and D is the diffusion coefficient. Figure and caption adapted from Buxton's *Introduction to Functional Magnetic Resonance Imaging* (14).

5.6 Appendix

5.6.1 An Alternative pH-Sensitive Hydrogel

p(DEAEM-*g*-EG) gels were used in the above pH sensor to generate relaxivity-based MR contrast. Our results indicate that its pH-dependent contrast is driven by a proton chemical exchange mechanism. Poly(acrylamide-co-acrylic acid), which we will refer to as p(AM-co-AA), is an alternative hydrogel which possesses similar pH-sensitive swelling/shrinking properties. Its responsiveness depends, however, on the protonation or deprotonation of carboxyl (pKa≈5) rather than amine groups. p(AM-co-AA) also swells rather than shrinks at higher pH (Figure 5.11). This swelling/shrinking behavior was experimentally verified (not shown as it appears similar to the left panel of Figure 5.11).

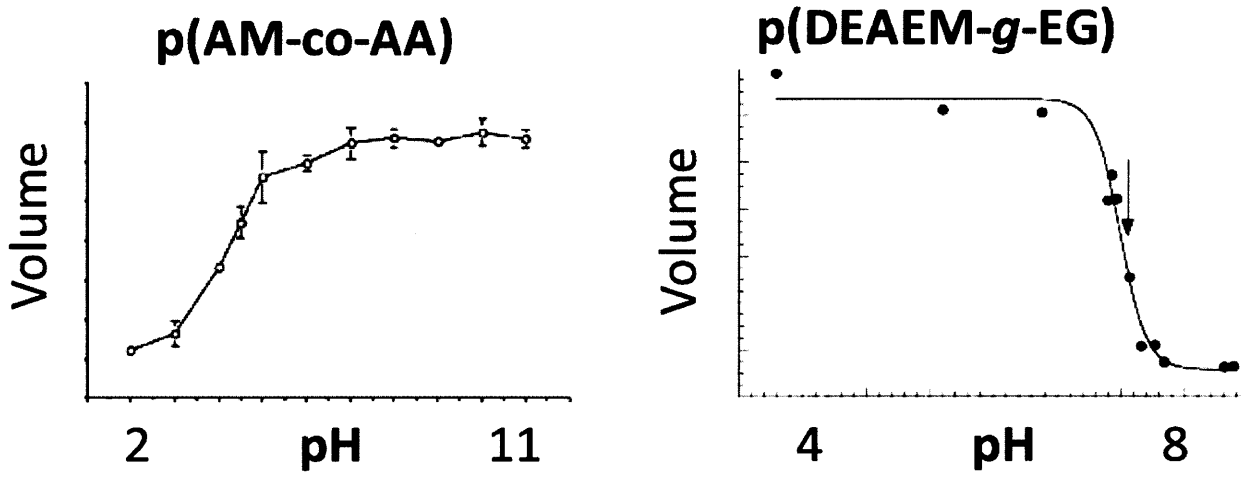

Figure 5.11 The swelling response curves of p(AM-co-AA) and p(DEAEM-*g*-EG) hydrogels. This figure is reproduced from Gemeinhart *et. al* (15) and Podual *et. al* (4).

5.6.1.1 Contrast Mechanism

We studied the MR relaxivity of p(AM-co-AA) to determine whether the chemical exchange mechanism is generalizable to this gel which possesses an alternative chemistry. The polymer was hence synthesized, milled, and filled into the chamber of the snap-on devices in a manner identical to that described above for p(DEAEM-*g*-EG) gels. Sensors possessing both gel alone, and gel doped with relaxivity-enhancing 50 nm magnetic nanoparticles, were equilibrated in pH 4 and pH 7.4 buffers (Figure 5.12). The results, acquired through single-sided proton relaxometry, indicate that nanoparticles must be added to p(AM-co-AA) gels to generate pH-dependent contrast. This behavior stands in contrast to that of p(DEAEM-*g*-EG) gels which generate contrast on their own own.

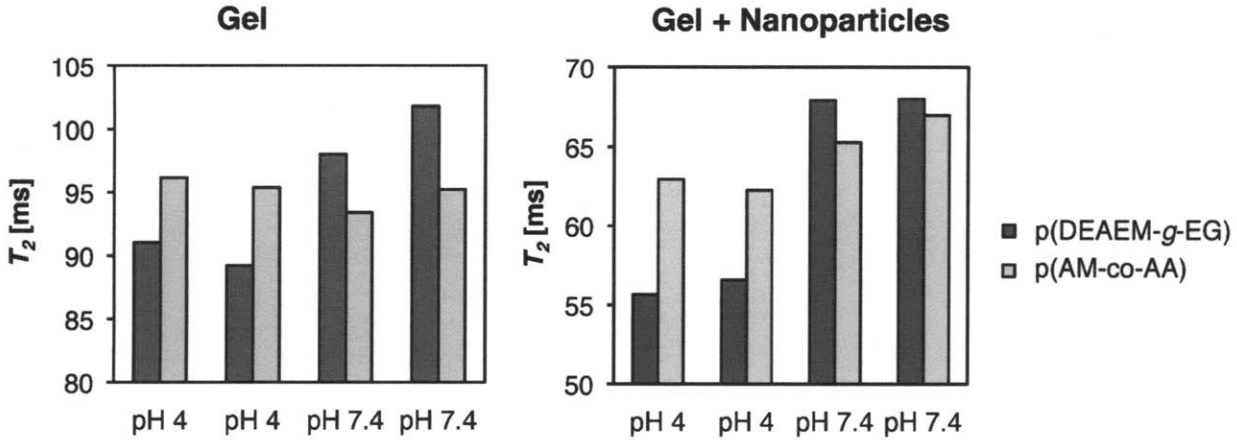

Figure 5.12 The T_2 of sensors, possessing both p(DEAEM-g-EG) and p(AM-co-AA) hydrogels, equilibrated in pH 4 or pH 7.4 buffers (left). Inclusion of 30 nm magnetic nanoparticles in the hydration buffer allowed p(AM-co-AA) sensors to generate pH-dependent contrast (right). Fit error bars are too small to be visible on these scales.

One simple explanation for these findings appeals to instrument inadequacy. The single-sided relaxometer used in making these measurements is fairly insensitive in the T_2 range of the gels (90 to 100 ms). Proton exchange rates in p(AM-co-AA) gels are pH sensitive but perhaps do not vary by the same magnitude as in p(DEAEM-*g*-EG) gels. The single-sided relaxometer might therefore be able to resolve the chemical exchange differences generated in p(DEAEM-*g*-EG) gels but not in p(AM-co-AA) gels. Nanoparticle inclusion reduces the baseline rate of relaxation to a range (50 to 70 ms) in which the instrument can resolve these differences in chemical exchange for p(AM-co-AA) based sensors.

An alternative possibility is that chemical exchange does not actually generate pH-dependent MR contrast in p(AM-co-AA) gels. There is no indication in the literature that carboxyl groups are NMR-visible sites of proton chemical exchange. Some interaction of nanoparticles with the polymer matrix must therefore be involved in producing the T_2 differences generated in p(AM-co-AA) sensors. We probed any potential interaction by assessing whether nanoparticles move freely within or are trapped by the gel mesh. The relaxivities of p(AM-co-AA) and p(DEAEM-*g*-EG) gels hydrated within buffers containing nanoparticles of varying diameters (20 nm, 50 nm, 100 nm) were determined (Figure 5.13a and 5.13c). p(AM-co-AA) gels appear able to generate pH-dependent T_2 differences only if 50 nm or 100 nm nanoparticles are included. Note that the T_2 of p(AM-co-AA) gels incorporating the 20 nm nanoparticles do not respond to pH differences. Excess buffer was intentionally used so that the sample supernatants could be extracted and quantified by relaxometry (Figure 5.13b and 5.13d). The T_2's of the supernatants are proportional to particle uptake. The results thus indicate that p(DEAEM-*g*-EG) gels do not 'absorb' nanoparticles from the buffer but that p(AM-co-AA) gels do, and in a particle size-dependent manner. p(AM-co-AA) absorbs more of the 50 nm and 100 nm nanoparticles at pH 7.4 than at pH 5, but do not absorb 20 nm particles. This finding matches the gel relaxivity results (Figure 5.12a); p(AM-co-AA) sensors produce pH-dependent contrast in the presence of 50 nm and 100 nm particles but do not in the presence of 20 nm particles.

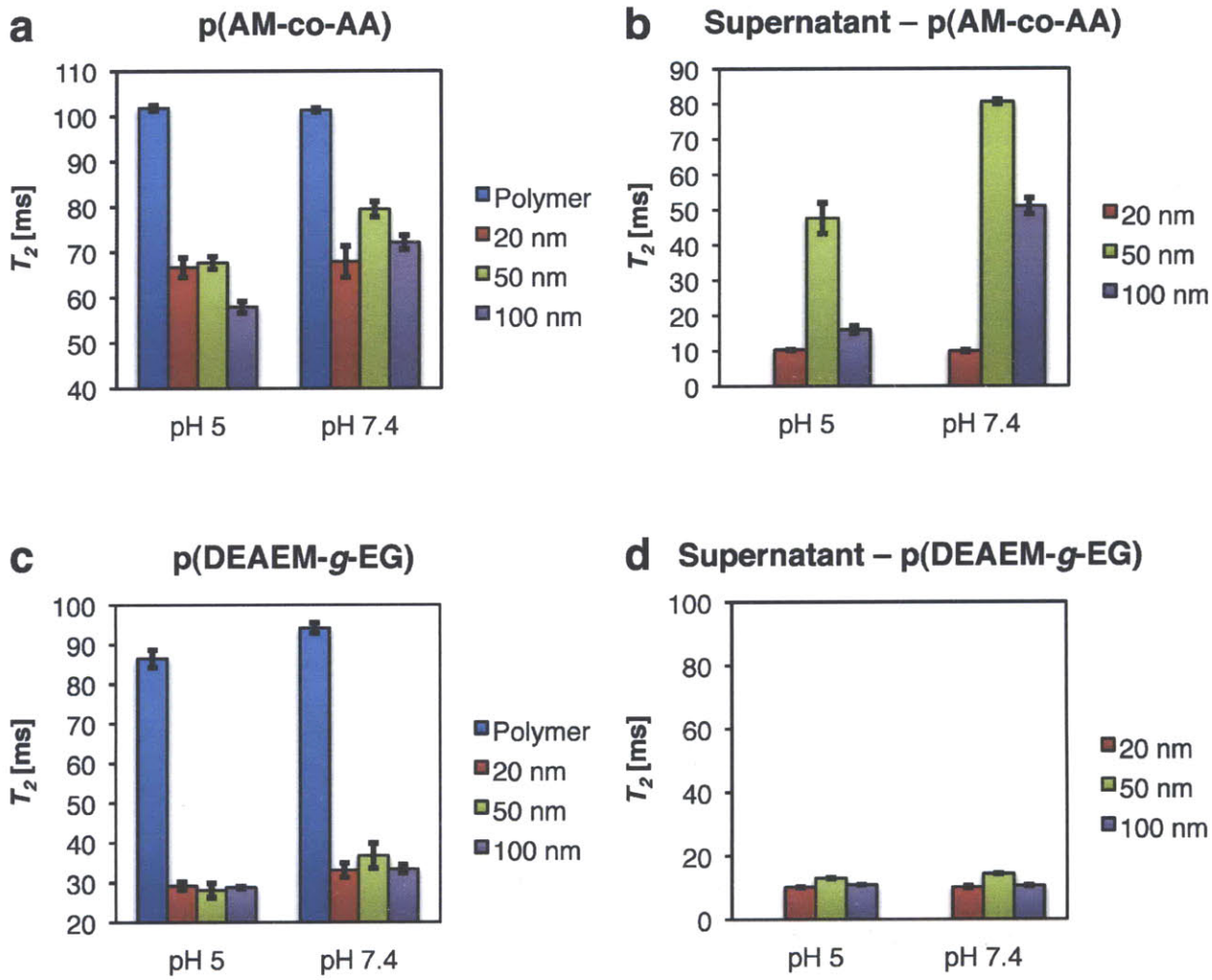

Figure 5.13 Nanoparticles interact with p(AM-co-AA) gels to provide pH-dependent T_2 contrast while p(DEAEM-*g*-EG) do not requires nanoparticles to generate contrast. **a**, p(AM-co-AA) gels generate contrast if >20 nm diameter nanoparticles are included. **b**, The relaxivity of p(AM-co-AA) sample supernatants indicate pH-dependent particle uptake of >20 nm nanoparticles. **c**, p(DEAEM-*g*-EG) gels generate pH-dependent contrast on their own or with further inclusion of 20 nm, 50 nm, or 100 nm magnetic nanoparticles. **d**, The relaxivity of p(DEAEM-*g*-EG) sample supernatants suggest no nanoparticle absorption by the gel.

The first conclusion we draw from this data is that p(DEAEM-*g*-EG) gels do not trap the magnetic nanoparticles. The particles therefore do not appear to complicate the contrast mechanism of the p(DEAEM-*g*-EG) based sensors described in the main body of this Chapter. The second conclusion we draw is that p(AM-co-AA) sensor contrast is based on pH-dependent changes in particle-polymer interaction rather than proton chemical exchange.

The aim of this work was to develop an implantable MR readable pH sensor. We determined the performance characteristics of the p(DEAEM-*g*-EG) sensors to be sufficient for further *in vivo* use. The importance of particle-polymer interaction to p(AM-co-AA) sensor functionality is clear from this data but we chose to leave its specifics unresolved at this time.

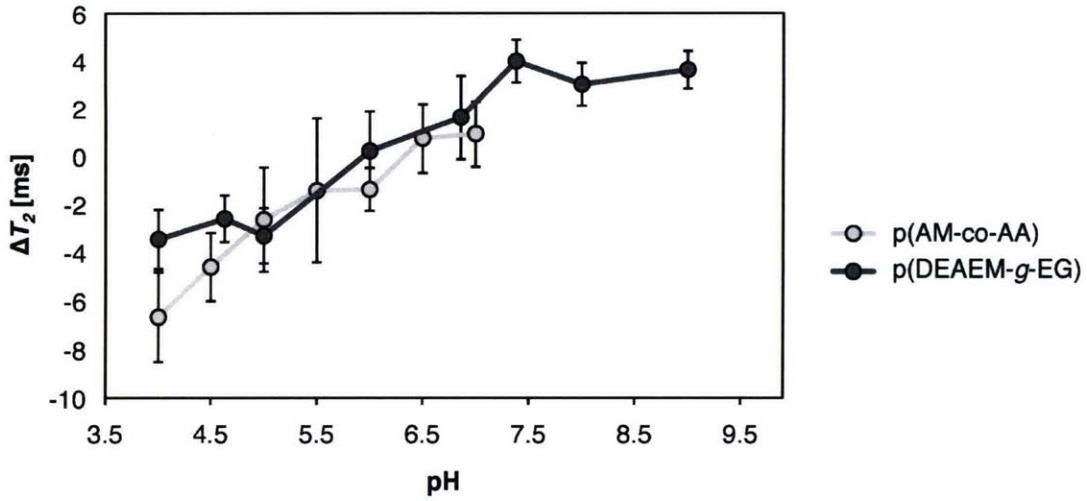

Figure 5.14 The pH response curve of p(AM-co-AA) sensors exhibits a somewhat reduced sensitivity range as compared to p(DEAEM-*g*-EG) sensors. 30 nm magnetic nanoparticles were included in both sensor types The data is plotted as the mean of n=3 samples and error bars correspond to the standard error.

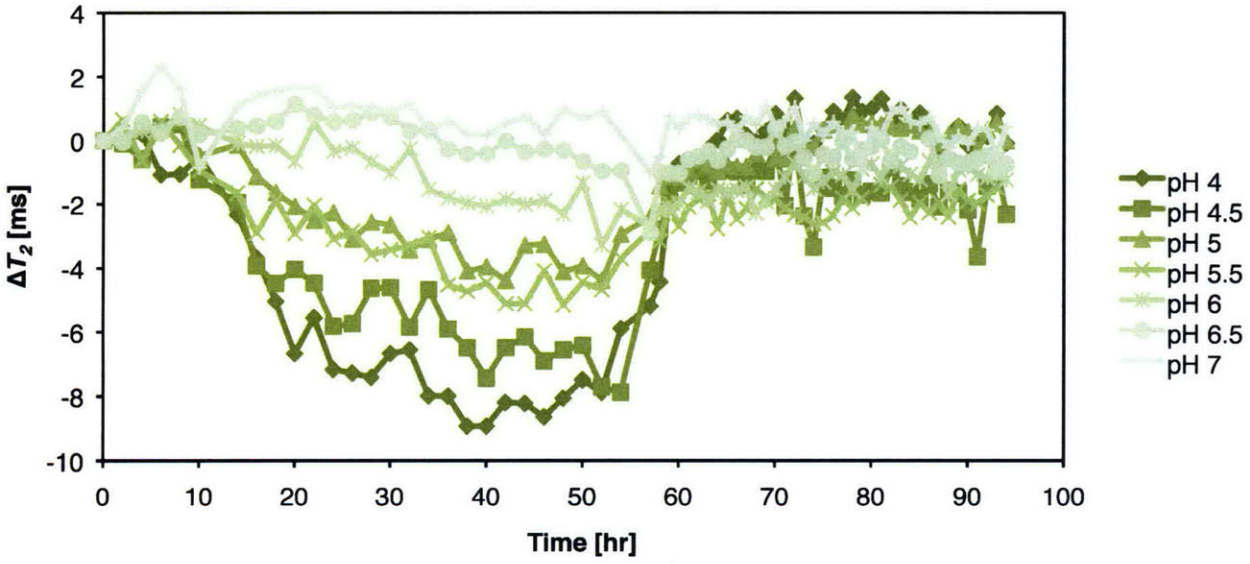

Figure 5.15 Reversibility of p(AM-co-AA) sensors is shown. Sensors equilibrated in the designated pH buffers were re-equibrated in pH 7 buffer starting at the 60 hr time point. The data is plotted as the mean of n=4 samples and error bars are omitted to facilitate uncluttered visualization.

5.6.1.2 Sensor Characterization

The pH response curve of p(AM-co-AA) sensors was found and plotted together with p(DEAEM-*g*-EG) sensors in Figure 5.13. It is roughly linear in the pH 4 to pH 5.5 range, which is shifted from that of p(DEAEM-*g*-EG) but roughly in line with its welling properties shown in Figure 5.10. We are interested in measuring the physiological pH 5.5 to 7.4 range but p(AM-co-AA) sensors may possess superior sensitivity for measuring lower pH values. p(AM-co-AA) sensor reversibility was also verified (Figure 5.14).

5.6.1.3 Hydrogel Synthesis

A superhydroporous version of p(AM-co-AA) was synthesized to be used as the pH-sensitive MR contrast medium. Two monomers, 1.5 mL acrylic acid (AA) and 1 g acrylamide (AM) were dissolved in 2.3 mL DI H_2O. 25 mg N,N'-methylene-bis-acrylamide (BIS) crosslinker, 50 mg Pluronic F127 detergent, and 50 μL N,N,N',N'-tetramethylene diamine (TEMED) was added to the mixture. TEMED and ammonium persulfate (APS) form the polymerization-inducing redox pair. 5 g $NaHCO_3$ next added and and the mixture allowed to bubble for 180 s. APS was then thoroughly mixed into the sample to facilitate overnight polymerization at room temperature. Superhydroporous gel slabs were washed with DI H_2O, dried at 80°C for 2 days, cryomilled (SPEX Certiprep 6850 Freezer/Mill) to a powder of sub-100 μm particles, and stored under vacuum.

5.6.2 CEST-based Chemical Exchange Measurements

Chemical exchange saturation transfer is a NMR technique first developed by Forsén and Hoffman (16) to measure the speed or proton transfer between water and salicylaldehyde.

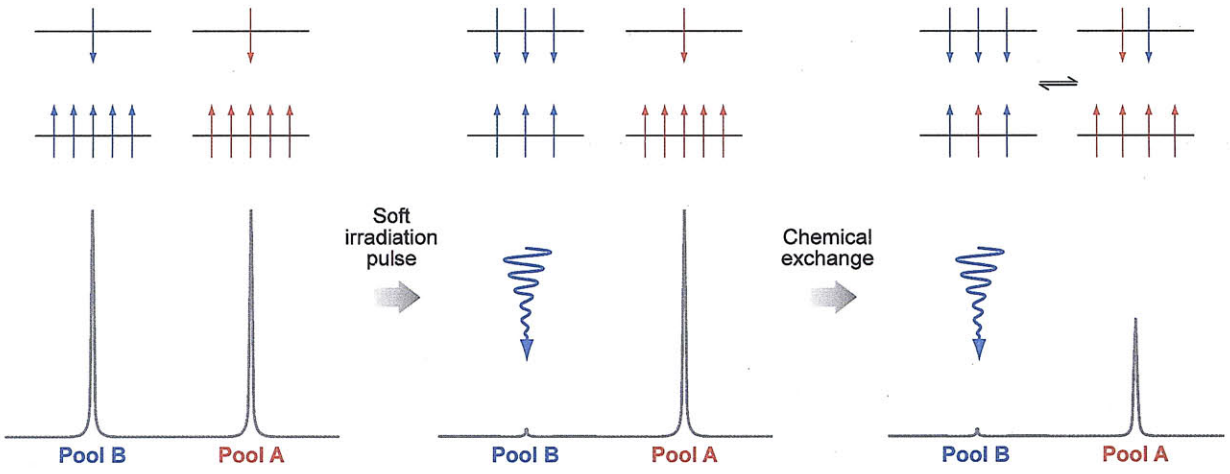

Figure 5.16 Schematic representations of the distribution of spins, aligned with and against the field (upper and lower energy levels, respectively) (*above*) and simulated NMR spectra (*below*) for two chemically distinct pools of nuclei (*left*), two spins after a saturation pulse has been applied to one pool (*middle*), and for a system undergoing chemical exchange after a saturation pulse has been applied to one pool (*right*). Figure and caption reproduced from Sherry and Woods (17).

It requires that two chemical pools A and B possessing distinct Larmour frequencies undergo chemical exchange (Figure 5.16). The general idea is to temporarily saturate one pool, B, with a soft irradiation pulse so that its net magnetization becomes zero. Pool B then exchanges with pool A so some of its saturated spins will transfer to pool A and decrease the net signal intensity of pool A. Signal attenuation in pool A is given by:

$$\frac{M_{A\infty}}{M_{A0}} = \frac{1}{1 + k_2 T_{1B}}$$

where $(M_{A\infty}/M_{A0})$ is the steady-state signal intensity, k_2 is the chemical exchange rate, and T_{1B} is the longitudinal relaxation rate of pool B. We are interested in using this technique to determine the chemical exchange rate between the amine-associated protons and water protons of p(DEAEM-*g*-EG) hydrogel. NMR was, however, designed to measure homogeneous samples of small molecules in solution. It is possible to obtain the NMR properties of our hydrogel samples but the resolution of the spectrums we acquired are poor as compared to 'typical' NMR samples. Comparison of the NMR spectrum of p(DEAEM-*g*-EG) gels hydrated in pH 4.63 and pH 7 buffers nonetheless reveals a marked peak at 2.9 ppm, likely corresponding to increased protonation of some distinct chemical group at low pH (Figure 5.17).

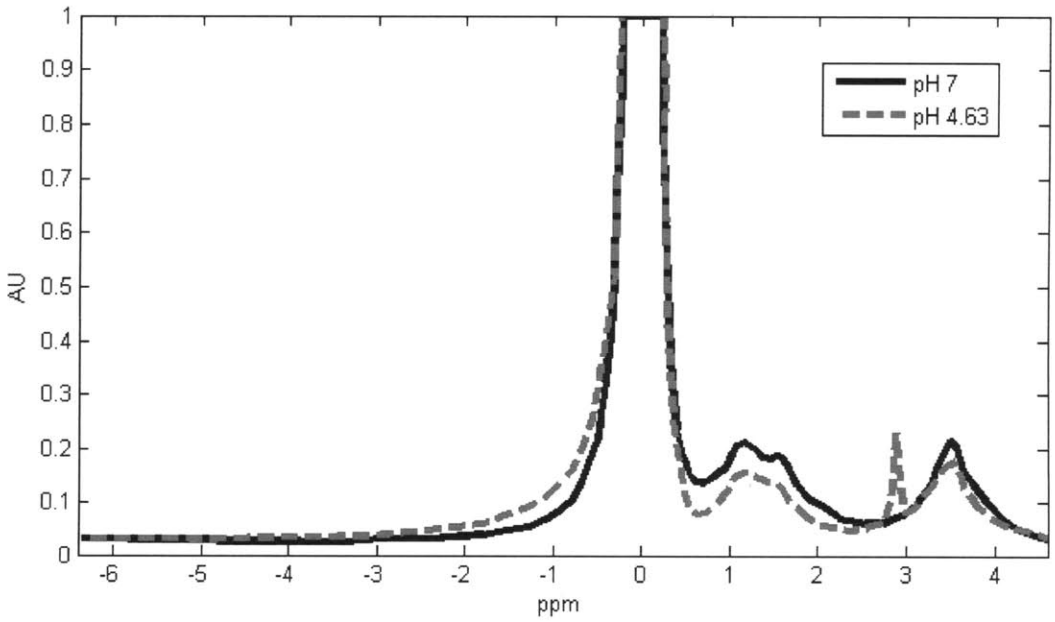

Figure 5.17 The NMR spectrum of p(DEAEM-*g*-EG) gels equilibrated in pH 7 and pH 4.63 buffers. The distinct peak at 2.9 ppm is unique to the pH 7 condition. The x-axis is centered on the water peak (0 ppm).

We then acquired the Z-spectrums, corresponding to water attenuation by saturation of off-water frequencies, of these samples using CEST (Figure 5.18). A noticeable signal attenuation in the positive ppm range for the pH 4.63 as compared to the pH 7 condition suggests a marked increase in chemical exchange at the lower pH. It is unclear why the signal is attenuated in the negative ppm range as well. We did not attempt to quantify the rate of chemical exchange from this data because of poor resolution. The results are nonetheless qualitatively consistent with the model of T_2 contrast put forth in Section 5.2.1.

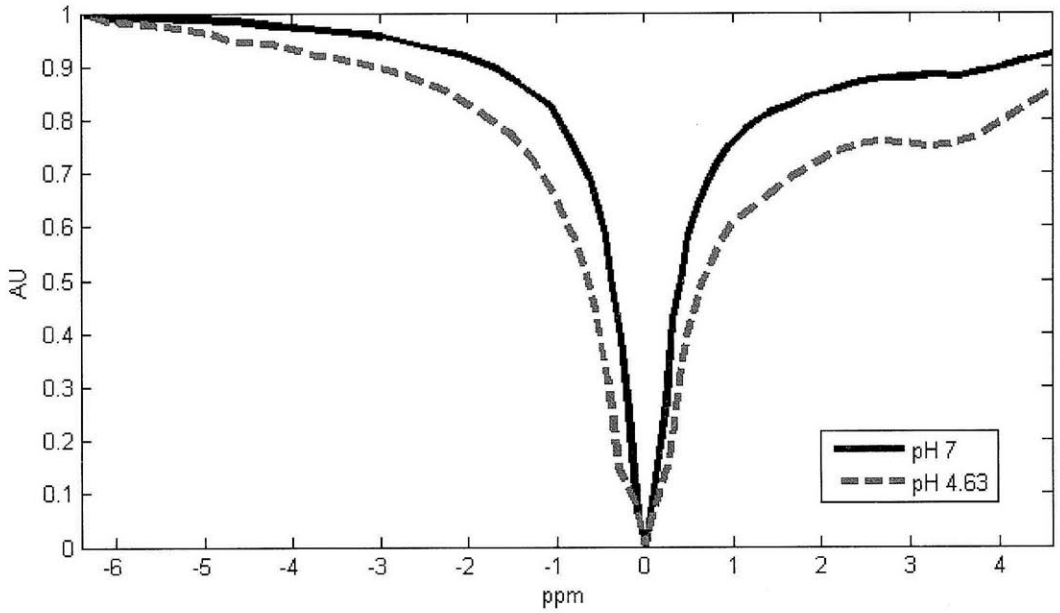

Figure 5.18 The Z-spectrum of p(DEAEM-*g*-EG) gels equilibrated in pH 7 and pH 4.63 buffers. The notch at 3 ppm is more noticeable for the pH 7 condition. The x-axis is centered on the water peak (0 ppm).

5.7 References

1. Wike-Hooley JL, van den Berg AP, van der Zee J, & Reinhold HS (1985) Human tumour pH and its variation. *Eur J Cancer Clin Oncol* 21(7):785-791 .
2. Lindner D & Raghavan D (2009) Intra-tumoural extra-cellular pH: a useful parameter of response to chemotherapy in syngeneic tumour lines. *Br J Cancer* 100(8):1287-1291 .
3. Sun PZ & Sorensen AG (2008) Imaging pH using the chemical exchange saturation transfer (CEST) MRI: Correction of concomitant RF irradiation effects to quantify CEST MRI for chemical exchange rate and pH. *Magn Reson Med* 60(2):390-397 .
4. Podual K, Doyle FJ, & Peppas NA (2000) Preparation and dynamic response of cationic copolymer hydrogels containing glucose oxidase. *Polymer* 41(11):3975-3983 .
5. Podual K, Doyle FJ, 3rd, & Peppas NA (2000) Glucose-sensitivity of glucose oxidase-containing cationic copolymer hydrogels having poly(ethylene glycol) grafts. *J Control Release* 67(1):9-17 .
6. Hills BP (1992) The Proton-Exchange Cross-Relaxation Model of Water Relaxation in Biopolymer Systems. *Mol Phys* 76(3):489-508 .
7. Hills BP (1992) The Proton-Exchange Cross-Relaxation Model of Water Relaxation in Biopolymer Systems .2. The Sol and Gel States of Gelatin. *Mol Phys* 76(3):509-523 .
8. Guivel-Scharen V, Sinnwell T, Wolff SD, & Balaban RS (1998) Detection of proton chemical exchange between metabolites and water in biological tissues. *J Magn Reson* 133(1):36-45 .
9. McConville P & Pope JM (2001) H-1 NMR T-2 relaxation in contact lens hydrogels as a probe of water mobility. *Polymer* 42(8):3559-3568 .
10. Ablett S, Lillford PJ, Baghdadi SMA, & Derbyshire W (1978) Nuclear Magnetic-Resonance Investigations of Polysaccharide Films, Sols, and Gels .1. Agarose. *Journal of Colloid and Interface Science* 67(2):355-377 .
11. Liepinsh E & Otting G (1996) Proton exchange rates from amino acid side chains--implications for image contrast. *Magn Reson Med* 35(1):30-42 .
12. Podual K, Doyle FJ, 3rd, & Peppas NA (2000) Dynamic behavior of glucose oxidase-containing microparticles of poly(ethylene glycol)-grafted cationic hydrogels in an environment of changing pH. *Biomaterials* 21(14):1439-1450 .
13. Taktak S, Weissleder R, & Josephson L (2008) Electrode chemistry yields a nanoparticle-based NMR sensor for calcium. *Langmuir* 24(14):7596-7598 .
14. Buxton RB (2002) *Introduction to Functional Magnetic Resonance Imaging: Principles and Techniques* (Cambridge University Press, New York, NY) 1 Ed p 523.
15. Gemeinhart RA, Chen J, Park H, & Park K (2000) pH-sensitivity of fast responsive superporous hydrogels. *J Biomater Sci Polym Ed* 11(12):1371-1380 .
16. Forsén SH, R.A. (1963) Study of moderately rapid chemical exchange reactions by means of nuclear magnetic double resonance. *J. Chem. Phys.* 39:2892-2901.
17. Sherry AD & Woods M (2008) Chemical exchange saturation transfer contrast agents for magnetic resonance imaging. *Annu Rev Biomed Eng* 10:391-411